

Energy measurements of the electron beam in the storage ring of Diamond Light Source

Niki Vitoratou

Department of Physics
Royal Holloway, University of London



A thesis submitted to the University of London for the degree of Doctor of Philosophy

July 2020

Declaration

I confirm that the work presented in this thesis is my own. Where information has been derived from other sources, I confirm that this has been indicated in the document.

Signed:

Date:

I dedicate this thesis to my family

Abstract

Resonant Spin Depolarization is a high precision technique for beam energy measurement employed in the Diamond Light Source storage ring. The relation between spin tune and beam energy can be used to determine the energy of a transversely polarized beam. The beam is excited at frequencies that match the fractional part of the spin tune and the beam loss rate is used to monitor the beam depolarization.

The standard procedure of these measurements is intrusive and needs a dedicated time during machine developments days. The goal of this study is to enable energy measurements during user operation.

The beam polarization which is essential for the energy measurements was studied theoretically and experimentally for the case of Diamond Light Source (DLS). For the spin depolarisation measurements the detection and the excitation scheme were optimised. A study for the choice of a suitable detector for these measurements has been carried out. An array of four custom-made scintillation detectors has been designed and used for this study. The excitation is gated to half of the stored bunches and the acquisition system counts losses in both halves independently. This approach enables measurements during user operation. Due to the sensitive beam loss detectors and their high accuracy, the beam can be excited weakly but enough in order for the depolarisation resonance to be detected and the small vertical emittance in the range of $pm-rad$ not to be affected. A new concept for detecting the depolarization resonance even when it coincides with higher order betatron resonances is presented. The resonant spin depolarisation measurement was achieved during user operation and a good long-term stability of the beam energy was measured.

Acknowledgements

I would like to thank Pavel Karataev, my academic supervisor of my PhD thesis. He always supported me and encouraged me to participate in schools and conferences to present and discuss my work. I wish to show my gratitude to the head of the Diagnostics group Guenther Rehm who introduced me to the new world of Diagnostics and sparked always my curiosity with new questions and ideas to explore. His enthusiasm and curiosity are two values I will always remember and I will try to bring into everyday life.

I would like to thank the Diagnostics Group (Michael Abbott, Chris Bloomer, Lorraine Bobb, Graham Cook, Sandira Gayadeen and Alun Morgan) for their support, help and the long discussions regarding diagnostics. I would like to thank the Accelerator Group of Diamond, especially Ian Martin, Marco Apollonio, Richard Fielder and Johan Bengtsson with whom we shared discussions about Resonant Spin Depolarisation and the modelling of the machine for the SLIM code. I wish to acknowledge the help of the Operations and Controls and Engineering group at Diamond for their help.

I would like to pay my special regards to Stewart Boogert, who was always interested in hearing my scientific problems and offering advice. Thank you very much to everyone in the Physics Department at Royal Holloway who made me feel welcome and part of the group. I always had a great time when I was visiting the university.

I would like to thank Royal Holloway, University of London and Diamond Light Source for providing me with the funding and the opportunities to participate in schools for Accelerator Physics and conferences. Also I would like to thank CAS school for providing me with a grant to participate in the Diagnostics CAS school 2018.

I wish to give individual thanks to my friends; Despina, Aiveen, Chara, Giota and Cristina who were always there to support me, discuss my problems and cheer me up.

Finally, I would like to thank my parents for their unconditional trust and encouragement, and my partner Antonis who is always by my side to hear my problems, celebrate my achievements, make me laugh and share my dreams with.

Contents

1	Introduction	15
1.1	Theoretical background in accelerator physics	15
1.1.1	Co-ordinate system	15
1.1.2	Single particle dynamics	16
1.1.3	Hill's equation	18
1.1.4	Dispersion	19
1.1.5	Synchrotron motion	19
1.1.6	Main storage ring components	22
1.1.7	Beam lifetime	23
1.2	Synchrotron radiation and synchrotrons	25
1.3	Diamond Light Source	26
1.4	Beam energy	28
1.4.1	Energy measurement methods	29
1.4.2	Resonant spin depolarisation	31
1.5	Research challenges and objectives	32
2	Theoretical background, Simulations and Calculations	35
2.1	Sokolov-Ternov effect	35
2.2	Beam polarisation	36
2.3	Spin precession and beam energy	36
2.4	Radiative beam depolarisation	37
2.5	Depolarisation resonances	39
2.6	Energy spread	40

2.7	Spin depolarisation	41
2.7.1	Froissart-Stora equation	42
2.8	Touschek lifetime	43
2.9	Simulation Studies and Calculations	44
2.9.1	SLIM	44
2.9.2	The FESTA code	49
2.9.3	Spin response function	53
2.9.4	Summary	56
3	Hardware Setup	57
3.1	Theory of Beam Loss Monitors	57
3.1.1	Electromagnetic showers	57
3.1.2	BLM working principle	58
3.1.3	Scintillators	59
3.1.4	Cherenkov radiation	59
3.1.5	Photomultiplier tube	60
3.1.6	PMT characteristics	62
3.1.7	Matching of scintillator and PMT	63
3.2	Detection system	64
3.2.1	Position of the detectors	65
3.2.2	Radiochromic film measurements	65
3.2.3	Comparison of three detectors	68
3.2.4	Detector pulses	69
3.2.5	Photomultiplier calibration test	70
3.2.6	Counting performance	70
3.2.7	Choice of detector	71
3.2.8	Lead shielding	73
3.2.9	Scintillator performance for different beam currents	76
3.2.10	Detector design	78
3.3	Acquisition system	79
3.3.1	Counting mode	80
3.3.2	Libera software	83
3.4	Excitation	83

3.4.1	Excitation hardware	83
3.4.2	Excitation principle for energy measurements	86
3.4.3	Amplifier problem	86
3.5	Synchronisation	88
3.6	Summary	92
4	Results and discussion	93
4.1	Beam polarisation	93
4.1.1	Beam loss and lifetime data	93
4.1.2	Calculation of the beam polarisation	95
4.2	Beam depolarisation measurement	98
4.2.1	Resonant Spin Depolarisation scan	98
4.2.2	Touschek particle detection in high dispersion areas	99
4.2.3	New approach of the depolarisation scan	100
4.2.4	Accuracy of the energy measurement	102
4.2.5	Reverse scan	102
4.2.6	Strength of resonance	103
4.2.7	Excitation duration of the depolarisation scan	104
4.2.8	Synchrotron sidebands	104
4.2.9	Continuous energy measurements	105
4.2.10	Betatron resonances	106
4.2.11	Top-up normalisation	107
4.2.12	Momentum compaction factor	109
4.3	Summary	110
5	Conclusions	113
5.1	Summary of work	113
5.2	Future Work	115

List of Figures

1.1	The trajectory coordinates of a particle, given with respect to the Frenet–Serret frame.	16
1.2	The particles B arrives later than particle A in the RF cavity and see a different accelerating voltage. Their longitudinal phase space plot is shown in the last plot.	21
1.3	The separatrix of a stationary bucket.	21
1.4	A 3D overview model of Diamond Light Source.	27
2.1	The polarisation vector is resonantly rotated away from the vertical direction when the perturbation is in phase with the nominal spin precession. The integrated magnetic field that is used to perturbate the spin is shown in the sinusoidal plot [64].	42
2.2	The thin lens representation of an element using the TEAPOT slicing for the case of 4 slices.	47
2.3	The polarisation level and the polarisation time versus the beam energy obtained from simulations with the SLIM code.	49
2.4	The polarisation level that can be achieved under different beam closed orbit distortions.	50
2.5	The depolarisation process calculated with the FESTA code.	51
2.6	The calculation of the expected ratio between the beam losses of a depolarised and polarised beam is plotted in the black line. The error function fit used to model the data is plotted in the red line.	52

2.7	The depolarisation event using different excitation strengths calculated by FESTA.	54
2.8	The vertical beta function along the ring.	55
2.9	The Spin Response Function along the ring.	55
3.1	Interference of spherical wavelets produced by the particle passage through the medium creates a cone of Cherenkov light. [89]	60
3.2	The photomultiplier structure [92].	61
3.3	Photomultiplier operating circuit [93].	61
3.4	The radiochromic film layers.	66
3.5	Radiochromic film installed in the storage ring.	66
3.6	Radiochromic film darkening after one week exposure in the electron beam.	66
3.7	The calibration curves that were used for the calculation of the dose from the exposure of the radiochromic film Gafchromic RTQA2.	67
3.8	The radiation dose around the beam pipe is used as a guide to design the detector geometry in order to capture the highest fraction of the beam losses.	67
3.9	The pulses created by the three different detectors.	69
3.10	The lab setup for the calibration of the PMTs.	70
3.11	The integrated ADC signals acquired from the three different PMTs versus different voltage gains.	71
3.12	Comparison of counting rate for the three detectors.	72
3.13	The lead shielded detectors installed in the storage ring.	73
3.14	The count rate for different voltage gain as the lead thickness changes.	74
3.15	The intensity spectrum of the bending magnet is shown in the blue line. The transmitted synchrotron radiation spectrum through a lead sheet of 1.3 mm, 2.6 mm and 5.2 mm are shown in the red, yellow and purple line respectively.	76
3.16	The count rate for different voltage gains in the PMT as the beam current increases.	77
3.17	The transverse view of the custom-design of the scintillator detectors. Four blocks, identical to the blue one, are designed in order to fit and be placed around the octagonal beam pipe.	78
3.18	The mechanical drawing of one of the custom-made blocks of the detector.	78
3.19	The four beam loss detectors installed around the beam pipe.	79

3.20	Picture of the data acquisition electronics module.	80
3.21	Diagram of the counting system.	80
3.22	The principle of ADC masks.	81
3.23	The counting of pulses with the two different methods.	82
3.24	Libera software structure (courtesy of Instrumentation Technologies [104]).	84
3.25	Schematic of the generation of the excitation signal by the TMBF system. The symbol $\textcircled{\sphericalangle}$ represents the signal generator in the NCO. The rectangular waveform used for the modulation is indicated by the symbol $\text{□} \text{□} \text{□}$. The symbol $\textcircled{\times}$ represents the modulation of the signal. The amplifier is depicted by ▷ . In the end the symbol $\text{◁} \text{□}$ stands for the hybrid coupler.	85
3.26	3D design of the striplines used for beam excitation. The current and the magnetic fields generated by the striplines are indicated by the red arrow and the blue loops accordingly.	85
3.27	The principle of excitation of half part of the beam, while the rest of the bunches are unaffected. Subplot <i>a</i> depicts the fill pattern in the storage ring. The first 300 bunches that are excited are coloured gray. Subplot <i>b</i> and <i>c</i> show the message and the carrier signal respectively. The modulated signal, used for the excitation of the beam is shown in subplot <i>d</i>	87
3.28	Graphical explanation of the distorted amplifier's output signal due to the bandwidth of the amplifier.	89
3.29	The timing system for the synchronisation of TMBF system and the beam loss monitor system. The blue line represents the fiber optic connections.	90
3.30	The different reference of the bunches in the fill pattern and the beam loss monitor system is shown in the two <i>x</i> -axes. The first bunch in the fill pattern is represented by the 82 nd ADC cycle sample in the beam loss monitor system. The total fill pattern in the blue colour consists of 900 bunches. The excited 280 bunches are shown in the red colour.	90
3.31	Each ADC cycle sample correspond to four buckets in the fill pattern. The beam loss rate for different ADC cycle samples	91
4.1	The beam losses and the lifetime versus time in minutes during the polarisation process.	94
4.2	The beam losses and the lifetime normalised to the beam current versus time during the polarisation process.	95

4.3	Polarisation build-up using beam loss data and lifetime data.	96
4.4	Polarisation build-up with wigglers turned on.	98
4.5	Resonant spin depolarisation scan.	99
4.6	The ratio of the beam loss data from the two masks show the beam depolarisation. The vertical emittance shows that the vertical beam size does not change during the beam excitation.	101
4.7	The normal scan and the reverse scan are shown in the blue line and red line respectively.	103
4.8	Two depolarisation scan with different gain in the amplifier of the striplines.	104
4.9	Depolarisation scan for different excitation times.	105
4.10	Three depolarisation scans to identify the main resonance and the sidebands.	106
4.11	Energy measurements every hour for a duration of three weeks of user operation. The energy changes over the time in the order of ten keV.	107
4.12	The betatron resonance excitation shown in beam losses and the vertical beam size.	108
4.13	The ratio of the beam losses acquired by the two masks in the red line changes after each top-up injection which are illustrated by a vertical black line. The blue data show the data after the analysis for normalising the steps due to the top-up injection.	109
4.14	The relative change of the energy is plotted versus the relative change of the RF frequency. A linear fit derives the momentum compaction factor. . .	111

List of Tables

1.1	Principal Parameters for the DLS storage ring.	26
2.1	Diamond storage ring parameters related to beam polarisation.	48
3.1	Key parameters of the pulses produced by the three different detectors. . .	70
4.1	Characteristics of the two insertion devices.	97

Introduction

1.1 Theoretical background in accelerator physics

1.1.1 Co-ordinate system

The trajectory of a particle in a synchrotron is defined by the arrangement of the dipole magnets. The guide field inside a dipole magnet is uniform and the ideal motion of the particle is a circle of (local) radius of curvature, $\rho(s)$. This trajectory lies in the centre of the machine's vacuum chamber and is called design orbit. After one complete turn, the particle will return to its initial position with its initial momentum, completing a closed orbit. In the real case scenario, some errors in the alignment and fields of the magnets can cause a divergence of the particle motion from the design orbit, leading to a different closed orbit. The trajectory coordinates are given with respect to the Frenet–Serret frame as is shown in Fig. 1.1 [1]. It rotates with the ideal particle around the accelerator which has the design momentum. At a certain longitudinal location s lying on the design orbit, the deviations in the transverse directions are given by x in the bending plane and y in the perpendicular to the bending plane. However, as there is not an ideal orbit, particles follow a closed curved path around the synchrotron, which is close to the ideal orbit and is called closed or equilibrium orbit.

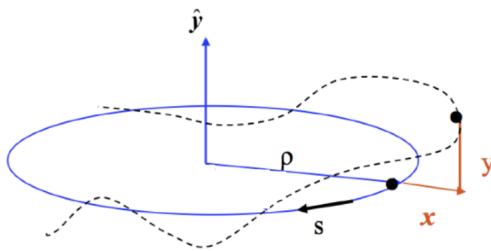


Figure 1.1: The trajectory coordinates of a particle, given with respect to the Frenet–Serret frame.

1.1.2 Single particle dynamics

The motion of a single relativistic charged particle in an accelerator beam line can be described using Hamilton's equations [2]:

$$\frac{dx_i}{dt} = \frac{\partial H}{\partial p_i}, \quad \frac{dp_i}{dt} = -\frac{\partial H}{\partial x_i} \quad (1.1)$$

where x_i are the co-ordinates of the particle, p_i are the components of the momentum and H is the Hamiltonian.

In Hamiltonian mechanics the state of a particle is specified by a pair of dynamical variables, a coordinate q_i and a conjugate momentum p_i . These variables are functions of the independent variable of time t and are independent of one another. In an accelerator where the components are defined by their locations along the reference trajectory, the fields and the Hamiltonians change along the beamline and the path length is chosen as independent variable [3].

Some of the important characteristics of using Hamiltonian mechanics are:

- It uses canonical variables which are used to describe a dynamical system which evolves;
- It offers a structured framework for transforming between coordinate systems (canonical transformation);
- Hamiltonian systems are symplectic. This is important as areas in phase space (emittance) are conserved as the system evolves. Also, the symplectic transfer maps give accurate results in the tracking of particles.

The Hamiltonian equations are used to calculate the evolution of the dynamical variables through the various elements of the accelerator. The changes in the variables at

the exit of each element have a nonlinear dependence on the initial values of the variables. Thus, the linear transfer maps R for accelerator components can be constructed by calculating the Taylor expansion of the Hamiltonian to second order in the dynamical variables. Then the evolution of the dynamical variables may be expressed in matrix formulation [4]:

$$\vec{x}(s = L) \approx R \cdot \vec{x}(s = 0) \quad (1.2)$$

where L is the length of each accelerator component and $\vec{x} = (x, p_x, y, p_y, z, \delta)$ is a vector whose six components are dynamical variables. In particular, x and y are the horizontal and vertical co-ordinates in a plane perpendicular to the reference trajectory at any point. The momenta p_x and p_y are given by the equations:

$$p_x = \frac{\gamma m \dot{x} + q A_x}{P_0}, \quad p_y = \frac{\gamma m \dot{y} + q A_y}{P_0} \quad (1.3)$$

where \dot{x} and \dot{y} are the derivatives of x and y with respect to time, A_x, A_y the horizontal and vertical components of the magnetic vector potential A which is used in the equations of motion for a charged particle in an electromagnetic field, P_0 is the nominal momentum and q the electric charge of the particle. The longitudinal co-ordinate z and its conjugate momentum δ which corresponds to the energy deviation are described as:

$$z = \frac{s}{\beta_0} - ct, \quad \delta = \frac{E}{cP_0} - \frac{1}{\beta_0} \quad (1.4)$$

where β_0 is the velocity of the reference particle, c the speed of light and E the energy which is equal to $E = \gamma_0 m c^2$.

In a phase space plot, each particle is plotted for a specific location using the phase space coordinates. The phase space variables for a particle are x, p_x, y, p_y, z , and p_z . When the transverse momentum components are small compared to the longitudinal ($p_z \gg p_x, p_y$) and p_z can be considered to be the same for all particles, then the paraxial approximation can be applied to the beam motion. In this case, x, y can be taken to be the transverse angles with respect to the ideal trajectory. If the magnetic fields through which the beam travels are entirely transverse (no solenoids), trace space (a term used to make a distinction with phase space) is a coordinate space using (x, x', y, y') to describe the transverse motion instead of (x, p_x, y, p_y) [5].

1.1.3 Hill's equation

An alternative formalism to describe the linear dynamics of a single particle, assuming uncoupled motion and $p_x \approx x'$, is given by the Hill's equation $\frac{d^2x}{ds^2} + k(s)x = 0$. In a periodic beam line, the focusing strength k satisfies the periodicity condition $k(s + C) = k(s)$, where C is the circumference of the closed orbit [6]. The function k is analogous to a spring constant in a harmonic oscillator, and is due mainly to the quadrupole magnets [7]. The solution of Hill's equation is given by the phase space coordinates for the horizontal plane:

$$x = \sqrt{2I_x\beta_x}\cos\psi_x(s) \quad p_x = -\sqrt{\frac{2J_x}{\beta_x}}(\sin\phi_x + \alpha_x\cos\phi_x) \quad (1.5)$$

The solution of the Hill's equation describes the oscillatory motion of particles about the reference orbit [8]. These oscillations are called betatron oscillations. The beta function $\beta_x(s)$ is determined by the design of the accelerator lattice and describes the local amplitude of the oscillations around the reference trajectory.

The action variable I_x is invariant of the particle motion and is expressed as [9]:

$$I_x = \frac{1}{2}(\gamma_x x^2 + 2\alpha_x x p_x + \beta_x p_x^2) \quad (1.6)$$

where the Courant–Snyder parameters satisfy the relation $\beta_x\gamma_x - \alpha_x^2 = 1$ and $\alpha_x = -\frac{1}{2}\frac{d\beta_x}{ds}$ and $\gamma_x = \frac{1+\alpha_x^2}{\beta_x}$. This invariant defines an ellipse in phase space which constrains the values of phase space coordinates (x, p_x) to lie on the ellipse with area equal to $2\pi I_x$. The values $\alpha_x, \beta_x, \gamma_x$ are called Twiss parameters and are used to describe the ellipse and determine its shape. Liouville's theorem states that the area of phase space bounded by the ellipse remains constant. Assuming that the angle variables for the particles are uniformly distributed and uncorrelated with the action variables, the value of I_x averaged over all particles of a beam is equal to the root mean square (rms) beam emittance $\epsilon_x = \langle J_x \rangle$. All particles enclosed by a phase ellipse in a symplectic system stay within that ellipse. Thus, the emittance is conserved. In case of uncoupled motion, vertical and longitudinal emittance can be described with the same treatment as it is presented for the horizontal plane. The emittance can be expressed in terms of the beam distribution as:

$$\epsilon_x = \sqrt{\langle x^2 \rangle \langle p_x^2 \rangle - \langle x p_x \rangle^2} \quad (1.7)$$

To compare emittances of beams with different momenta it is convenient to introduce the

normalized emittance as: $\epsilon_N = \beta\gamma\epsilon_x$, where β and γ are the relativistic Lorentz factors.

The parameter ψ_x is the angle variable and is defined by $\tan\phi_x = -\beta_x \frac{p_x}{s} - \alpha_x$. The change in the angle variable when we move from the point s_1 to s_2 is called the phase advance and is given by the expression $\Delta\phi_x = \int_{s_1}^{s_2} \frac{1}{\beta_x} ds$. The total phase advance in the horizontal plane when particles complete a full circle round the ring divided by 2π is used to define the betatron tune. In other words, betatron tune can be expressed as the number of betatron oscillations per one turn around the ring and is given by $\nu_x = \frac{\Delta\phi_x}{2\pi} = \frac{1}{\pi} \int_0^C \frac{1}{\beta_x} ds$, where C is the path length for one complete turn around the ring [10].

1.1.4 Dispersion

If the energy of a particle in the beam, differs from the design energy its trajectory may deviate from the trajectory of a particle at the right energy. In first order, this deviation is linear in the momentum deviation $\delta = \Delta p/p$. In a storage ring, the orbit deviation due to an energy offset is given by the periodic dispersion function $\eta(s)$ as $\Delta x(s) = \eta(s)\delta$.

When the momentum deviation $\delta \neq 0$, the path length of a particle deviates from the design. The ratio of the relative change in path-length to the relative momentum deviation is called the momentum compaction factor and is given by:

$$\alpha = \frac{\Delta L/L}{\delta} = \frac{1}{L} \oint \frac{\eta(s)}{\rho(s)} ds \quad (1.8)$$

where L is the path length and $\rho(s)$ is the bending radius [10].

1.1.5 Synchrotron motion

The longitudinal motion of particles are dictated by RF cavities. An RF cavity is designed to provide enough energy to the particles to account for losses due to synchrotron radiation. This is achieved by timing the particle arrival at the cavity with a specific phase (synchronous phase) in the oscillating voltage. The accelerating voltage from the accelerating fields of the cavities can be expressed as $V = V_0 \sin\phi_s$, where ϕ_s is the synchronous phase and V_0 the amplitude of the RF voltage. A beam particle, in a storage ring with nonzero RF voltage, except of betatron oscillations, performs oscillations in the longitudinal phase space. The frequency of the synchrotron motion is much lower than the horizontal and vertical betatron-oscillation frequencies. It can be expressed in terms of a synchrotron tune Q_s which is the number of synchrotron oscillations in one complete turn

around the ring, or the ratio between the synchrotron frequency f_s and the revolution frequency f_{rev} . It is given by the equation [11]:

$$Q_s = \frac{f_s}{f_{rev}} = \sqrt{\frac{(\gamma^{-2} - \alpha)h e V_0 \cos \psi_s}{2\pi c p_0}} \quad (1.9)$$

where α is the momentum compaction factor, h the harmonic number which corresponds to the ratio of the RF frequency over the revolution frequency (f_{rf}/f_{rev}), e the particle charge, p_0 the equilibrium momentum, c the speed of light, γ the Lorentz gamma and ψ_s the synchronous phase angle.

1.1.5.1 Energy acceptance

Particles which deviate from the synchronous phase are subjected to a restoring force leading to harmonic oscillations or synchrotron oscillations about synchronous phase ϕ_s . In Fig. 1.2 particle B arrives later than the synchronous particle A . The particle's motion can be plotted in longitudinal phase space. The vertical axis corresponds to the energy difference between the particle B and the synchronous particle A . The horizontal represents the relative phase of the particle and RF wave [12].

The longitudinal motion of the electrons in the beam can follow stable or unstable trajectories, which are divided by separatrices in phase space. Particles in the unstable region undergo a continuously increasing deviation from the synchronous phase and momentum and can be lost. Separatrices is a boundary between the region of stable and unstable motion. Within the phase stable region particles perform oscillations about the synchronous phase and the ideal momentum. These regions are known as RF buckets. The separatrix for a stationary bucket, which means no acceleration, is shown in Fig. 1.3 [11] The synchronous phase is set to $\phi_s = \pi$ and the separatrix extends from 0 to 2π radians. For accelerating buckets, the shape of the separatrix depends on the setting of the synchronous phase and is different from the case of the stationary bucket.

Some particles inside the separatrix reach maximum deviation in phase and momentum from the ideal values during synchrotron oscillations. The value of the maximum energy deviation of the stable synchrotron oscillations is called energy acceptance of the accelerator. The maximum energy acceptance for a stationary bucket is [13]:

$$\left(\frac{\Delta E}{E_0}\right)_{stat} = \sqrt{\frac{2eV_0\beta}{\pi h|\eta_c|E_0} | \cos\phi_s + (\phi_s - \pi/2)\sin\phi_s |} \quad (1.10)$$

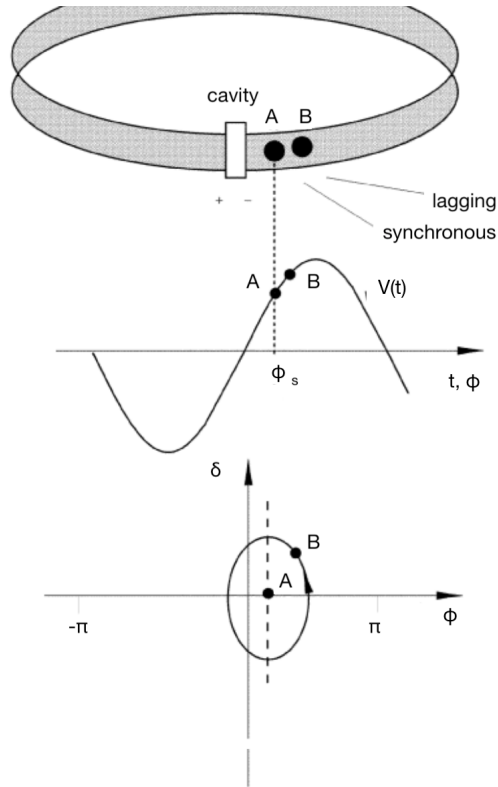


Figure 1.2: The particles B arrives later than particle A in the RF cavity and see a different accelerating voltage. Their longitudinal phase space plot is shown in the last plot.

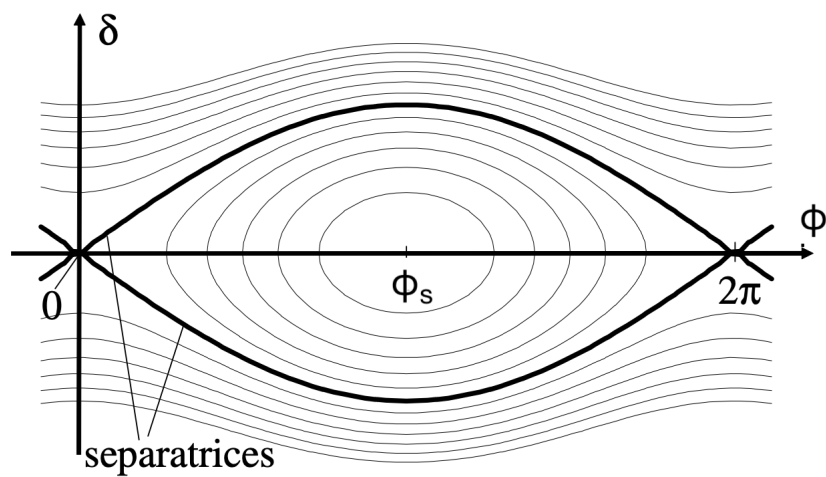


Figure 1.3: The separatrix of a stationary bucket.

where E_0 is the energy of the synchronous particle, $h = f_{RF}/f_{rev}$ is the harmonic number of the cavity, V_0 is the maximum RF voltage in the cavities and $\eta_c = \alpha - \gamma^{-2}$, where α is the compaction factor and γ the Lorentz factor, is the slip factor.

1.1.6 Main storage ring components

The storage ring consists of a group of technical components which hold an important role for the operation of the machine. Some of them are described [14].

- Magnets

Different types of magnets are used in a storage ring, each one for different purpose. The bending magnets are used to deflect the electron beam to define the geometry of the storage ring. A storage ring consists of a series of arc sections (bending magnets), interrupted by straight sections. Bending magnets also serve as sources of synchrotron radiation. The quadrupole magnets are placed in straight sections between bending magnets for focusing the beam particles in order not to deviate strongly from the ideal orbit. The sextupole magnets are used to correct for chromatic aberrations caused by focusing errors on particles with different energies.

- Vacuum chamber

The electron beam must be enclosed in a vacuum chamber where the air pressure is reduced to some or lower to prevent particle losses due to scattering on residual gas atoms.

- Radio Frequency (RF) system

Special accelerating RF cavities generate a synchronous accelerating electric field with the arrival of electrons. The acceleration compensates for the energy loss due to the emission of synchrotron radiation. Proper acceleration occurs only when electrons pass through the cavity at a specific time. Thus, the circulating beam is composed of a number of bunches. The distance between bunches is any integer multiple of the RF-wavelength.

- Beam controls

Beam controls include the beam diagnostics to monitor the beam and the feedbacks to correct for any distortions created to the beam.

- Injection system

Injection system is responsible to transfer the electrons that are generated in the injector and accelerated in the booster to the storage ring.

- Insertion devices

Insertion devices are used to provide the desired radiation from the users when the synchrotron radiation from the bending magnets does not meet the requirements of the users. They are placed in straight sections and are composed of a number of poles with opposing polarities. Thus, the synchrotron radiation can be produced when the beam is bending but the total beam deflection in the exit of the magnet is zero. The most popular insertion devices are the wigglers which are used to produce high intensity broad band radiation and the undulator magnets which produce high brightness, quasi monochromatic radiation.

1.1.7 Beam lifetime

The stored beam electrons can get lost producing either rapid beam losses or gradual beam losses. Technical component malfunctioning or physical obstruction of a beam line and phenomena like RF trips, beam instabilities or pressure bumps can lead to immediate beam loss. However other mechanisms like quantum diffusion, residual gas scattering and intra-beam scattering cause gradual beam loss. To characterise the gradual beam loss, the quantity of beam lifetime is used. The lifetime τ of a beam containing N particles is defined through its relative loss rate \dot{N} at a given time [13]:

$$\frac{1}{\tau} = -\frac{\dot{N}}{N} \quad (1.11)$$

The beam lifetime in an electron storage ring is determined by the effects of the intra-beam scattering and elastic and inelastic residual gas scattering [15]. More specifically, the phenomena that affect the beam lifetime are:

- Quantum diffusion

Normally the electron bunches in a storage ring have a Gaussian distribution in all six phase space coordinates. When the aperture of the ring is small in any dimension, the tails of the Gaussian distribution can be scraped. When

electrons emit synchrotron radiation, can randomly be driven in the tails of the distribution and get lost [16].

– Residual gas scattering

The presence of residual gas species even at a low pressure of 1 nTorr, causes scattering of the electrons with the nuclei of residual gas atoms. The scattering may be elastic or inelastic.

* Elastic scattering

In the elastic coulomb scattering of the stored beam electrons with the nuclei of residual gas atoms, the electrons are deflected from their path and their betatron oscillation amplitude increases. If the amplitude of betatron oscillation of an electron is more than the chamber aperture the electron is lost [17].

* Inelastic gas scattering

Charged particles passing through matter become deflected by strong electric fields from the atomic nuclei. The deflected charged particles lose energy through emission of radiation which is called bremsstrahlung. If this energy loss is too large such that the particle energy error becomes larger than the storage ring energy acceptance, the particle gets lost.

– Touschek scattering

Touschek scattering is a single scattering between two electrons of the bunch. The collision can transfer momentum from transverse to longitudinal motion and both the electrons can exceed the longitudinal acceptance, in which case they are lost.

When several processes contribute, the resulting beam lifetime is found by adding the respective loss rates. Thus, the total lifetime for a storage ring is [18] :

$$\frac{1}{\tau} = \frac{1}{\tau_q} + \frac{1}{\tau_g} + \frac{1}{\tau_t} \quad (1.12)$$

where τ_q is the quantum lifetime, τ_g is the vacuum lifetime and τ_t is the Touschek lifetime.

Usually, the quantum lifetime is much longer than the other two lifetimes and can be neglected. The residual gas lifetime is typically much smaller compared to Touschek

loss. Touschek scattering is the most dominant mechanism for beam losses in a storage ring.

1.2 Synchrotron radiation and synchrotrons

Synchrotron radiation is electromagnetic energy emitted by charged particles (e.g., electrons and ions) that are moving at speeds close to that of light when their paths are altered, as by a magnetic field. Synchrotron radiation covers the spectral range from terahertz and infrared to UV and hard X-rays. This range of the electromagnetic spectrum is known as ‘synchrotron light’ and can be produced by a dedicated synchrotron light source.

A synchrotron light source begins with an electron gun which liberates electrons due to thermionic emission. These electrons are packed in bunches, accelerated through a Linear Accelerator (LINAC) and then injected into the booster synchrotron in most of the synchrotrons facilities. In the booster ring, they are accelerated to ultra-relativistic speeds and later enter another ring, the storage ring, where they circulate under the effect of the bending magnets. As the electrons pass through different types of magnets, such as bending magnets, undulators and focusing magnets, they lose energy in the form of synchrotron radiation. This light can then be channelled out of the storage ring wall and into the experimental stations, called beamlines. The energy lost by the electrons in the process of generating this synchrotron light is restored as they pass through the RF cavities.

The synchrotron light is used today to carry out fundamental research in areas as diverse as condensed matter physics, pharmaceutical research and cultural heritage. For planning experiments, the most important figure of merit to assess an X-ray source is its brightness, which is the photon flux normalized to the solid angle of emission, the source size, and an energy band [19]. There are more than 50 light sources in the world (operational, or under construction) in order to satisfy the growing demand for beamtime [20].

1.3 Diamond Light Source

The Diamond Light Source (DLS) is the UK's 3rd generation light source operating at 3 GeV energy. In the linac, the produced electrons are accelerated up to 100 MeV [21]. The 100 MeV electrons are injected to the booster synchrotron which accelerates the electrons up to 3 GeV energy and extracts them to the final stage, the storage ring.

The storage ring consists of 24 sections with the same magnet distribution, which are called cells. Two different multi-magnet arrangements are used, the Double Bend Achromat (DBA) lattice and the Double-Double Bend Achromat (DDBA) lattice. These arrangements aim to provide long magnet free sections, which are named straight sections, in order to allow the installation of insertion devices [14]. DLS storage ring consists of 23 DBA cells and 1 DDBA cell which allows the installation of one more additional insertion device [22]. The total circumference of the ring is 561.6 m [23]. The RF frequency of 499.7 MHz results in 936 buckets with a bunch spacing of approximately 2 ns. The principal parameters are listed in Table. 1.1.

Table 1.1: Principal Parameters for the DLS storage ring.

Parameter	Values
Energy	3 GeV
Circumference	561.6 m
Lattice	23 x DBA, 1 x DDBA
Injection energy	3 GeV
Beam current	300 mA
Lifetime	10 - 20 hrs
Emittance; horiz, vert	3.17, 0.008 nm-rad
Bunch length (fwhm)	17.1 ps (for 0.62 nC bunch current)
Revolution frequency	533.8 kHz
RF frequency	499.68 MHz

The storage ring can be filled with an arbitrary bunch pattern, subject to a current limit which depends on the number of bunches, and a maximum limit of 300 mA.

The bunch patterns that are currently offered to users are:

- *Standard mode*

900 contiguous bunches, 2 ns apart, each with a charge of 0.62 nC (0.33 mA), with a gap in the bunch train of 72 ns; total current = 300 mA.

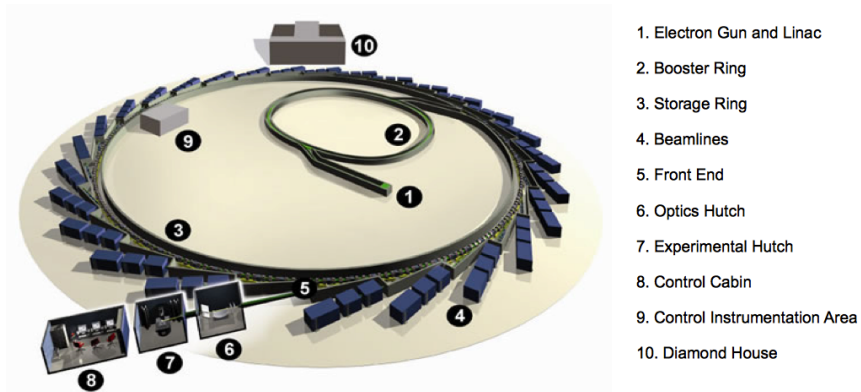


Figure 1.4: A 3D overview model of Diamond Light Source.

– *Hybrid mode*

A train of contiguous bunches (typically between 686 and 836 bunches in length), 2 ns apart, plus a single/group of bunches centered in the gap with charge in the range 0.67 nC to 6 nC (0.36 mA to 3.2 mA). Total current is maintained at 300 mA.

– *156 bunch mode*

156 bunches equally spaced, 12 ns apart, each with a charge of 1.63 nC (0.87 mA), total current = 136 mA.

– *Low alpha mode*

This special operating mode utilises a different storage ring optics to the standard, hybrid and 156 –bunch modes, in order to create short electron bunches, with low beam current. This mode has two varieties, short pulse mode and THz mode.

The different modes allow the users to conduct different experiments and apply time-resolved experimental techniques. The synchrotron is free at the point of access through a competitive application process, provided that the results are in the public domain. Most commonly, Diamond runs with the normal user optics.

The two 2.2 MV superconducting RF cavities in the storage ring are operating at frequency of 500 MHz. They compensate for the energy losses and allow the beam to maintain a fixed orbit around the storage ring.

The front-end is fitted to the storage ring where synchrotron light is channelled into a beamline and is used to monitor the position of the synchrotron light, to protect

the storage ring if there is a leak in the beamline and to remove heat that is created by the synchrotron light.

Diamond facilitates 32 beamlines which provide a range of methods for academic and industrial researchers like diffraction, imaging, microscopy, scattering and spectroscopy techniques. Researchers from across both academia and industry use Diamond to conduct experiments, assisted by approximately 620 staff. Most beamlines are divided into three sections: optics hutch, experimental hutch, and control cabin. The optics hutch is the first room where the photon beam enters and is prepared by focusing and filtering as required for the particular needs of the beamline using optical devices like mirrors and diffraction gratings. The experimental hutch houses the experimental apparatus which is used for the testing of the samples. Rotating arms are used to change the positions of the sample and detectors collect data from the interaction of the synchrotron light with the sample. The detectors send the collected data to the control cabin. The control cabin is usually the room occupied by scientists who monitor and control the experiment. In the end, Diamond house accommodates many of Diamond's staff, as well as meeting rooms and conference facilities.

The accelerators and photon beamlines are controlled through a distributed, heterogeneous computing environment, using embedded systems for direct control of the instrumentation, together with Linux workstations for the operator interfaces. The software makes extensive use of the open source EPICS Control System tool kit [24]. The client side high-level applications comprise general-purpose tools for synoptic display management, alarm handling and archiving, as well as bespoke tools to control the operation and characterization of the accelerators.

1.4 Beam energy

Beam diagnostics are essential constituents in the commissioning and operation of an accelerator as they monitor and measure the properties and the behaviour of the beam. The beam position, the beam size, the beam current, the fill pattern are some of the parameters that are of interest to measure. This thesis focuses on measuring another important property of the beam, the energy, by developing a special diagnostics system for this purpose.

The term beam energy refers to the average relativistic energy of particles in a beam and is given by the formula:

$$E_{beam} = [p_{beam}^2 c^2 + m^2 c^4]^{1/2} \quad (1.13)$$

where p_{beam} is the beam momentum, m the mass of the particle and c the speed of light. For ultra-relativistic particles, where $pc \gg mc^2$, the beam energy and momentum are closely related by the equation : $E_{beam} = p_{beam}c$.

The beam energy is an important parameter in accelerator physics for the measurement of the W boson mass for the case of LEP, the study of resonances in nuclear physics in an ion beam on fixed target configuration and the characterization of insertion devices for the case of synchrotrons [25].

Different parameters in accelerator physics include in their definition the beam energy. The measurement of the beam momentum can be used either to calculate these parameters or for energy calibration. The momentum compaction factor, for example, is defined as the relative change in circumference with momentum [26]. Measurements of the revolution frequency which derives from the orbit length and the beam energy allow the momentum compaction factor calculation. The quadrupole gradient which is used for the characterisation of the optics is normalised to the beam momentum, thus beam energy is important in order for the gradients obtained from beam-based measurements to agree with gradients given from the model [27].

1.4.1 Energy measurement methods

Different methods have been developed and used in different facilities to measure the electron beam energy. Here the techniques that were used in storage rings are briefly described and their relative precision is stated.

At the Large Electron-Positron Collider (LEP), energy was measured using a spectrometer which consisted of a steel dipole with precisely known integrated field, and triplets of beam-position monitors (BPMs) on either side of the interaction point [25]. The energy was determined by measuring the beam deflection which is inversely proportional to the momentum. For this calculation the magnetic field of the dipole should be known with a relative precision of the order of 10^{-5} and the

spectrometer BPMs must have a precision of $1\ \mu\text{m}$. The relative energy uncertainty $\Delta E/E$ achieved with the LEP spectrometer was of the order of 10^{-4} .

Another approach to measuring the energy at LEP employed the relation between the energy loss caused by the emission of photons and the beam energy [28]. In a machine such as LEP the synchrotron tune, Q_s , depends on the beam energy, the energy loss per turn, and the total RF voltage, V_{RF} . An analysis of the variation of Q_s with V_{RF} can be used to infer the beam energy. However, many variables like the contribution from synchrotron radiation losses in quadrupoles or the energy loss due to the machine impedance, need to enter the analysis. All of these have uncertainties which limit the accuracy of the energy measurement. A cross-calibration using another method which is not compatible for continuous measurements and could not be used at high energies at LEP but attains high precision (Resonant Spin Depolarisation) allows to constrain the input parameters with the high uncertainties. Thus, the method using the RF voltage, the synchrotron tune and the energy loss can achieve beam energy measurements with a resolution of the order of 10^{-4} .

At the Berlin Electron Storage Ring Society for Synchrotron Radiation (BESSY), the energy measurement by Compton-backscattering of laser photons was studied using light from a CO2 laser [29]. The laser light is scattered in a head-on collision with the electron beam in the electron storage ring and the backscattered photons are measured with an energy-calibrated high-purity germanium (HPGe) detector. The exact energy and shape of the high energy edge of the measured Compton spectrum can then be used to determine the electron energy.

A different technique was explored in the same facility by measuring the spectral photon flux of the synchrotron radiation with calibrated energy dispersive photon counters [30]. From this data the characteristic photon energy was determined and in combination with the magnetic fields for storage ring optics which can be measured using a nuclear magnetic resonance system, the electron energy was calculated. The uncertainty of beam energy is of the order of $\Delta E/E = 0.4\%$.

At the European Synchrotron Radiation Facility (ESRF) the energy measurement was based on the analysis of the X-ray spectrum from an undulator [31]. It is based on the dependence between the harmonics wavelengths and the electron beam energy. The X-ray beam is monochromatised at 21 keV by a silicon crystal in back-scattering geometry.

By adjusting the magnetic gap, one makes the third harmonic of the radiation from an undulator coincide with the energy selected by the crystal. The main errors come from the uncertainties in the undulator's magnetic field and period. By operating the undulator at low field, an absolute accuracy of 10^{-3} is reached for the electron energy.

Two schemes based on the concept of synchrotron radiation interference were explored at the Advanced Light Source (ALS) at Berkley and Stanford Synchrotron Radiation Light-source (SSRL). K.-J Kim has proposed to apply the principle of Synchrotron Radiation (SR) interferometry using an interference wiggler which is a set of two simple wigglers [32]. The modulated spectrum which is produced by the interference of radiation from each section of the wiggler can be analysed using a monochromator and the electron energy can be determined up to an accuracy of 10^{-3} . The drawback of this method is that it needs a special beam line dedicated for producing the SR interference.

T. Suwada uses the SR interference requiring no major modification for the machine [33]. This method was tested in the Proton-Electron-Positron II (PEP-II) rings and utilises two neighboring dipole magnets in a straight section of a storage ring, a high resolution monochromator and a photon detector. The system measures the spectral interference of two synchrotron radiation beams emitted from fringing fields of dipole magnets and from the modulation spacing and depth of the photon spectrum, the energy can be derived. The achievable resolution of absolute beam energy is estimated to be $\Delta E/E = 10^{-4}$.

1.4.2 Resonant spin depolarisation

Resonant Spin Depolarization (RSD) is a well-established technique to measure the electron beam energy in synchrotrons [34], [35], [36], [37], [38]. The spin of the electrons is aligned antiparallel with the magnetic field of the bending magnets due to spin-flip synchrotron radiation. Using a device that can generate a time-varying horizontal magnetic field, the spin-vector can be resonantly tilted away from the vertical axis by a small amount in successive revolutions of the storage ring gradually resulting in reduction of the beam polarization. The detection of depolarization is used to determine the precession frequency of the electrons and thus the energy can be calculated. The accuracy of this method is about 10^{-6} .

There are several methods of depolarisation measurement in storage rings. The Touschek polarimeter is based on the phenomenon of Touschek scattering which is a beam loss

mechanism driven by large angle scattering in the electron bunch. The electrons can exceed the longitudinal acceptance limit and get lost, resulting in reduction of the beam lifetime [39]. Scintillator counters can be used to detect changes of the beam loss rate due to the scattering and measure changes on the polarisation of the beam.

Another method for higher energies is the Compton backscattering polarimeter, which utilises the spin dependent cross section for Compton scattering of polarised photons on electrons [40]. The scattering of circularly polarised photons from a laser on vertical polarised electrons is asymmetric with respect to the plane of the storage ring and the magnitude of the asymmetry is proportional to the vertical polarisation of the electron beam.

The third method is based on the polarization dependence of synchrotron radiation intensity [41]. From the expression for the radiation intensity of a classical point charged particle moving with an acceleration which is transverse to its velocity, it follows that the naturally polarised beam of electrons in a storage ring will radiate stronger than a non polarised beam. The SR intensity from two electron bunches, simultaneously circulating in a storage ring, is observed while one of these bunches has been depolarized by a special selective depolarizer. The ratio between the SR intensity produced by the two bunches can be used to reveal the beam depolarisation.

1.5 Research challenges and objectives

Resonant spin depolarisation (RSD) is an energy measurement technique that is based on the natural build-up of transverse polarisation in the electron storage rings. This method attains high precession of 10^{-6} and is commonly used by many synchrotron facilities.

This method's main advantage is that it uses the natural phenomenon of polarisation in a storage ring. The beam polarisation is a prerequisite of this method and has to be studied and measured experimentally to verify that resonant spin depolarisation can be employed. The energy can be measured with an accuracy that other techniques cannot achieve by using suitable instrumentation for beam excitation and a polarimeter. The RSD was successfully implemented at DLS in 2011 [42].

However, this method required a large amount of beam time to allow the build-up of the polarisation. In addition, it is a destructive method by its nature, as it implies the

excitation of the beam. Due to these two main reasons, a dedicated beam time of about three hours was used during DLS development days. With these conditions, the energy measurements were rarely reproduced, and the stability of the beam energy could not be tested.

The motivation of this project is to address these issues. An advanced RSD method compatible with user time could help measure the energy of the beam more frequently without the need for dedicated beam time. The exact energy information can be provided to the beamlines. This information is essential to understand the ID spectrum and polarisation. Also, the energy value is included in the model used to calibrate the ID gap. From the machine side, the beam energy measurement is needed for the optics model calibration and to set the correct magnet strengths.

Several challenges were met in the implementation of the online measurements for the case of DLS. The polarisation level that can be achieved in the DLS storage ring was studied as it is an important prerequisite for the depolarisation measurements. The betatron tunes were changed to study the injection efficiency from the booster to the storage ring in 2017. In the same period, there was no evidence of polarisation in the data from lifetime and beam losses. This raised the question of whether the betatron tunes are related to the absence of the polarisation level. The maximum polarisation level that can be achieved was calculated by the SLIM code theoretically. Experimental studies verified the calculated theoretical values.

One of the main challenges of this project was the beam excitation. The Diamond Light Source operates with a small vertical beam emittance and consequently a small vertical beam size. Thus, the size of the beam is sensitive to any disturbance produced by the beam excitation during the depolarisation scans. For this reason, a low current is applied in the striplines, which is enough to depolarise partially the beam but not to affect the quality of the beam. As a consequence the beam losses created by the depolarisation are low and a sensitive beam loss detection system is required. The sensitivity of the system is defined, in this case, as a high count rate of the detected beam losses. The aim for a high count rate will minimise the uncertainty of the data and will favour the detection of small changes in beam losses and, consequently, changes of polarisation.

Another problem was introduced by external factors that create beam losses, like, changes in the insertion device gaps or operation of the feedback systems. These losses overlap with

the losses due to the depolarisation and are treated as background noise. To overcome this problem the idea of gating the excitation pattern and the beam loss detection was introduced. Only one part of the beam was excited and depolarised. The beam losses from the excited part were normalised with the beam losses from another part of the beam with equal charge, which was not excited. By this way, the ratio of the beam losses of the two parts of the beam shows only the effect of the excitation.

The high sensitivity of the beam loss detectors resulted in detecting beam loss changes created by exciting higher order betatron resonances. During the excitation of the betatron resonances, the vertical beam size increases, while the beam losses decrease. After the crossing, the above parameters return to their nominal values. These resonances overlap with the depolarisation resonance, and the detection of its center is difficult to be determined. A new approach was used to deal with this problem.

According to the Froissart-Stora formula for the depolarisation process, the polarisation of the beam after excitation depends on the depolariser's strength, the duration of the beam excitation and the frequency step of the scan. As was referred before, during user time, the beam is excited weakly, resulting in a weak depolarisation resonance. However, longer excitations of each frequency can be used to compensate for the weak excitation. Thus, the long-lasting energy measurements scans should be modified in order to become suitable for user operation.

By understanding the phenomenon of resonant spin depolarisation for DLS and tackling the introduced challenges, the energy measurements during user time were accomplished. The online measurements can be used to demonstrate the long term beam energy stability and any correlation between the beam energy fluctuations with other parameters of the machine. Beamlines can retrieve an energy measurement every hour and update their models according to the precise beam energy measurement.

From the above considerations, the main objectives are:

- Study the beam polarisation level that can be achieved for the storage ring of the Diamond Light source;
- Design, build and study the beam loss monitors used for the energy measurements;
- Perform the energy measurements during user time.

Theoretical background, Simulations and Calculations

2.1 Sokolov-Ternov effect

According to the Sokolov-Ternov effect, in a storage ring, the spin of the electrons will develop a polarisation antiparallel with the magnetic field of the main bending magnets (which is assumed to be oriented "up") through the emission of spin-flip synchrotron radiation [43]. When electrons are moving on curved orbits, they emit synchrotron radiation. A tiny fraction of the emitted photons will cause a spin-flip between the "up" and "down" quantum states of the electron's spin. For electron spins aligned along a uniform magnetic field, the transitions rates from the up-to-down state and down-to-up state are [44], [45], [46] :

$$W_{\uparrow\downarrow} = \frac{5\sqrt{3}}{16} \frac{r_e \gamma^5 \hbar}{m_e \rho^3} \left[1 + \frac{8}{5\sqrt{3}} \right] \quad (2.1)$$

$$W_{\downarrow\uparrow} = \frac{5\sqrt{3}}{16} \frac{r_e \gamma^5 \hbar}{m_e \rho^3} \left[1 - \frac{8}{5\sqrt{3}} \right] \quad (2.2)$$

where the arrows indicate the relative directions of the spin in the initial and final states, and ρ is the radius of curvature of the orbit, r_e is the classical electron radius, and the other symbols have their usual meanings. The difference between the two transition rates leads to the build-up of polarisation antiparallel to the magnetic field. The net polarisation

that can be achieved is:

$$P_0 = \frac{W_{\uparrow\downarrow} - W_{\downarrow\uparrow}}{W_{\uparrow\downarrow} + W_{\downarrow\uparrow}} = \frac{8}{5\sqrt{3}} = 0.9238 \quad (2.3)$$

For initially unpolarised particles, the polarisation builds up in the vertical direction according to the equation below [43]:

$$P(t) = P_0(1 - e^{-t/\tau_0}) \quad (2.4)$$

where t is the time, P_0 is the maximum polarisation level and the time constant:

$$\tau_0 = (W_{\uparrow\downarrow} - W_{\downarrow\uparrow})^{-1} = \left[\frac{5\sqrt{3}}{8} \frac{r_e \hbar \gamma^5}{m_e \rho^3} \right]^{-1} \quad (2.5)$$

2.2 Beam polarisation

The polarisation vector P of a bunch is defined as the statistical average of an ensemble of the spin vectors S of the individual particles:

$$P = \langle S \rangle = \left| \frac{1}{N} \sum_{n=1}^N S_n \right| \quad (2.6)$$

where N is the number of particles in the bunch [10]. The beam will have spin polarisation of 100% when all the particles in a bunch will be pointing towards the same direction. The polarisation reduces when there is a spread in the direction of the spin vectors.

For uniformly distributed spin vectors around a cone with an opening angle 2θ , where θ is the angle to the vertical plane, the magnitude of the spin polarisation vector is equal to $\cos\theta$ [2].

2.3 Spin precession and beam energy

The motion of the spin vector \vec{S} of a relativistic electron in electromagnetic fields \vec{E} and \vec{B} is described by the Thomas-BMT (Bargmann-Michel-Telegdi) equation [47]:

$$\frac{d\vec{S}}{dt} = \vec{\Omega}_{BMT} \times \vec{S} \quad (2.7)$$

$$\vec{\Omega}_{BMT} = -\frac{e}{\gamma m} \left[(1 + \alpha\gamma)\vec{B}_\perp + (1 + \alpha)\vec{B}_\parallel - \left(\alpha\gamma + \frac{\gamma}{1 + \gamma}\right)\vec{\beta} \times \frac{\vec{E}}{c} \right] \quad (2.8)$$

where \vec{B}_\perp and \vec{B}_\parallel are the components of the magnetic field which are transverse and parallel with respect to the particle's velocity β , c the speed of light, e is the charge, m is the mass, α is the magnetic moment anomaly and γ is the Lorentz factor of the electron [25]. Thus, an accurate description of the spin-magnetic interaction can be obtained.

In a storage ring of a light source storage ring where there are no significant solenoid magnetic fields ($B_\parallel = 0$) nor transverse electric fields ($\vec{\beta} \times \vec{E} = 0$) and the strongest magnetic fields in a storage ring arise from the dipole bending magnets the Eq. 2.8 can be simplified as [48]:

$$\Omega_{BMT} = \Omega_c(1 + \alpha\gamma) \quad (2.9)$$

where $\Omega_c = -(e/\gamma m)B_\perp$ is the cyclotron frequency. The quantity $\alpha\gamma$ is known as the spin tune ν and gives the number of revolutions the spin vector makes about the vertical axis in one revolution of the storage ring. The average value ν for all electrons is directly proportional to the average beam energy E :

$$\nu = \alpha\gamma = \frac{\alpha E}{mc^2} = \frac{E[MeV]}{440.6486[MeV]} \quad (2.10)$$

2.4 Radiative beam depolarisation

In the inhomogeneous fields of storage rings, the Sokolov–Ternov effect is accompanied by depolarisation. While the synchrotron radiation emission gives rise to a polarisation build-up through the Sokolov–Ternov effect, the stochastic nature of the individual emissions can result in a spread of the spin vectors (diffusion) due to the spin-orbit coupling. Photon emission imparts both transverse and longitudinal recoils to the electron, and the electron changes its position in phase space. In the motion that follows after every such emission event, the electron will experience fields in the quadrupoles (and higher-order multipoles) and eventually returns to its original phase space position owing to the damping. However the spin will not point in the same direction as before the emission. Thus, an initially fully polarised ensemble of electrons eventually will have a spread of the spin vectors and the polarisation decreases due to uncorrelated photon emission events. The phenomenon of the spin diffusion is embodied in the Derbenev-Kondratenko equation, which estimates

the attainable equilibrium polarisation [49]:

$$P_{dk} = \pm \frac{8}{5\sqrt{3}} \frac{\oint ds \left\langle \frac{1}{|\rho(s)|^3} \hat{b} \cdot \left(\hat{n} - \frac{\partial \hat{n}}{\partial \delta} \right) \right\rangle}{\oint ds \left\langle \left(1 - \frac{2}{9} (\hat{n} \cdot \hat{s})^2 + \frac{11}{18} \left(\frac{\partial \hat{n}}{\partial \delta} \right)^2 \right) \right\rangle_s} \quad (2.11)$$

where $\langle \rangle_s$ denotes phase space averaging, \hat{s} is the direction of motion, and ρ is the radius of curvature of the orbit. The unit vector $\hat{b} = (\hat{s} \times \dot{\hat{s}}) / |\dot{\hat{s}}|$ is perpendicular to both the velocity and the acceleration and is the direction of the magnetic field in the case of no electric fields and motion perpendicular to the magnetic field.

The unit vector field \hat{n} satisfies the Thomas–BMT equation along particle trajectories $u(s)$ and it is periodic: $\hat{n}(\vec{u}; s) = \vec{n}(\vec{u}; s + C)$ where C is the ring’s circumference. This means that the field $\hat{n}(\vec{u}; s)$ transform to itself in one turn around the machine and, thus, is called ”invariant spin field”. It provides a reference direction for a spin at each point in phase space. On the closed orbit where the orbital amplitude is zero, the $\hat{n}(0; s)$ is written as $\hat{n}_0(s)$ and has vertical direction.

The partial derivative $\frac{\partial \hat{n}}{\partial \delta}$ is the spin-orbit coupling vector and is a measure of the change of \hat{n} caused by the fractional energy jumps δ . It results from the dependence of the radiation power on the initial spin direction, and it introduces the depolarisation term by the spin diffusion in the formula [50]. The Derbenev–Kondratenko formula assumes that the photon emission takes place in a locally uniform magnetic field, i.e. the synchrotron radiation is assumed to be emitted from dipole magnets. It does not take into account synchrotron radiation from more complicated devices such as undulators or free-electron lasers.

In the presence of radiative depolarisation the final polarisation build-up rate can be written in terms of the build-up polarisation rate [51] τ_P^{-1} given in the Eq. 2.5, and the depolarisation rate τ_D^{-1} as:

$$\frac{1}{\tau} = \frac{1}{\tau_P} + \frac{1}{\tau_D} \quad (2.12)$$

The theoretical value for the radiative build-up time is:

$$\tau_P[s] = 98[sGeV^5m^{-3}] \frac{R[m]^3}{E[GeV]^5} \frac{\langle R \rangle}{R} \quad (2.13)$$

where R is the magnet bending radius, E the beam energy and $\langle R \rangle$ the average radius of the machine.

The build-up of the polarisation is given by the following formula:

$$P(t) = P_{\infty}[1 - e^{-t/\tau}] \quad (2.14)$$

where $P_{\infty}[\%] = \frac{0.92x100}{1+\tau_P/\tau_D}$.

2.5 Depolarisation resonances

Particle bunches in storage rings have nonzero transverse dimensions and energy spread and thus, the motion of the spin, compared to that of a spin on the closed orbit, depends on the position in phase space $u(s)$. For a particle orbiting for many turns, the total disturbance to spin can grow significantly if there is coherence between the natural spin motion and the oscillation motion in the beam. In the case of no synchrotron - betatron coupling, the spin-orbit resonance condition is:

$$\nu_{spin} = m + q\nu_x + r\nu_y + s\nu_s \quad (2.15)$$

where m, q, r, s are integers, ν_x, ν_y are the horizontal and vertical betatron tunes of the orbital oscillations respectively and ν_s is the synchrotron tune. The quantity $(|q| + |r| + |s|)$ is called the order of resonance.

The general resonance condition specifies the criteria for many different types of resonances. Some unavoidable magnet misalignments force electrons to execute an oscillating motion around the newly formed equilibrium closed orbit. The misalignment of a quadrupole adds a horizontal and a vertical dipole component in the kick of the electrons. The horizontal component will perturb spin motion from vertical precession. Furthermore, the spin of an oscillating electron that recoils due to photon emission will suffer a horizontal perturbation when it goes through a quadrupole with a vertical deviation away from the center of the magnet. These perturbations will add coherently and cause beam depolarisation if $\nu_{spin} = m$ or $\nu_{spin} = m + q\nu_y$. The first one is called imperfection resonance since it is caused by an imperfect ring and closed orbit distortions. By making suitable orbit corrections, these resonances can be reduced in strength. The second one is called intrinsic resonance since it is caused by the oscillation of a particle and this is intrinsic. Since any beam has a non-zero emittance, these resonances can not be avoided by any error correction scheme. In practice, the above two types of resonances have proven the

most significant in the energy regimes of existing accelerators with polarised beams.

The resonances involving horizontal tune are called intrinsic coupling resonances because they are due to the linear betatron coupling between horizontal and vertical oscillation. The betatron coupling exists mainly due to skew quadrupoles, sextupoles, and solenoid field components in the ring.

The resonances involving a synchrotron tune are called synchrotron sideband resonances and represents the phase modulation of the spin precession motion by the synchrotron oscillations.

2.6 Energy spread

The frequency modulation of spin precession leads to the appearance of satellite sidebands about the central line in the frequency spectrum. These satellite resonances are regularly spaced by the synchrotron tune. When the energy spread is significant due to the strong quantum excitation of orbit oscillations, the spread in spin tune is large. The satellites then become broad and strong and overlap with the main depolarisation resonance.

By taking into account the energy spread, an enhancement factor of depolarisation (the explicit expression can be found in [[52], [53]]) is introduced. It includes the influence of the synchrotron motion on the spin-orbit coupling vector $\Gamma = \gamma \frac{\partial \hat{n}}{\partial \delta}$ [54] and depends on the parameter called the synchrotron tune modulation index [55], [56] which is equal to:

$$\sigma = \frac{\nu}{\nu_s} \frac{\sigma_E}{E_0} \quad (2.16)$$

where ν and ν_s are the spin and the synchrotron tunes respectively and $\frac{\sigma_E}{E_0}$ is r.m.s value of the energy spread. As it is shown, the tune modulation index increases strongly with the beam energy and the energy spread.

A simple definition of the spin tune modulation is given by the number of sidebands inside the spin tune spread. According to N. Carmignani [57], who contacted studies on this phenomenon for electron storage rings, the detection of sharp sideband resonances is achieved when $\sigma \leq 1.5$. For the case of the DLS storage ring, the spin modulation index is equal to 1.5 ($\nu_s = 0.004$, $\nu = 6.8082$, $\frac{\sigma_E}{E_0} = 0.9\%$), and indeed the sidebands are well-separated by the main depolarisation resonance and do not reduce the total polarisation level.

According to studies at HERA [58], [59] as the tune modulation index increases, higher-order synchrotron sidebands become more and more significant.

Another reason that the spin satellites can overlap with the main resonance is that the synchrotron frequency is high ($Q_s \approx 0.1$) in high-energy electron storage rings [60]. A quantitative approach of the depolarisation due to was obtained by Ya. Derbenev and A. Kondratenko [61], C. Biscari et al. [54] for synchrotron resonances and by K. Yokoya [55] for synchrotron and betatron resonances. More studies were contacted by S. Mane for the Future Circular Collider (FCC) [62], and J. Buon for Large Electron Collider (LEP), whos demonstrates that the depolarisation enhancement due to beam energy spread is the primary concern when considering the possibility to obtain a high level of polarisation in high-energy electron storage rings [63].

2.7 Spin depolarisation

As is indicated in the previous section, since both Ω_c and α are known to high precision, measurement of Ω_{BMT} yields a very precise measurement of the beam energy. An oscillating radio-frequency magnetic field is applied in the horizontal plane to excite the beam. The RF-magnetic field oscillates at a frequency f_{dep} which is aliased with a multiple of the orbital revolution frequency f_{rev} :

$$f_{dep} = (k \pm [\nu]) \cdot f_{rev} \quad (2.17)$$

where k is an integer and $[\nu]$ is the non-integer part of the spin tune.

When the vertical excitation is in resonance with the spin tune, the spin-vector is tilted away from the vertical axis by a small amount in successive revolutions of the storage ring, gradually reducing the beam polarisation [64]. The figure Fig. 2.1 illustrates the spin vector rotation during depolarisation.

However, all the particles in the bunch are not affected with the same way during the resonant depolarisation. The particles in the bunch have some spread in the energies and consequently in the spin tune. Thus, during excitation, the beam is depolarised than simply rotate the polarisation vector.

Because the polarisation vector is the ensemble average over all spin vectors, the measured beam energy is to a very good approximation independent of betatron and synchrotron

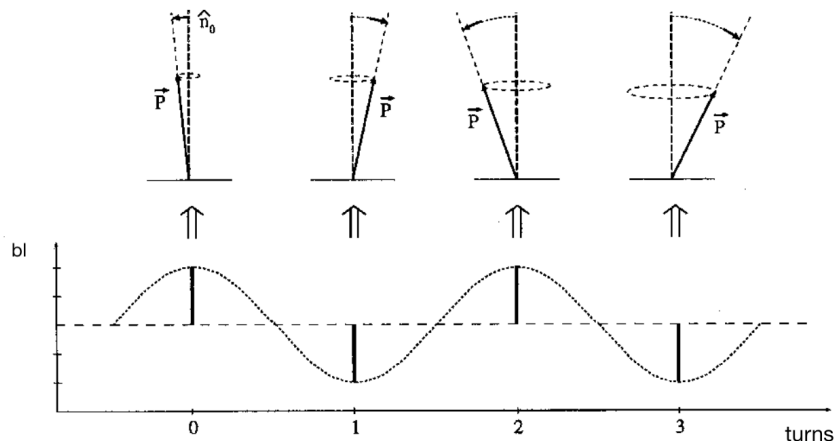


Figure 2.1: The polarisation vector is resonantly rotated away from the vertical direction when the perturbation is in phase with the nominal spin precession. The integrated magnetic field that is used to perturbate the spin is shown in the sinusoidal plot [64].

oscillations of the individual particles and is not limited in accuracy by the beam energy spread.

2.7.1 Froissart-Stora equation

The initially vertically polarised beam perturbed by a horizontal magnetic field can be depolarised when the perturbation induces a spin resonance. The Froissart-Stora formula describes the spin transport through a single resonance where the final polarisation is given by [10]:

$$f_{seq} P_y(\infty) = \left(2e^{-\frac{\pi|\epsilon|^2}{2\alpha}} - 1 \right) P_y(-\infty) \quad (2.18)$$

where ϵ is the resonance strength, α the rate of resonance crossing which is given as a function of the frequency step Δf_{RF} , the excitation time Δt and the revolution frequency f_{rev} by the equation $\alpha = \frac{\Delta f_{RF}}{2\pi f_{rev}^2 \Delta t}$. $P_y(\infty)$ and $P_y(-\infty)$ refer to the initial and final polarisation, respectively. This formula shows that if the resonance is very weak or is crossed very quickly ($|\epsilon|^2/\alpha \ll 1$), then there is almost no loss of polarisation. When the resonance is very strong, or is crossed very slowly ($|\epsilon|^2/\alpha \gg 1$), then the polarisation direction is flipped with almost no loss of polarisation. A large polarisation loss can occur when the crossing speed α is comparable to $|\epsilon|^2$ [65].

2.8 Touschek lifetime

The Touschek effect is a single scattering between two electrons of the bunch. Electrons inside a bunched beam undergo transverse betatron oscillations around the closed orbit and synchrotron oscillations with respect to a synchronous particle. In a reference frame moving with the electron bunch, the slow synchrotron motion can be neglected, and the electron motion becomes purely transverse. When two electrons with initially horizontal momenta collide (Møller scattering), the scattering process leads to vertical and longitudinal components. The longitudinal component is multiplied by the Lorentz factor to be transformed from the center-of-momentum system into the laboratory system. The energy of the scattered particle changes due to the transformation. If the induced energy deviation exceeds the energy acceptance of the storage ring, the electron can get lost [66], [13], [18]. The scattering cross-section is spin-dependent; hence the particle loss rate depends on the beam polarisation. The relation between Touschek lifetime τ , Touschek beam losses dN/dt and polarisation P is shown as [15], [18]:

$$\frac{1}{\tau} = -\frac{1}{N} \frac{dN}{dt} = \alpha_t [C(\varepsilon) + F(\varepsilon)P^2]N \quad (2.19)$$

$$\alpha_t = \frac{\sqrt{\pi}cr_e^2}{\gamma^3(4\pi)^{3/2}\sigma_x\sigma_y\sigma_l\sqrt{\epsilon_x/\beta_x}(\Delta p_m/p)^2}; \quad (2.20)$$

$$C(\varepsilon) = \varepsilon \int_{\varepsilon}^{\infty} \frac{1}{u^2} \left\{ \left(\frac{u}{\varepsilon}\right) - \frac{1}{2} \ln \left(\frac{u}{\varepsilon}\right) - 1 \right\} e^{-u} du \quad (2.21)$$

$$F(\varepsilon) = -\frac{\varepsilon}{2} \int_{\varepsilon}^{\infty} \frac{1}{u^2} \ln \frac{u}{\varepsilon} e^{-u} du \quad (2.22)$$

and

$$\varepsilon = \left(\frac{\Delta p_m/p}{\gamma} \frac{\epsilon_x}{\sigma_x} \right)^2 \quad (2.23)$$

where $\Delta p_m/p$ is the momentum acceptance, γ is the relativistic Lorentz factor, σ_x and σ_y are the horizontal and vertical beam size, ϵ_x is the horizontal emittance, r_e is the classical electron radius, σ_l is the bunch length and β_x is the horizontal beta function. For one measurement, the integrals can be treated as constants and have been evaluated using Mathematica for the case of DLS ring [67].

Since $F(\varepsilon)$ is a negative quantity, the Touschek lifetime increases with the electron beam's polarisation, while the beam losses decrease.

2.9 Simulation Studies and Calculations

Simulation studies were used to understand and model the process of spin polarisation and depolarisation for the Diamond Light Source case.

The working principle of the energy measurements is based on the polarisation of the beam. Thus, the estimation of the polarisation level is essential for this measurement. The SLIM code calculated the equilibrium degree of polarisation that can be achieved (Solution by Linear Matrices) [46]. SLIM determines the first-order spin resonances using a linear approximation to the spin motion.

For the depolarisation process, the spin tracking code FESTA (Fast Electron Spin Tracking based on Accelerator Toolbox) [57] was used to simulate the depolarisation of the electron beam. Various parameters of the depolarisation were simulated. The results were used as a guide later for the depolarisation experiment. In the end, the calculation of the first-order spin resonances strength ensures that the excitation strength is enough to depolarise the electron beam

2.9.1 SLIM

The equilibrium polarisation that can be achieved in a ring, in the real case where there are field imperfections, and closed orbit distortions, can be calculated using the SLIM code. The SLIM code uses a matrix formalism for a wide variety of storage ring designs and operation conditions. The orbital motion of an electron is described with six canonical coordinates $(x, x', y, y', z, \delta)$, where x, y are the horizontal and vertical position coordinates, z is the longitudinal coordinate relative to the bunch center, (x', y') are the horizontal and vertical conjugate momentum and $\delta = \Delta E/E_o$ is the relative energy error. In the linear approximation, the transformations of the six-dimensional vector are described by 6×6 transport matrices [68]. Spin motion can be included by adding two more spin coordinates (α, β) to form an 8×8 transport matrix. The magnet elements of the ring are modelled as thin lenses. The electron spin motion is tracked using the Derbenev - Kondradenko - Mane equation 2.11, [69] which calculates the equilibrium polarisation taking into account the radiative depolarisation due to photon - induced longitudinal recoils. However, nonlinear depolarisation effects such as those associated with spreads in the orbital frequencies cannot be included in the matrix method of SLIM.

2.9.1.1 Thin lens model

The lattice representation includes the sequence of the magnets with the geometrical dimensions and the magnetic strengths. For particle tracking, the input magnet lattice description for the SLIM code has to be symplectic. Symplectic lattice descriptions can be obtained by translation to a thin lattice. In the following equations, the comparison of the transfer matrix of a thick and a thin quadrupole is shown.

The transfer matrix for a quadrupole described as a thick element, at the transverse motion, in one degree of freedom, is [70]:

$$M_{thick} = \begin{pmatrix} \cos(l\sqrt{k}) & (1/\sqrt{k})\sin(l\sqrt{k}) \\ -\sqrt{k}\sin(l\sqrt{k}) & \cos(l\sqrt{k}) \end{pmatrix} \quad (2.24)$$

where k is the quadrupole strength and l is the quadrupole length. If the trigonometric functions are expanded in Taylor series:

$$M_{thick} = \begin{pmatrix} 1 - \frac{l}{2f} + \dots & l(1 - \frac{l}{6f} + \dots) \\ -\frac{1}{f}(1 - \frac{l}{6f} + \dots) & 1 - \frac{l}{2f} + \dots \end{pmatrix} \quad (2.25)$$

In the thin lens approximation it is assumed that the length of the quadrupole approaches zero $l \rightarrow 0$ while holding the focal length constant as $1/f = kl = \text{constant}$. Thus, the elements of the matrix in Eq. 2.25 are replaced with first order Taylor series terms ($\cos(x) \rightarrow 1, \sin(x) \rightarrow x$) and becomes:

$$M_{thin} = \begin{pmatrix} 1 & 0 \\ -1/f & 1 \end{pmatrix} \quad (2.26)$$

For the case where the quadrupole is described as a thin element that is placed at the centre of its length, the transfer matrix will result from the multiplication of a drift matrix with length equal to half of the quadrupole length, the transfer matrix of a thin quadrupole and one drift transfer matrix identical to the first one.

$$\begin{pmatrix} 1 & \frac{l}{2} \\ 0 & 1 \end{pmatrix} \begin{pmatrix} 1 & 0 \\ -1/f & 1 \end{pmatrix} \begin{pmatrix} 1 & \frac{l}{2} \\ 0 & 1 \end{pmatrix} = \begin{pmatrix} 1 - \frac{l}{2f} & l(1 - \frac{l}{4f}) \\ -\frac{1}{f} & 1 - \frac{l}{2f} \end{pmatrix} \quad (2.27)$$

The comparison between Eq. 2.27 and Eq. 2.25 demonstrated that if the ratio l/f is small, the thin lens approximation is in good agreement with the thick lens approximation. However, the diagonal elements introduce some errors that can be eliminated by replacing the thick element with several thin lenses. By splitting the integration into smaller steps, it is possible to obtain better approximations [71].

The accelerator elements are sliced into sufficiently short segments that can be represented by delta function "kicks". The most straightforward approach is to slice each accelerator component in equally spaced kicks, separated by drifts. For example, the transfer matrix of each quadrupole will be [72]:

$$M(n) = [M_d(L_n)M_{th}(K_n)M_d(L_n)]^n \quad (2.28)$$

where n is the number of slices, M_d is the matrix for a drift of length $L_n = L/(2n)$ where L is the length of the element, M_{th} is the transfer matrix of the element and $K_n = 2KL_n$ is the thin lens quadrupole strength where K is the quadrupole strength.

For the case of the bending magnet's modelling, the edge focusing due to the fringe fields should be included. Fringe fields appear in regions that lie at the edges of a magnet. The field does not suddenly change from zero to the nominal dipole field in the entrance and the exit of the dipole but follows a smooth rise and fall. This effect can be represented by two quadrupoles that have been placed at the entrance and the exit of the bending magnet with a strength equal to $k = -\tan(\delta)/\rho$, where ρ is the bending radius of the bend and $\delta = \theta - \zeta$. The term θ is the angle of the bend and ζ is the a correction term to account for the additional focusing due to the fringe fields. The term ζ depends on the full gap height of the dipole g , ρ and the fringe field integral (FINT parameter in most modelling codes) κ as [73] [74]:

$$\zeta = \frac{g\kappa}{\rho} \sec\left(\frac{\theta}{2}\right) \left(1 + \sin^2\frac{\theta}{2}\right) \quad (2.29)$$

2.9.1.2 TEAPOT slicing algorithm

For the case of this study, instead of using the normal slicing technique with equal spacing, a special algorithm according to the TEAPOT program for optics and tracking was used [75]. The TEAPOT algorithm improves the convergence of the (2,1) matrix element in the thin lens quadrupole 2.27 towards the true solution given by the thick quadrupole 2.25 [72] and results in better tracking accuracy. This slicing algorithm introduces the fraction of

the total length of the magnet L which is $\delta = \frac{1}{2} \frac{1}{1+n}$. The distance δL is between the first and the last slice to the edge of the magnet, where n is the number of slices. The distance ΔL separates each slice of the magnet. The two length proportions follow the condition:

$$2\delta + (n - 1)\Delta = 1 \quad (2.30)$$

The TEAPOT slicing can be written as [72]:

$$M(K, L, n, \delta) = M_d(L\delta) \times [M_{th}(K_n)M_d(L\Delta)]^{(n-1)} M_{th}(K_n)M_d(L\delta) \quad (2.31)$$

The description of an element starts with a drift of length δL , followed by $n - 1$ thin quads spaced by ΔL , and ends with a last thin slice at distance δL from the end. The multiple kicks due to multiple slices are equal. An illustration of the TEAPOT slicing using four slices ($n=4$) is shown in Fig. 2.2. The red dashed line corresponds to the total length of the element.

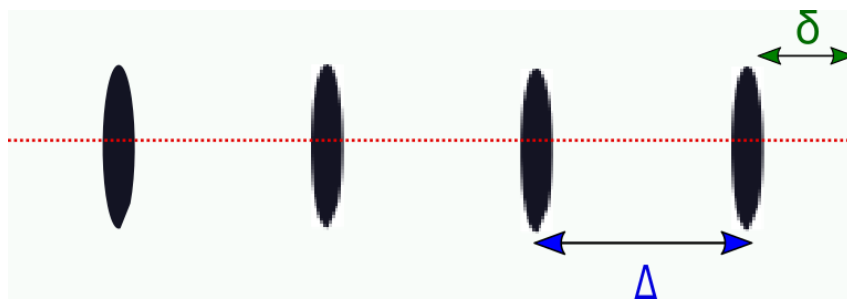


Figure 2.2: The thin lens representation of an element using the TEAPOT slicing for the case of 4 slices.

2.9.1.3 From thick to thin lens lattice

The conversion of a thick lens lattice to a thin lens can result in discrepancies on the betatron tune and the chromaticity between the two cases. The Methodical Accelerator Design (MAD) tool [76] was used to overcome this inconsistency. MAD was developed at CERN for lattice design and beam optics and calculates the global machine parameters like tunes, chromaticity and optics functions such as beta function and dispersion. Besides, it uses matching routines to provide numerical optimisation tools for adjusting magnet strengths and change the optics. The strength of a quadrupole doublet was adjusted to correct the horizontal and vertical tunes. After this correction, the lattice was used as

input in the SLIM code. To verify that SLIM calculations agree with the calculations by elegant [77] which is the tool used for the optics design in DLS, the betatron tunes, the chromaticity and the Twiss functions were compared.

2.9.1.4 Closed Orbit Distortions (COD)

As discussed in the previous chapter, the equilibrium polarisation deviates from the maximum value of 92% because of magnet misalignments and field errors in the realistic case. The magnet misalignment and field errors give rise to horizontal and longitudinal fields on the closed orbit and cause the spin axis to tilt away from its nominal direction. The closed orbit distortions are simulated in SLIM by using the corrector magnets of the storage ring. The corrector magnets were set with different random strengths, which eventually will create CODs in the ring.

2.9.1.5 Results

The results from the SLIM calculations are presented in this section. In the upper plot of Fig. 2.3 the polarisation level that can be achieved for different beam energies is shown. The second plot illustrates the calculation of the polarisation time. The resonance on the right reveals that when the spin tune ν_{spin} and the horizontal betatron tune ν_x meet the condition $\nu_{spin} + \nu_x = 35$ the polarisation degree can be significantly reduced. When the spin tune is close to the intrinsic resonance $\nu_{spin} + \nu_y = 20$, where ν_y is the vertical betatron tune, the beam can be depolarised strongly, as is illustrated by the resonance on the left in Fig. 2.3. The betatron, synchrotron and spin tunes of the Diamond ring are listed in Table 2.1.

Various simulated field imperfections give different results for the position and the width of the resonances, as shown in Fig. 2.4. The r.m.s. value of the introduced closed orbit

Table 2.1: Diamond storage ring parameters related to beam polarisation.

Parameter	Values	Units
Energy	3.014	GeV
Horizontal betatron tune, ν_x	28.189	-
Vertical betatron tune, ν_y	13.277	-
Synchrotron tune, ν_s	0.0041	-
Spin tune, ν_{spin}	6.840	-
Theoretical polarisation time, τ_{ST}	29.9	min

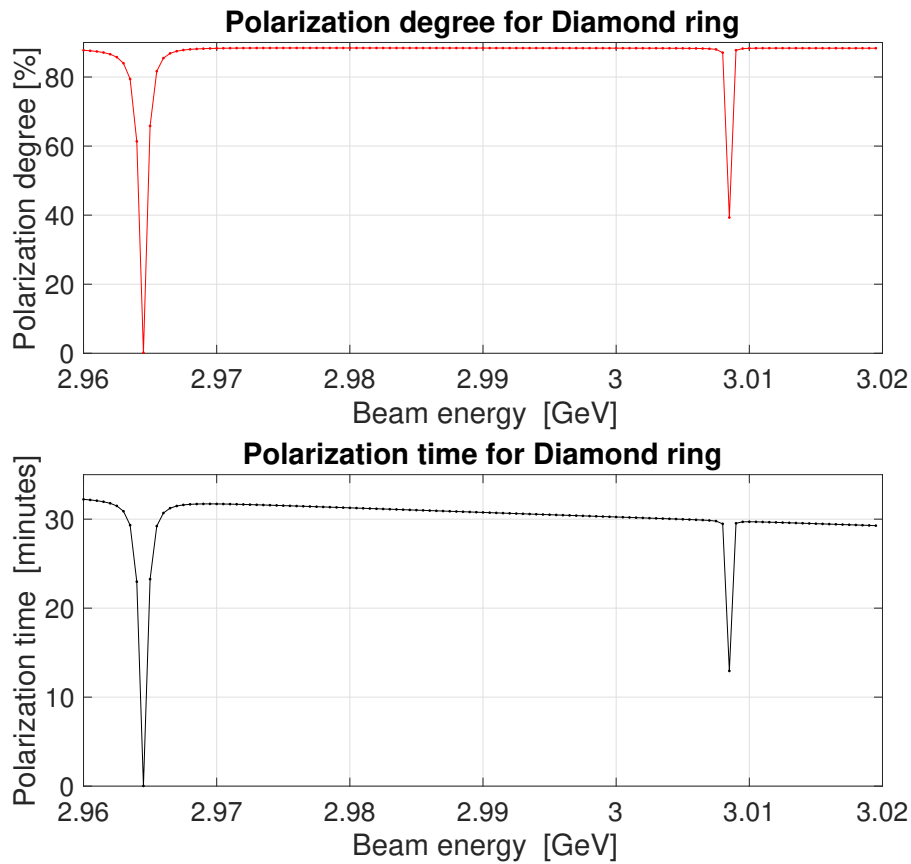


Figure 2.3: The polarisation level and the polarisation time versus the beam energy obtained from simulations with the SLIM code.

distortions estimates the simulated field imperfections. Since the spin depolarisation resonances appear in a short energy range and are far from the operational spin tune (6.84 for the DLS case), a high level of beam polarisation during operation can be expected. Only when the CODs are large (higher than 100 μm which is the case for DLS), the equilibrium polarisation is reduced by the resonances. These simulation results revealed that attention should be given to good orbit correction and that high-quality alignment of the magnets is mandatory. Also, the betatron tunes should be chosen carefully in order to avoid any destructive spin depolarisation resonances.

2.9.2 The FESTA code

FESTA (Fast Electron Spin Tracking based on Accelerator Toolbox) is a spin tracking code based on MATLAB and developed in the European Synchrotron Radiation Facility (ESRF) [78]. It was used to simulate the resonant spin depolarisation process. The spin

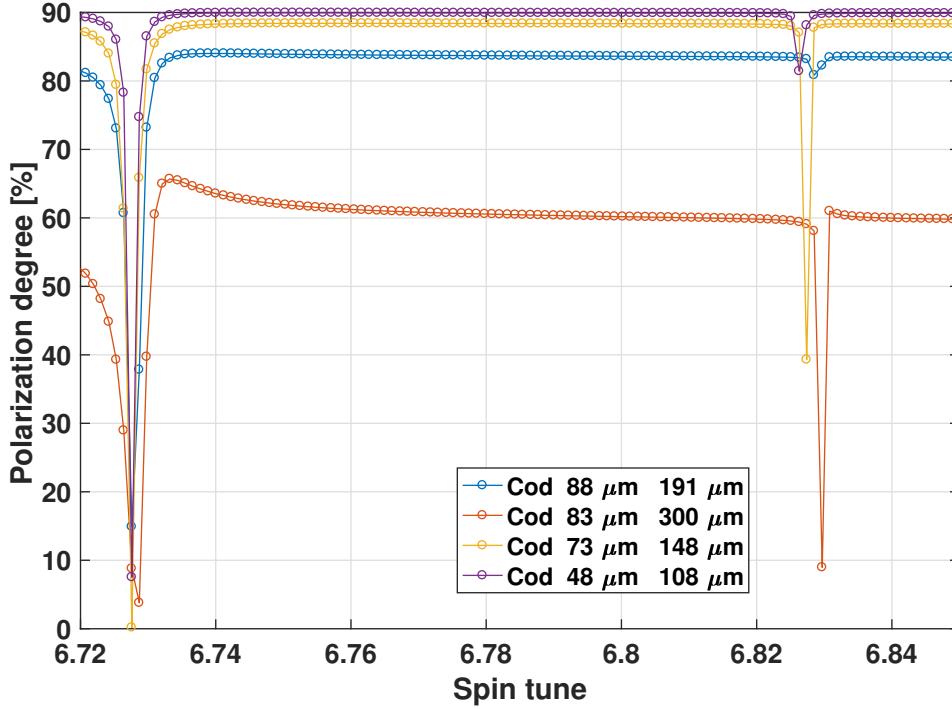


Figure 2.4: The polarisation level that can be achieved under different beam closed orbit distortions.

of a single electron is modelled as a point in a sphere, with two angle coordinates: θ and ϕ . FESTA uses the lattice description according to the Accelerator Toolbox and tracks the spin vector of many particles for a given number of turns under the effect of a vertical kicker. The signal given to the kicker is a sinusoidal signal with a given amplitude and a range of frequencies and is modelled as a rotation, around horizontal the direction, of an angle θ_x [79]: $\theta_x = 2\pi\nu_{spin}\theta_{kicker}$ where θ_{kicker} is the kick angle given to the electron from the kicker. Since the depolarisation time can be of the order of a few seconds and the particles to be simulated are of the order of 100, the code must be used in a cluster where some hundreds of processor cores can be used. The output is the calculation of the polarisation level after the excitation of the particles in different frequencies. For accurate modelling, four various phenomena were added to the spin dynamics, like the effect of the energy spread and the synchrotron oscillations, the radiation damping and quantum diffusion effects and the influence of kicker-induced orbit oscillations.

2.9.2.1 Depolarisation scan using FESTA

The FESTA code was the tool that was used mainly to investigate the depolarisation procedure. As the Froissart-Stora formula describes only the polarisation state before and after the depolarisation, a spin-tracking code was needed for this study. The simulation of depolarisation scans with different parameters each time answered questions regarding this phenomenon and contributed to the success of the experiment. A result of a depolarisation scan simulation is shown in Fig. 2.5. The initial polarisation level value was chosen to be 0.92, the frequency step 2 Hz, the excitation time of each frequency 2 s and the excitation strength $0.125 \mu\text{rad}$.

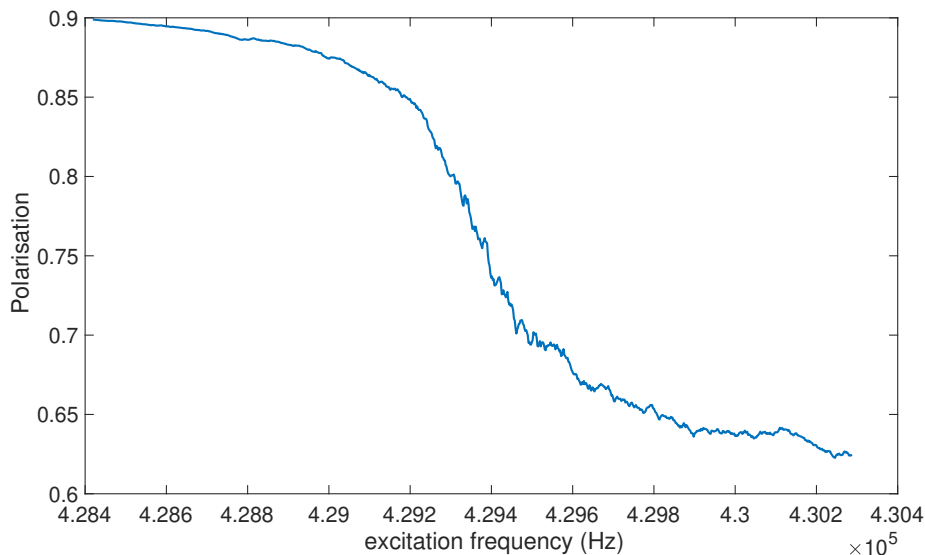


Figure 2.5: The depolarisation process calculated with the FESTA code.

The simulated polarisation level in each excited frequency was used to calculate the expected beam losses using Eq. 2.19. The ratio between the beam losses before and after the excitation is related to the beam's polarisation level beam after the excitation with the following relationship:

$$\frac{\left(\frac{dN}{dt}\right)_{fin}}{\left(\frac{dN}{dt}\right)_{in}} = \frac{a[C(\epsilon) + F(\epsilon)S_{fin}^2]N^2}{a[C(\epsilon) + F(\epsilon)S_{in}^2]N^2} = \frac{C(\epsilon) + F(\epsilon)S_{fin}^2}{C(\epsilon) + F(\epsilon)0.92^2} \quad (2.32)$$

In this relationship, we assume that the coefficients $C(\epsilon)$ and $F(\epsilon)$ are constants for a given measurement.

The calculated ratio of the beam losses according to the formula 2.32 is shown in Fig. 2.6.

At the horizontal axis, the excitation frequency was translated to energy values to demonstrate the high accuracy that the depolarisation method can provide.

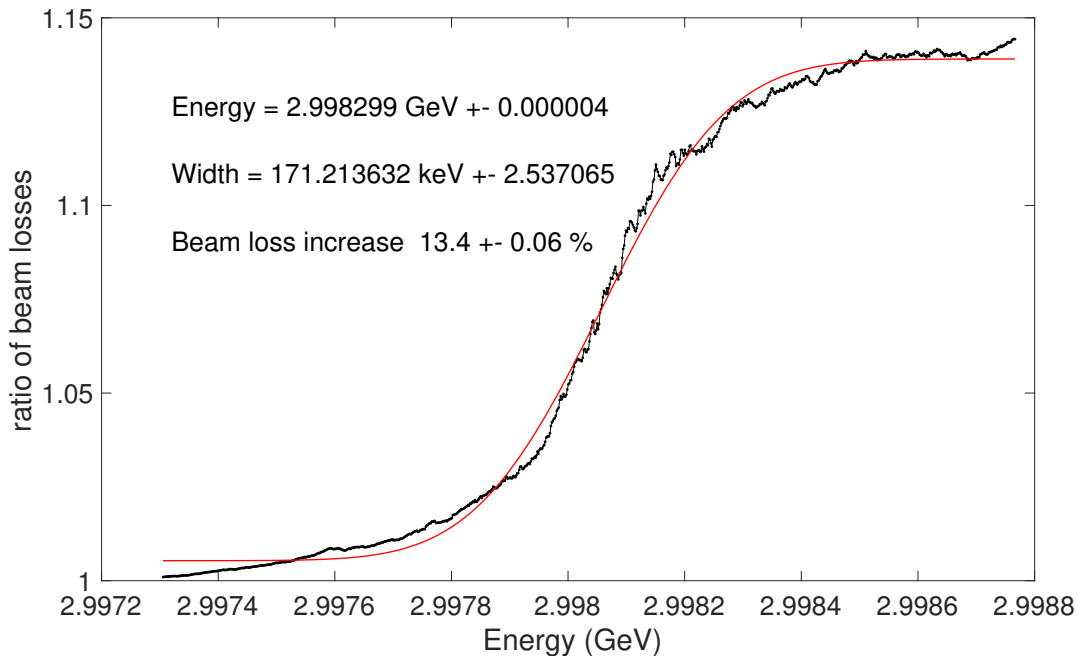


Figure 2.6: The calculation of the expected ratio between the beam losses of a depolarised and polarised beam is plotted in the black line. The error function fit used to model the data is plotted in the red line.

The simulated data were fitted with an error function fit by using the non-linear least squares analysis in MATLAB according to the equation:

$$f(x) = y_0 + a \times \operatorname{erf} \left(\frac{x_0 - x}{|w|/\sqrt{2}} \right) \quad (2.33)$$

where x corresponds to the energy range values, a is the beam loss ratio increase step, y_0 the mean value of the beam loss ratio, w the resonance width and x_0 the position of the beam energy which locates in the center of the error function curve. The errors correspond to the 95% confidence bounds calculated by MATLAB. To describe how well the error function model fits the set of the observations, the goodness of fit summarizes the discrepancy between observed values and the values expected. To evaluate the goodness of fit, the goodness-of-fit statistics were calculated using the Curve Fitting Toolbox software of MATLAB. The calculated parameters include the sum of squares due to error which measures the total deviation of the response values from the fit to the response values, the R-square, which measures how successful the fit is in explaining the variation of the data

and the root mean squared error which is an estimate of the standard deviation of the random component in the data. These calculations show that the data can be modelled by the error function fit, and the same approach was used in the experimental data.

The above analysis allows the comparison between the simulation and the experimental data from a depolarisation scan. The comparison showed that qualitatively the simulation describes well the depolarisation phenomenon. The beam loss ratio step due to depolarisation increases with stronger excitation, longer excitation and short frequency step. However, there was no agreement in the quantitative data. The width of the resonance was measured shorter than it was simulated. The beam loss ratio increase for the same excitation parameters was predicted higher than it was measured. This disagreement could be either due to the discrepancy between the excitation strength set in the simulation and the calculated integrated magnetic field in the stripline magnets. Another reason could be that the FESTA code was under development, and some phenomena were not included in the simulation, or some calculations needed more investigation. Nevertheless, the results from FESTA gave an essential input in this work as it demonstrated the right approach to depolarise the beam strongly.

2.9.2.2 Different resonance strengths

Scans with different frequency step, kicker strength and excitation time were simulated to investigate how the depolarisation resonance changes accordingly. These parameters were investigated as they are included in the Froissart-Stora equation ???. Fig. 2.7 shows an example of different scans using different excitation strengths. The excitation time was set to be 2s. High kick strength results in stronger depolarisation, wider resonances, and a higher increase in beam losses. Thus, strong depolarisation is needed in order to optimise the depolarisation measurement.

2.9.3 Spin response function

The magnetic field, generated by the stripline magnets, perturbs the spin and depolarise the beam. In addition, it affects the beam's orbital motion due to the excitation of vertical oscillations. The vertical oscillations of the beam drive the electrons into stronger or weaker fields of the focusing quadrupoles. The result is that the spin of the electrons is affected by the quadrupole fields, and the resonance strength can be enhanced, or

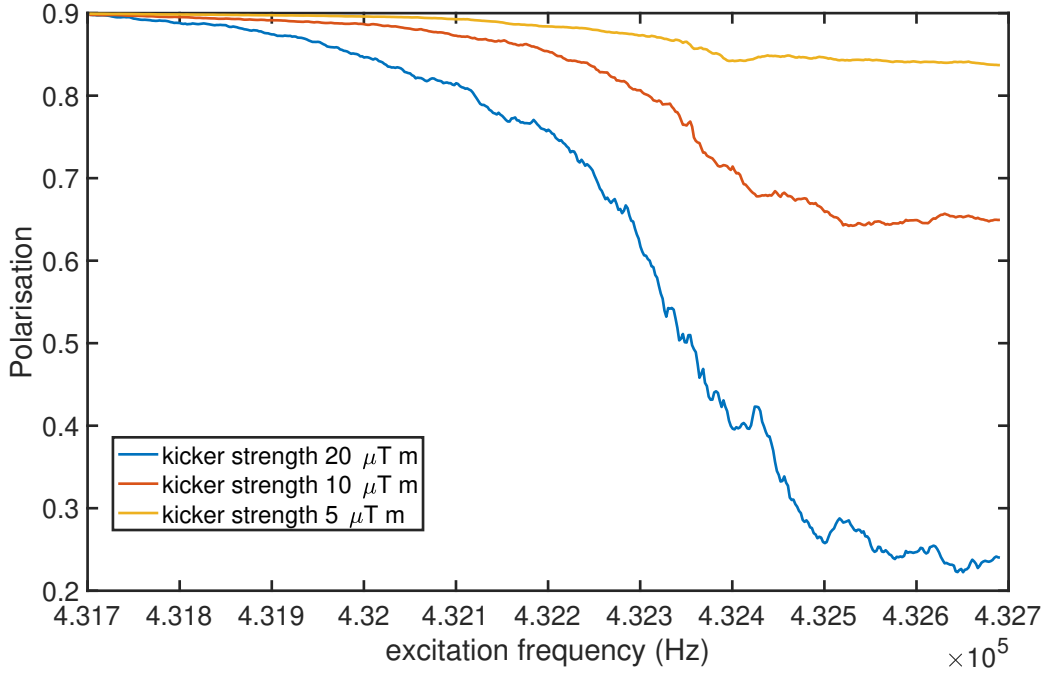


Figure 2.7: The depolarisation event using different excitation strengths calculated by FESTA.

diminished [80], [81], [82], [83]. The spin resonance strength, including both the direct spin kick and the spin-orbit coupling due to the induced coherent betatron oscillations, is given by the following formula [84]:

$$\epsilon = \frac{\phi_x}{4\pi} |F(\theta)| \quad (2.34)$$

where $\phi_x = \frac{\sqrt{2}}{B\rho} \int B_{rms} dl$ is the maximum angle of the spin rotation by the stripline magnets which produce an integrated magnetic field $B_{rms} dl$ and $|F(\theta)|$ is the spin response function. The spin response function can be determined by the magnetic structure of the ring and is calculated by the formula :

$$F(\theta) = \frac{e^{-i\nu\Theta}}{2i} \left[f_z \int_{-\infty}^{\theta} [\nu(\nu^2 + a)K_z^2 + i(\nu^2 - 1)K_z'] f_z^* e^{i\nu\Theta} d\theta \right. \\ \left. - f_z^* \int_{-\infty}^{\theta} [\nu(\nu^2 + a)K_z^2 + i(\nu^2 - 1)K_z'] f_z e^{i\nu\Theta} d\theta \right] \quad (2.35)$$

where the azimuth $\theta = s/R$ is defined by the arc-length s along the reference orbit and the radius of the ring R . For uncoupled orbital motion, denote the vertical orbital mode

by $f_y = \sqrt{\beta_z/R}e^{i\phi_y}$ where β_y is the vertical beta function that is shown in Fig. 2.8 and $d\phi_z/d\theta = R/\beta_z$. $K_y = B_y/B_0$ is the dimensionless scaled magnetic fields on the reference orbit and $B_0 = \frac{1}{2\pi} \int_{arc} B_y d\theta$ is a reference value given by the arc dipoles. The turning angle Θ is defined as $\Theta = \int_0^\theta \frac{R}{\rho(\tilde{\theta})} d\tilde{\theta}$ where ρ is the local bend radius in the horizontal plane. The ν is the spin tune. For DLS, the calculation of spin response function is illustrated in Fig. 2.9. As the function depends on the azimuth θ the function and consequently, the resonance strength varies along the ring. The kicker should be positioned in a location where the spin response function is high. Thus, the beam depolarisation measurement would profit as the beam can be depolarised quicker and with less excitation strength. The red vertical line shows the location of the kicker for the case of DLS. The spin response function F is equal to 0.4 at this position. This position, according to the calculation, is not favourable for strong and short depolarisation. However, the beam can still get depolarised but by a weaker depolarisation resonance.

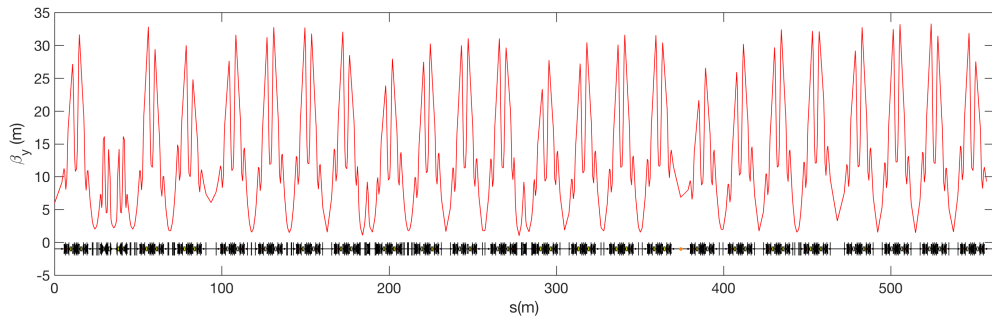


Figure 2.8: The vertical beta function along the ring.

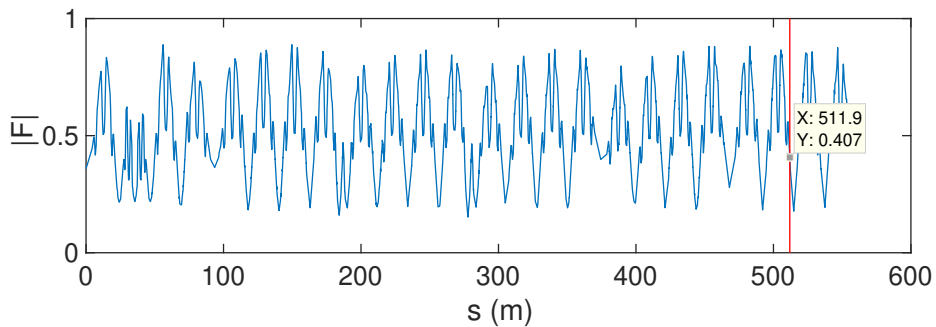


Figure 2.9: The Spin Response Function along the ring.

2.9.4 Summary

This chapter presents two simulation studies that have been carried out to study different parameters of the phenomenon of resonant spin depolarisation in the Diamond storage ring.

The SLIM code was used to calculate the expected polarisation level for the Diamond storage ring. The vertical and horizontal tunes should be chosen carefully to allow the beam to polarise to the maximum level of 92%. Closed orbit distortions could have destructive effects; however, due to the good alignment and the orbit feedback used during the operation of the machine, the CODs do not diminish the polarisation level strongly.

The FESTA code was used to test different scan parameters, and the results were used as a guide in the experimental studies. According to the FESTA results, the depolarisation level and the width of the resonance did not agree with the experimental results numerically. However, it gave results between the shape of the depolarisation resonance and the parameters of the frequency step, the kicker strength and the excitation time. These qualitative results contributed to the success of the experiment.

As the depolarisation resonance was not strong for Diamond, and a sensitive detection scheme is needed for the energy measurement, the question arose as to whether the kicker position is related to the strength of the resonance. The spin response function calculation shows that the effective strength of the kicker depends on its position in the ring. The setup could be optimised by choosing the kicker's location to be where the maximum of the spin response function is. However, the relocation of the kicker was not considered for the scope of this study. The calculation showed that the spin response function in the current location has a sufficient value for the beam depolarisation and explains why the resonance strength is not as strong as expected when the maximum excitation is applied.

Hardware Setup

The experimental setup of the energy measurements consists of the excitation scheme, which is used to depolarise the beam and the detection scheme with the beam loss monitors, which record the data and witness the depolarisation. Characteristics of the beam loss monitor system, like the material and the position of the detectors, were studied, and the performance of each detector is shown. The acquisition system used in this project and the newly added features are described. Later, the excitation scheme's details to make the energy measurements compatible with user operation are presented.

3.1 Theory of Beam Loss Monitors

3.1.1 Electromagnetic showers

An electron that leaves the bunch population interacts with the surroundings (beam pipe, collimators) and loses kinetic energy by excitation, ionisation or radiation. When an electron enters a medium, it creates an impulse to the atom electrons due to Coulomb forces. This impulse may be sufficient to raise the atom electrons to higher shells within the atom (excitation) or remove the electrons from the atom altogether (ionisation).

Fast electrons lose energy additionally by interactions with the Coulomb field of the nuclei of the transverse medium. If the electron decelerates in this field, a fraction of its kinetic energy will be emitted in photons and converted into radiation. This process is known as bremsstrahlung radiation.

The photons can interact with the matter by photoelectric absorption, Compton scattering and pair production.

In the photoelectric process, the photon interacting with the atom is absorbed by the atom. Then a photoelectron is ejected from one of the bound shells of the atom. The photoelectric process is the predominant mode of photon interaction at relatively low photon energies. Compton scattering happens between the incident photon and an electron in the absorbing material. The incoming photon is deflected through an angle θ with respect to its original direction and transfers a part of its energy to the electron, which is called Compton electron. The probability of Compton scattering decreases as the photon energy increases. In the pair production process, if a photon with energy higher than 1.022 MeV pass near the nucleus of an atom, it is subjected to strong-field effects from the nucleus and may disappear as photon and reappear as positive and negative electron pair.

At energies of 1 GeV and higher, electrons and photons initiate electromagnetic showers when they penetrate a material. Electrons lose their energy predominantly by radiation and pair production; pairs of electrons and positrons are produced and radiate more photons. A cascade of particles is created, increasing until the multiplication process reaches a maximum at a certain depth inside the absorber. Then the cascade development lessens, and two types of processes govern the electromagnetic shower. Firstly the electron and positron move away from the shower axis because of multiple scattering, and secondly, the photons and electrons produced in Compton scattering and photoelectric effect move away from the shower axis [85], [86].

3.1.2 BLM working principle

The observation of the electromagnetic shower is the most common method for detecting beam losses. The ionisation charge measurement, the fluorescence, the secondary emission current, the Cherenkov light or Compton electrons can be used to detect and monitor the losses. Thus, different types of beam loss monitors have been built to measure the above phenomena. The most common type of beam loss monitor detects light which is beam-induced in scintillators or Cherenkov radiators. This type of beam loss monitor was chosen for the studies of this thesis.

3.1.3 Scintillators

Different type of scintillators is used depending on the application. The two main categories of scintillators are organic and inorganic. In inorganic scintillators, scintillation arises because of the structure of the crystal lattice. In the organic scintillators, the fluorescence mechanism arises from transitions in the energy levels of a single molecule. Inorganic scintillators are usually made of high Z -elements and have a high density which enhances the photoelectric interaction. They are widely used in spectroscopy and in applications where high detection efficiency is needed, and low energy X-ray / Gamma-ray radiation has to be detected. Organic scintillators, which can be plastic or liquid, are made of low Z -elements and have a low density. This enhances the Compton scattering interaction with the ionizing radiation. Thus, they are used widely in high energy particle physics to detect charged particles and neutrons [87].

For the choice of a suitable scintillator for every application, several properties should be considered. The kinetic energy of the charged particles should convert into light with high scintillation efficiency (photons/1 MeV electron), and the light yield should be proportional to the deposited energy. The medium should be transparent to the wavelength of its emission for good light collection, and the index of refraction should be close to the value of the glass refractive index to allow efficient coupling between the scintillator and the photomultiplier tube. In the end, the rise and decay time of the induced luminescence should be short for fast applications and to avoid pile-up events [88].

3.1.4 Cherenkov radiation

Cherenkov radiation is produced when a charged particle is moving with constant velocity through the material medium greater than the phase velocity of light in this medium ($\beta n > 1$ where n is the refractive index, and β is the ratio of the velocity of the particle in the medium to that of light in the vacuum). The spherical wavelets of the field of the travelling particle interfere constructively to form a wake behind the particle as shown in Fig. ??.

The direction of emission of the Cherenkov radiation is :

$$\cos\theta_c = \frac{c}{v} \tag{3.1}$$

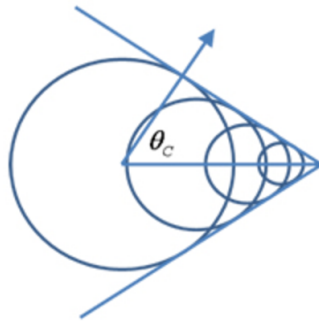


Figure 3.1: Interference of spherical wavelets produced by the particle passage through the medium creates a cone of Cherenkov light. [89]

The number of Cherenkov photons emitted per unit path length dx is [90]:

$$\frac{dN}{dx} = 2\pi\alpha z^2 \int \left(1 - \frac{1}{n^2\beta^2}\right) \frac{d\lambda}{\lambda^2} \quad (3.2)$$

for refractive index $n(\lambda) > 1$ and where z is the particle charge, α is the fine structure constant and λ is the wavelength.

Some properties of the Cherenkov detectors are:

- The light is emitted over a short time, and the pulse width is limited only by the photomultiplier tube that collects the light;
- They have low light yield;
- The yield of Cherenkov photons per unit wavelength is proportional to $1/\lambda^2$, but according to Eq. 3.2 only for those wavelengths where the refractive index is larger than unity. The emission is therefore concentrated in the short-wavelength region of the spectrum. In the X-ray region, there is no X-ray Cherenkov emission;
- There is a minimum energy threshold for electrons to produce Cherenkov light. This threshold prevents the detection of electrons with lower energy than the minimum threshold [91].

3.1.5 Photomultiplier tube

The photomultiplier tube (PMT) is an extremely sensitive light detector providing a current output proportional to light intensity. Photomultipliers are used to measure any process which emits light.

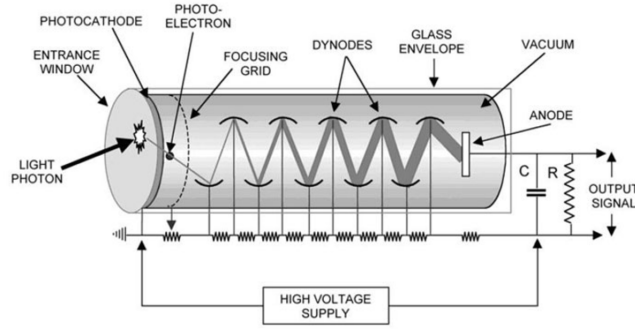


Figure 3.2: The photomultiplier structure [92].

Photons pass through the PMT entrance window, strike the photocathode, and release electrons due to the photoelectric effect, as is shown in Fig.3.2. An electric field between the photocathode and the first dynode accelerates the photoelectrons. A focusing grid directs the photoelectrons toward the dynode. The first dynode knocks out multiple electrons due to the phenomenon of secondary emission. Those electrons are then accelerated to a second dynode, and the same phenomenon repeats for several dynodes (usually 10 to 20), leading to a multiplication of electrons. At the end of the dynode chain is an anode or collection electrode. The current flowing from the anode to the ground is directly proportional to the photoelectron flux generated by the photocathode. The voltages needed to create the electric fields between dynodes to accelerate and focus the electrons in a PMT are most conveniently derived from a single high-voltage supply (500 to 3000 volts) and a voltage divider network. The setup is enclosed by a glass envelope and is in a vacuum. The PMT basic operating circuit is shown in Fig. 3.3.

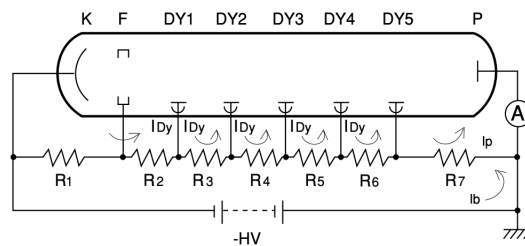


Figure 3.3: Photomultiplier operating circuit [93].

A high voltage is applied between the anode (A) and the cathode (K). The voltage-dividing resistors provide a proper voltage gradient between the photoelectron focusing electrode (F) and the dynodes (DY). The current flowing each resistor is the difference

between the divider current I_b and the dynode current I_{Dy} flowing in the opposite direction through the voltage-divider resistor. The anode current I_p and dynode current I_b act to reduce the divider current and the accompanying loss of the interstage voltage becomes significant in the latter dynode stages, which handle larger dynode currents. However, when the incident light intensity increases, the resultant anode and dynode currents are increased, and the voltage distribution for each dynode in the earlier stages increases. This results in a collective increase in current amplification in the early stages. Eventually, the voltage between the last dynode and the anode decreases. Therefore, the anode's secondary-electron collection efficiency degrades and leads to a saturation problem of the anode.

3.1.6 PMT characteristics

The PMT characteristics should meet the requirements of the application. Some important characteristics that should be considered are [93]:

- The basic characteristics of the photocathode. These include luminous sensitivity and spectral response characteristics.
 - * The spectral response characteristics show the dependency of the photocathode sensitivity to the incident light wavelength and are expressed as radiant sensitivity and quantum efficiency. Radiant sensitivity is defined as the photoelectric current generated by the photocathode divided by the incident radiant flux at a given wavelength, and its unit is amperes per watts (A/Watt). Quantum efficiency is defined as the ratio of the number of the emitted photoelectrons by the cathode to the number of photons incident on the window. It is expressed as a percentage.
 - * Luminous sensitivity is a convenient parameter to express the spectral response of a PMT since the spectral response measurement is expensive.
- The basic characteristics of dynodes, which are the collection efficiency and the gain.
 - * Collection efficiency refers to the probability that photoelectrons will arrive at the effective area of the first dynode where the electrons can be multiplied successfully to the next dynode stages.

- * The gain or current amplification G of a PMT is the ratio of the anode current to the photocathode current. It varies as a power of the supply voltage and $G^2 = (V_2/V_1)^{aN}$ where V_2 and V_1 are the supply voltages in the anode and cathode, respectively, a is a coefficient (0.6 to 0.8) set by the dynode material and geometry, and N is the number of dynodes.
- The linearity which describes the output distortion with the increasing of the incident light intensity at a given gain. If the incident light is very strong, the output will deviate from the linear response.
- The dark current which is a small output current produced by a PMT is total darkness. The leading causes of dark current are: Ohmic leakage between the electrodes on the glass and the insulating surfaces of the tube, thermionic emission of single electrons from the cathode, field emission due to imperfections in electrodes in the presence of high electric fields, and radioactivity since some parts of the PMT contain radioactive isotopes.
- The time characteristics, which include the rise time, fall time and electron transit time. The rise time is defined as the time required for the anode current to increase from 10% to 90% of its peak pulse height. The fall time is defined as the time required for the anode current to decrease from 90% to 10% of its peak pulse height. Transit time is the times that takes a light pulse in the cathode to be converted and collected as a current in the anode.

Some additional usage considerations are the existence of magnetic fields or ambient light in the location of the PMT's installation. Strong magnetic fields can curve electron paths, steer the electrons away from the dynodes and cause loss of gain. Ambient light can increase the dark current. Suitable shielding should be used in each case [94].

3.1.7 Matching of scintillator and PMT

The scintillation light is transported from the scintillator to the PMT via light guides. The main process of light transport is the total internal reflection. The scintillator light is emitted in all directions, and only one small fraction can reach the PMT window directly. The remainder is reflected on one or multiple times in the scintillator surfaces [91]. If the angle of incidence θ is greater than the critical angle of θ_c , the total internal reflection will

occur. The critical angle is given by the equation:

$$\theta_c = \sin^{-1} \frac{n_1}{n_0} \quad (3.3)$$

where n_0 , n_1 are the indices of refraction for the scintillation medium and the surrounding medium respectively. Two effects arise in practical cases that lower the light transport efficiency, the optical self-absorption within the scintillator and the losses at the scintillator surfaces. A reflective material like aluminium foil can enhance the reflection of the light but with some higher absorption. The scintillation counter must be shielded from ambient room light. Other important considerations for the matching of the scintillator with the PMT are [95]:

- The matching the size of the light guide and the photocathode;
- The use of optical grease between the light guide and the PMT;
- The emission spectrum of the scintillator and the spectral response of the PMT should match.

3.2 Detection system

A study of the beam loss monitor system that is going to be used for the energy measurements was carried out. The main characteristic of the beam loss monitors for optimisation is the count rate. As the counting follows Poisson statistics, a high count rate results in a small measurement error. Thus, the leading objective of this work was to build a beam loss detector that gives the highest count rate.

This study included the position for the installation of the beam loss detectors along the storage ring. The detectors should be installed in a location where most of the losses happen due to Touschek scattering. Also, the material of the detectors should be sensitive and detect the highest fraction of the electromagnetic shower created by the lost particles. The system should be protected from the background noise and the acquisition system should be optimised to count most of the pulses.

3.2.1 Position of the detectors

The detectors should be positioned, such as to detect the maximum number of Touschek particles. Touschek particles transfer high momentum from transverse to longitudinal motion, exceed the longitudinal acceptance limit and are lost in areas with high dispersion, which follow sections where a high particle density was reached [95].

The beam loss rate in locations with high dispersion and big physical aperture was compared with lower dispersion and small physical aperture locations. The increase of the beam losses produced during the energy measurement is small. Thus, the precision of each beam loss measurement should be optimised. For this reason, the small physical aperture enhances the detection of the lost particles, as a stronger electromagnetic shower is created when the lost electron hits the beampipe.

For this study, the area downstream of the collimators was chosen for the installation of the detectors, as this is the location with the most significant ratio of horizontal dispersion to physical aperture. This location gave the highest count rate, and the depolarisation resonance was detected with much less noise. The detectors installed in other locations with higher dispersion but a much bigger physical aperture could detect the resonance but with much more noise. The drawback of this location is that due to the small physical aperture in the collimators, electrons lost from Coulomb scattering are detected additionally. However, these background losses did not affect the energy measurements as the new method of normalising the beam losses from different parts of the beam cancels out the background noise. This approach is further explained in chapter 4.

3.2.2 Radiochromic film measurements

The radiation footprint in the location where the detectors would be installed was measured using a radiochromic film. This measurement identifies the area where the highest fraction of the beam losses occurs and determines the detectors' dimensions that are going to be built. The radiochromic film Gafchromic RTQA2 [96] consists of a double layer of radiation-sensitive organic microcrystal monomers on a thin polyester base with a transparent coating, as is shown in Fig. 3.4. Usually, it is used for radiotherapy sources testing and therapy equipment commissioning, but it was well-suited to the present study as it can be placed easily in the area of interest. The darkening which depends on the received dose, can be translated in dose without any need of processing.

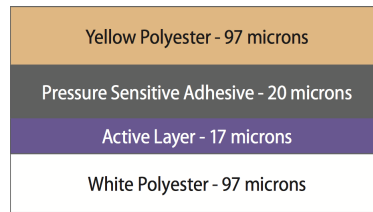


Figure 3.4: The radiochromic film layers.

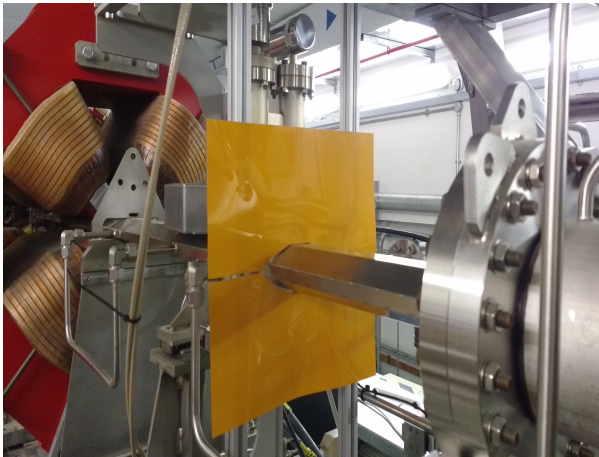


Figure 3.5: Radiochromic film installed in the storage ring.

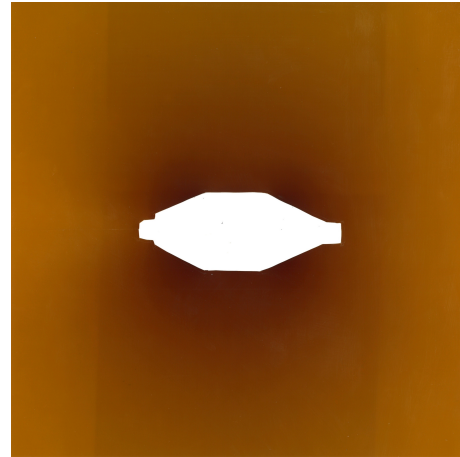


Figure 3.6: Radiochromic film darkening after one week exposure in the electron beam.

The film had been cut and shaped to fit around the beam pipe. Then it was installed in the storage ring, as is illustrated in Fig.3.5. The film was exposed one week to the radiation created by the electron beam, and the results are shown in Fig.3.6.

The exposed radiochromic film was scanned, and the picture was analysed using MATLAB. From the image, the values of the red, green and blue components were extracted. For the calculation of the dose, calibration data were provided by the diagnostics group of the synchrotron SOLEIL, who performed similar studies with the same radiochromic film [97].

At SOLEIL, seven films were exposed to various doses from 23 to 1526 mGy, and the amplitude of each colour component of the images was calculated. In Fig. 3.7 the percentage of each image colour versus the dose is plotted and fitted. The fit was used to extrapolate the colour amplitude data for a higher dose. The red colour calibration was used to calculate the dose of the irradiated film due to higher sensitivity compared to the other colours from the three curves. The calculated dose is presented in Fig. 3.8. The radiation in the area close to the beam pipe is high and fades further. The detectors' dimensions were chosen accordingly to cover the darkened area of the exposed radiochromic film.

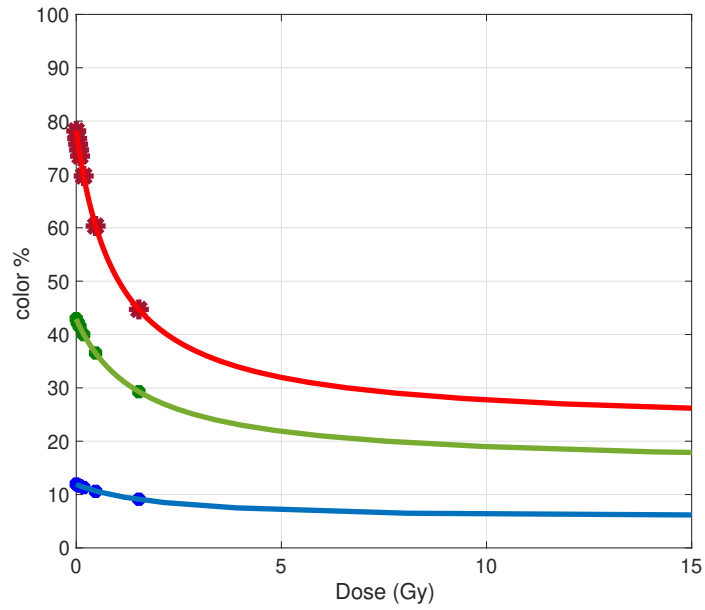


Figure 3.7: The calibration curves that were used for the calculation of the dose from the exposure of the radiochromic film GaFchromic RTQA2.

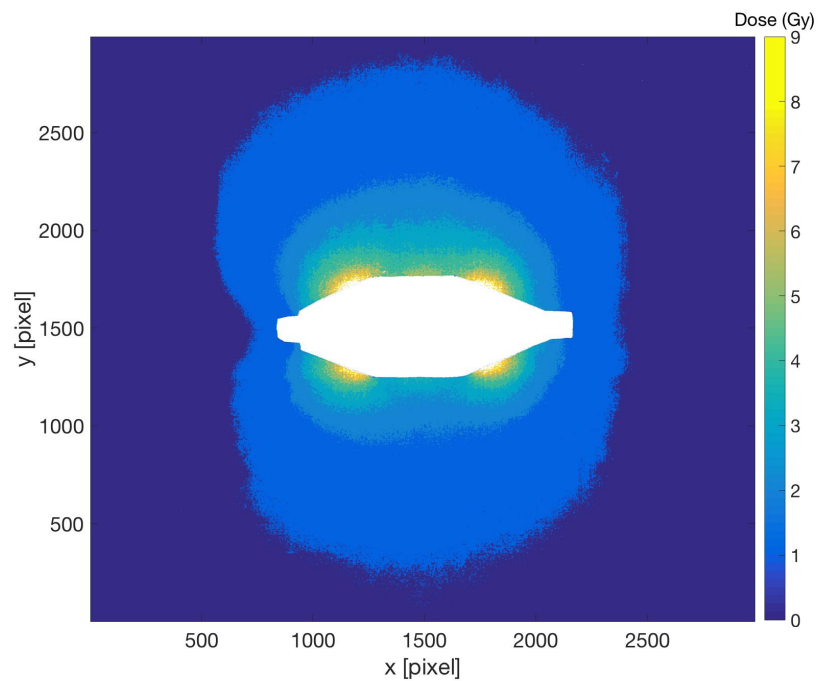


Figure 3.8: The radiation dose around the beam pipe is used as a guide to design the detector geometry in order to capture the highest fraction of the beam losses.

3.2.3 Comparison of three detectors

The most common method of detecting beam losses is detecting light produced by scintillators or Cherenkov radiators. The produced light can be collected by photodetectors which provide a current output proportional to the light intensity.

In this study, three different detectors were studied and tested. At Diamond, the detectors of the existing beam loss monitors were made from polymethyl methacrylate (PMMA, commonly known as acrylic glass). Two more detector materials were tested to find a more sensitive material that produces higher light output when a charged particle interacts with it. For this reason, the performance of the organic plastic scintillator EJ204 [98], and fused quartz used as a Cherenkov radiator were considered. The Scintillator EJ204 has high efficiency, high speed (with a decay time of 1.8 ns), attenuation length of 160 cm and wavelength that matches with the bialkali photocathode of the attached photomultiplier. However, the scintillator is sensitive to X-rays produced by the synchrotron radiation. As a Cherenkov radiator, the fused quartz outputs light instantaneously with a continuous spectrum without interacting with background X-rays, making the fused silica detector a good candidate for this study.

The three materials were rod-shaped with 15 cm length and 3 cm diameter. The size of the detectors was determined by the physical limitations of the installation area.

They were attached to the same model of end window photomultiplier (Electron Tubes ET 9126) with 29 mm diameter, and a blue-green sensitive bialkali photocathode [99]. The spectral response of the PMT is between 280 nm to 630 nm and is well-matched with the wavelength of the maximum emission from the scintillator, which is 408 nm. The single electron rise time of the PMT is 4.5 ns.

The monitors were installed in the storage ring 1 m downstream from the vertical and horizontal collimator set. They were placed about 2 cm above the beam pipe where the radiation distribution is within the same level according to the radiochromic film results. A sheet of 1.3 mm thick lead was used to protect the detectors from background ionizing radiation.

The comparison of the three detectors was based on the number and the shape of the pulses. A complementary consideration for the choice of the material was the vendor companies' capability to provide the desired design of the detectors within a price that matches the project's budget.

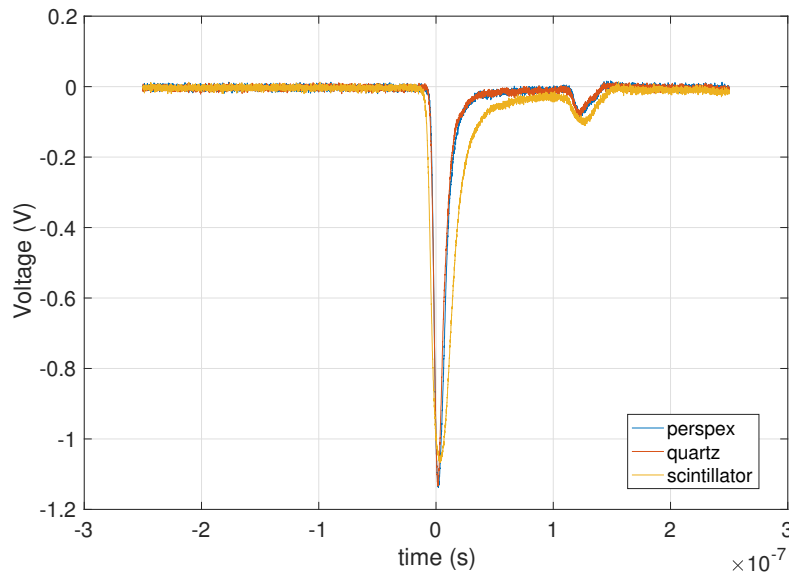


Figure 3.9: The pulses created by the three different detectors.

3.2.4 Detector pulses

For the future detector's design for the energy measurements, sharp pulses would benefit the counting algorithm. For this reason, the output pulse of each detector accompanied by the PMT module was studied. The detectors were placed in the storage ring, with the beam running under user operation mode. The pulse of the detectors was recorded using an oscilloscope, and the data can be seen in Fig. 3.9. The Full Width Half Maximum (FWHM), the drop and rise times were measured to characterise the pulses. The drop and the rise time were defined as the mean time difference between the 90% and 10% amplitude of the pulse. These parameters were compared for the three detectors shown in Table 3.1. The scintillator has wider pulses and a longer rise time than the other two detectors. This is because of the exponential nature of scintillation. The perspex and the quartz detector produce similar pulses. The afterpulse, which is created by the three detectors, was also investigated. The product of the time difference between the two pulses and the propagation speed of light in the cable was found to be twice the length of the connection cable (RJ58). This indicates that the pulse was created by a reflection at the connection with the oscilloscope.

	Perspex	Quartz	Scintillator
FWHM	10.3	9.3	20.1
Rise time (ns)	4.6	5	7.3
Fall time (ns)	15	14	29.8

Table 3.1: Key parameters of the pulses produced by the three different detectors.

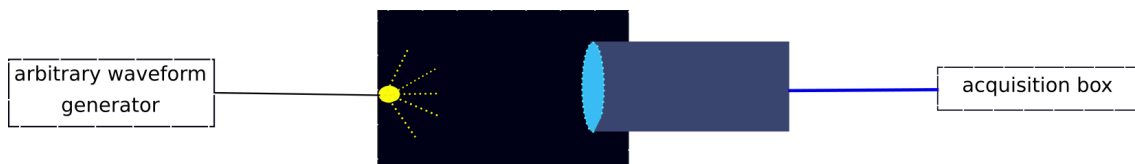


Figure 3.10: The lab setup for the calibration of the PMTs.

3.2.5 Photomultiplier calibration test

The three materials were attached to the same model of the PMT module. The PMTs were incorporated in a photodetector module, including a voltage divider circuit and a high voltage power supply circuit. Each PMT behaves differently for the same voltage gain setting, as they have different voltage dividers. Thus, a calibration test was conducted in the lab of the Diagnostics group of DLS to demonstrate the difference between each PMT performance. A light-emitting diode (LED), which produced a controlled intensity of light, was used. The LED was fixed at one end of a black opaque cylindrical box. The photocathode of each PMT was placed at the opposite side, as is shown in Fig. 3.10. The signal output was measured directly from the PMT's anode and was digitised using the acquisition system described in section 3.3. The ADC data were averaged over ten consecutive ADC samples. The voltage gain of each PMT was varied, and the integrated ADC signal was recorded. In Fig. 3.11, the maximum level of the ADC data is plotted for each voltage gain applied in the PMTs. The divergence between these curves was taken into consideration to compare the performance of the three detectors.

3.2.6 Counting performance

The beam losses are measured by counting the pulses that are produced by the three detectors. The calculated dose around the beam pipe given by the radiochromic film was used to find an area where all the detectors would receive the same radiation. A beam with 300 mA current was set in the storage ring, and the count rate of the three detectors was recorded for different gain voltages in the photomultiplier. The same scan was repeated

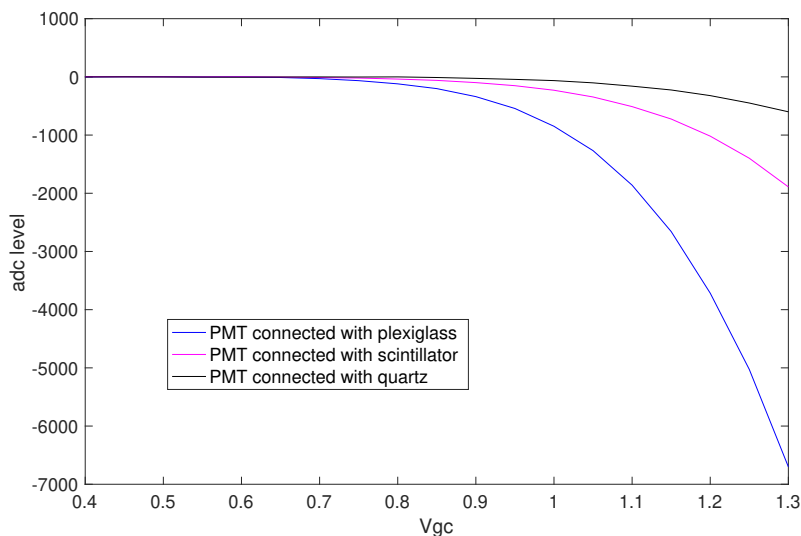


Figure 3.11: The integrated ADC signals acquired from the three different PMTs versus different voltage gains.

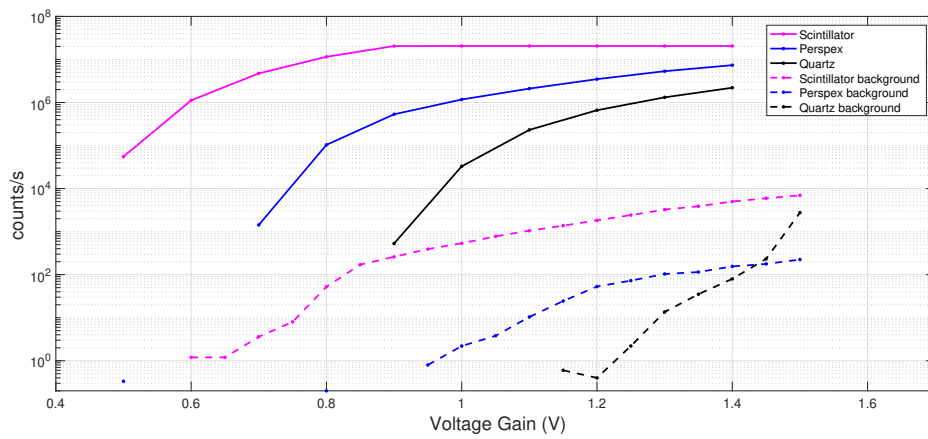
while there was no beam in the storage ring, and the background data were acquired as is shown in Fig. 3.12a. The background data, also shown in the same figure, are created by the dark current of each photomultiplier for different voltage gains and are considered noise in the detectors' counting rate. The error of each measurement is very small, and the error bars fail to represent them as their size is smaller than the size of the marker in the plot. The signal-to-noise ratio (SN ratio) is used to compare the performance of the three detectors. The calculation of the SN ratio (R) for counting is based on the equation [100]:

$$R = \frac{N_s \sqrt{T}}{\sqrt{N_s + 2N_b}} \quad (3.4)$$

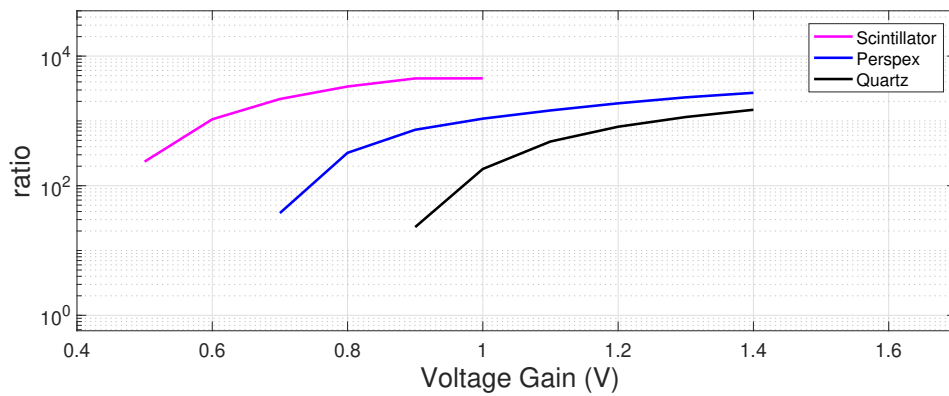
where N_s is the number of *counts/s* resulting from incident light per second, N_b is the number of *counts/s* resulting from background light per second and T is the measurement time. The results are shown in Fig. 3.12b.

3.2.7 Choice of detector

The scintillator presented the highest count rate in comparison with the other two detectors. This was the essential criterion for the choice of the detector. The scintillator's wide dynamic range allows the detection of weak and high beam losses by adjusting the gain voltage in the PMT. The ease of manufacturing the detector in the desired shape and the cost were two more advantages that the scintillator could offer.



(a) The count rate of the three materials for different voltage gains (solid lines). The dashed lines correspond to the recorded count rate without beam in the machine.



(b) The signal to noise ratio of the three different detector materials being considered.

Figure 3.12: Comparison of counting rate for the three detectors.



Figure 3.13: The lead shielded detectors installed in the storage ring.

However, the scintillator's high light output can damage the PMT, and careful settings of the PMT gain should be used. Further studies were conducted to characterise the scintillator behaviour and avoid saturation. Also, the higher sensitivity of the scintillator in X-rays compared with the other two detectors was studied further.

The Cherenkov detector and perspex did not outperform the scintillator. However, the results showed good counting performance and signals with short pulses. Another advantage is that the Cherenkov detector did not need shielding from X-rays. However, the manufacturing of these detectors in a custom shape was challenging, as the collaboration with the vendor companies was not successful. Based on these criteria, the scintillator was chosen as the detector for the beam loss monitor design for the energy measurements.

3.2.8 Lead shielding

The beam loss system should be protected from the synchrotron radiation produced by the bending magnets and the insertion devices, as we are interested only in the electromagnetic shower produced by the beam losses. For this purpose, a sheet of lead was used. Due to its malleability, the lead was easily shaped in the DLS diagnostics lab to cover the scintillator detectors. The shielding of the detectors is shown in Fig. 3.13. This study was focused on the scintillator detector since the quartz detector can create Cherenkov radiation only by charged particles. The main question to be answered through this work is about the

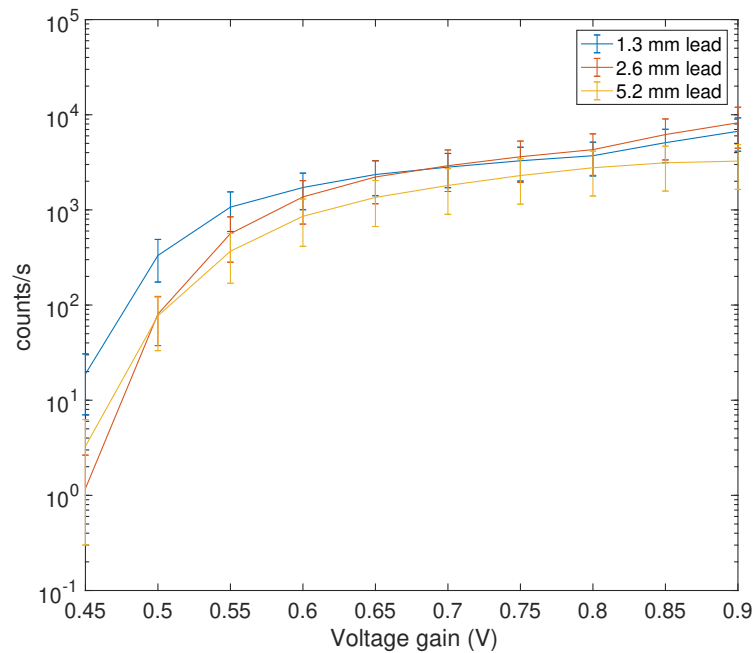


Figure 3.14: The count rate for different voltage gain as the lead thickness changes.

lead's thickness: it should be enough to protect the system from X-rays but not so much that it will reduce the count rate produced by the beam losses. An experimental study investigated whether the lead's thickness caused a large difference in the count rate for each case. Count rate data were taken for different voltages for 1.3 mm, 2.6 mm and 5.2 mm thickness of the lead sheet. Fifty different measurements were taken for each voltage gain, and the mean value is plotted, as is shown in Fig. 3.14.

The data was taken with separate beams for each lead thickness. Different beam conditions can result in different beam losses. Thus, an additional beam loss monitor was used to witness the differences between the different tests to normalise the data. When the lead thickness increases, the count rate tends to decrease. However, this difference is in the range of data errors. The data errors were defined as the standard deviation of each measurement. Since the experimental data do not show notable discrepancies between the three data sets, it was decided to adopt the 1.3 mm lead sheet as a good choice to protect the detectors from X-rays while simultaneously avoiding the risk of blocking the detection of beam losses.

3.2.8.1 Calculation of synchrotron radiation X-rays

The transmission of the synchrotron radiation X-rays through different lead thickness was calculated. The main source of the synchrotron radiation, where the detectors are placed, is the bending magnet. Synchrotron radiation occurs in a narrow cone of nominal angular width $1/\gamma$. An important quantity that can characterize its properties is the flux which is defined as the total number of photons per second per unit 0.1% bandwidth. The observation angle in the horizontal and vertical plane θ and ψ are used to describe the angular distribution of the radiation. The intensity distribution then provides information about the angular collimation of the flux and determines the fraction of the source flux transmitted by an angular aperture. When it is integrated over the vertical angle, and the horizontal angle is equal to 1 *mrad*, is given by the formula [101]:

$$I[(Watts/eV)] = 2.458 * 10^{13} I[A] E[GeV] \frac{E}{E_c} \int_{E/E_c}^{\infty} K_{5/3}(\eta) d(\eta) \quad (3.5)$$

where I is the beam current, E the beam energy. E_c is the critical energy of the bending magnet which characterises the width of the spectrum and is defined by the equation $E_c = 3\gamma c/2\rho$, where ρ is the radius of instantaneous curvature of the electron trajectory. $K_{5/3}$ is the modified Bessel function. In Fig. 3.15 the intensity spectrum of the bending magnet is shown.

The transmitted X-ray intensity by a sheet of lead is given by:

$$I = I_0 e^{-\mu t} \quad (3.6)$$

where I_0 is the incident intensity, I is the (reduced) intensity after travelling a distance t through the material and μ is the absorption coefficient. Its value varies with the atomic composition (increasing with the atomic number) and X-ray wavelength (increasing with wavelength).

In Fig. 3.15 the transmitted synchrotron radiation spectrum through a sheet of 1.3 mm, 2.6 mm and 5.2 mm lead are shown. Shielding the detectors with 1.3 mm sheet of lead blocks the synchrotron radiation allowing only a fraction of 2×10^{-21} of the total radiation power from the bending magnets to transmit. Thicker lead sheets are not needed. This result explains the experimental data where the count rate does not change with thicker lead shielding. These results were compared and are in good agreement with the

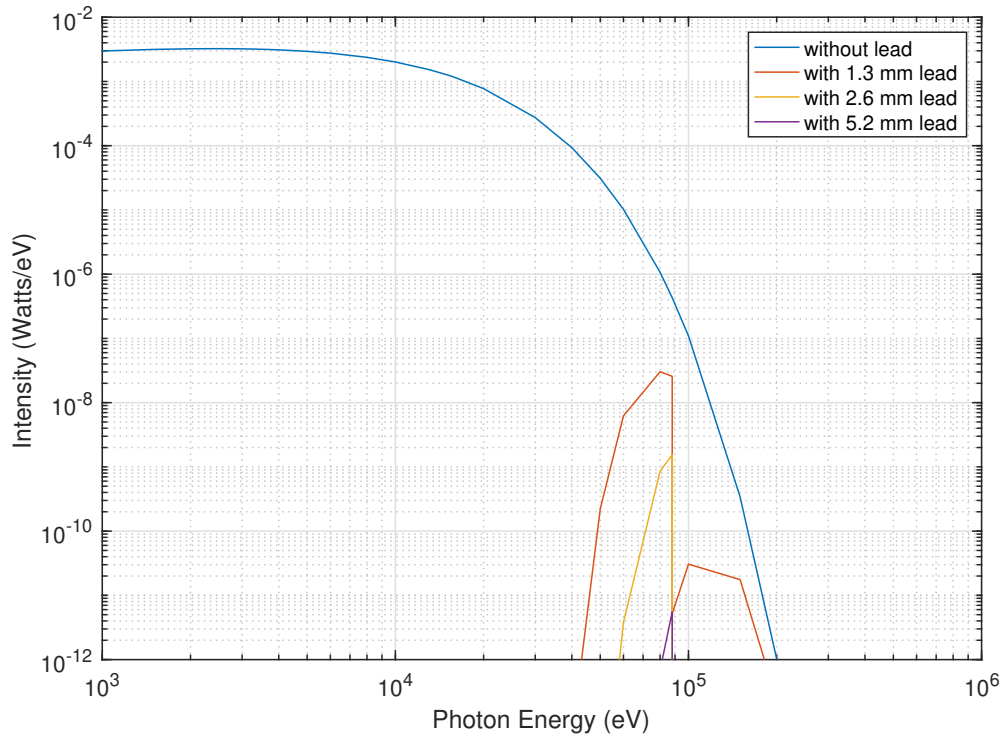


Figure 3.15: The intensity spectrum of the bending magnet is shown in the blue line. The transmitted synchrotron radiation spectrum through a lead sheet of 1.3 mm, 2.6 mm and 5.2 mm are shown in the red, yellow and purple line respectively.

calculations by the *XOP* code [102] which is software for simulations and ray-tracing for hard X-ray optics developed at ESRF.

3.2.9 Scintillator performance for different beam currents

According to the working principle of the PMT, the emitted light causes the emission of photoelectrons in the photocathode, which later are multiplied and create an amplified signal. However, when the light is intense, the produced photoelectrons can saturate the PMT's anode, as explained in 3.1.5. The PMT can go into a breakdown or permanent damage with continued exposure to intense light. The scintillator's performance was studied by changing the beam current of the machine in steps and consequently the produced beam losses. This test demonstrated the highest intensity that the PMT can handle. The results are shown in Fig. 3.16. For low beam currents, the PMT gain voltage can be set up to 1.5 V. However, when the beam current increases, the PMT starts to saturate with lower gain voltage. At 300 mA the maximum gain voltage which can be used without damaging the PMT is 0.9 V.

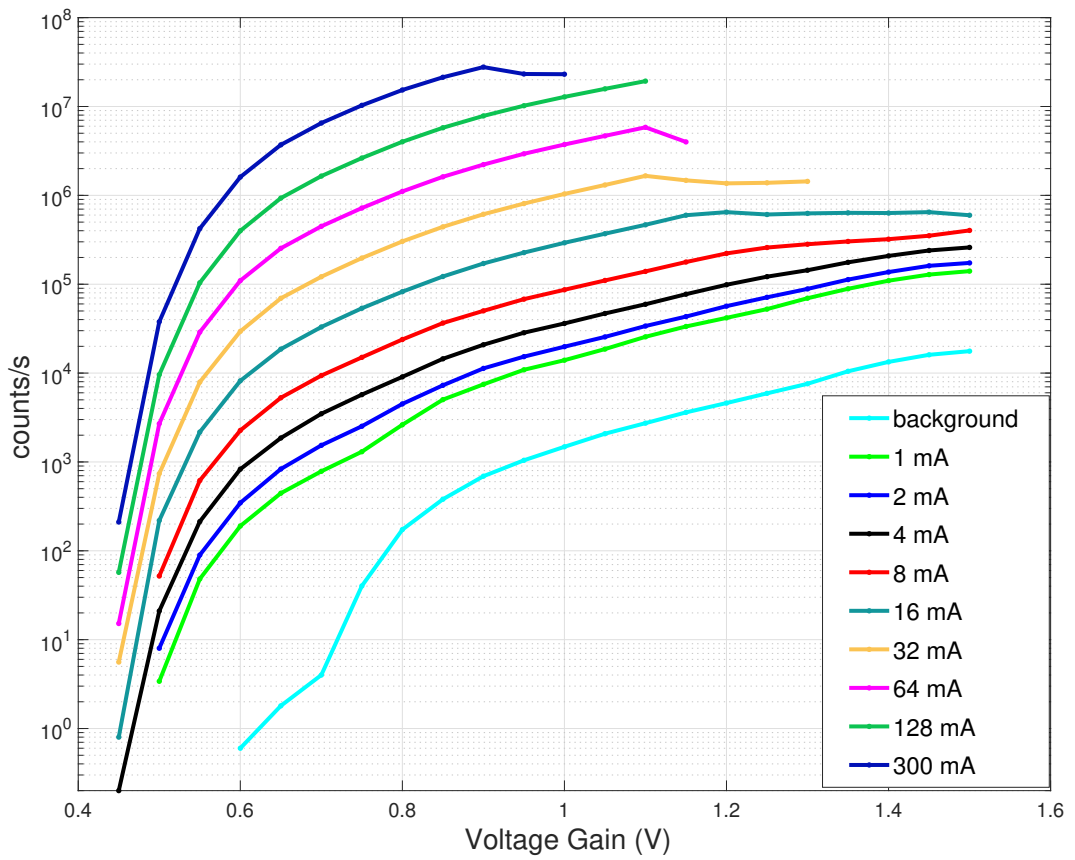


Figure 3.16: The count rate for different voltage gains in the PMT as the beam current increases.

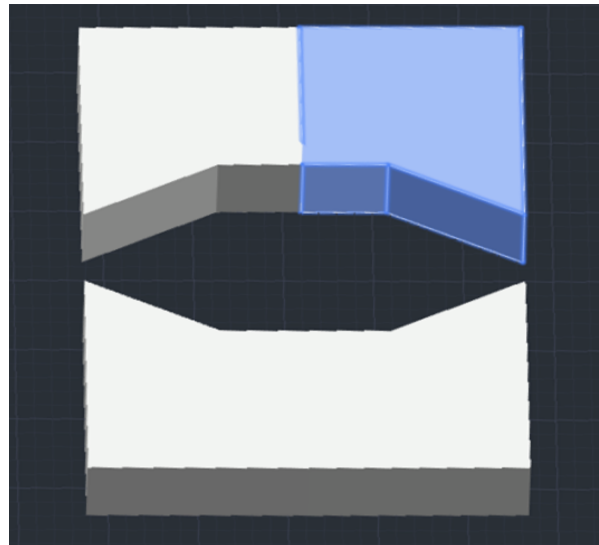


Figure 3.17: The transverse view of the custom-design of the scintillator detectors. Four blocks, identical to the blue one, are designed in order to fit and be placed around the octagonal beam pipe.

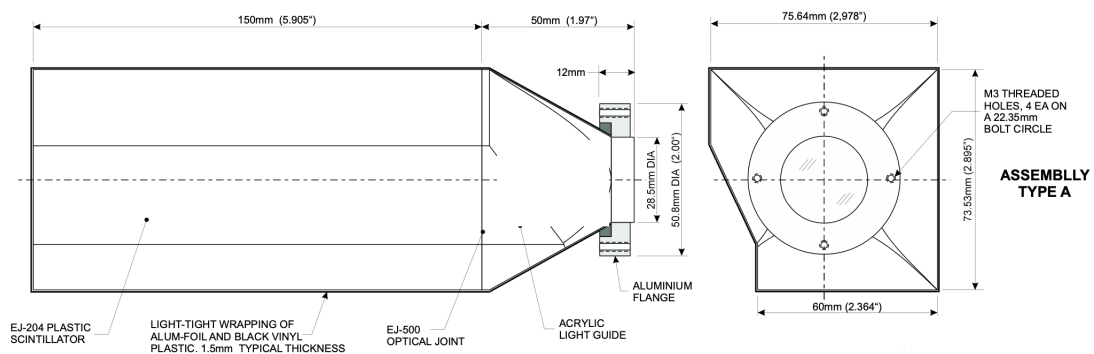


Figure 3.18: The mechanical drawing of one of the custom-made blocks of the detector.

3.2.10 Detector design

Based on the radiochromic film measurements results, four scintillators were designed to fit around the octagonal shape of the beam pipe. Thus, they can capture a high fraction of the electromagnetic shower created when an electron is lost. The 3D design of the custom-built detector was modelled in AutoCAD [103]. Fig. 3.17 shows the transverse view of the detector, which consists of four identical blocks to the one highlighted in blue. The detector was manufactured by Eljen Technology [98].

Since the scintillator's size increases the probability of the charged particles interacting with the material, the detector blocks are as long as possible by the physical limitations. Thus, the length of the scintillator block is 15 cm. The scintillator block is then attached

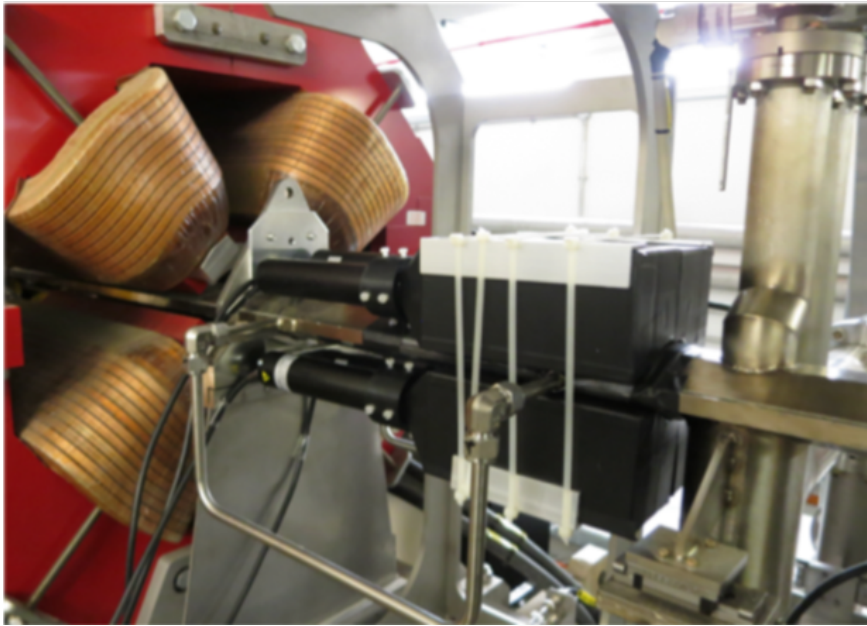


Figure 3.19: The four beam loss detectors installed around the beam pipe.

to an acrylic light guide that is used to transfer the light to the photocathode's circular surface, as shown in the mechanical drawing in Fig. 3.18. Both scintillators and light guides are coated with aluminium foil to prevent light leaks and further with black vinyl plastic to prevent the outside light from interfering with the detectors' light.

The four blocks were equipped with a photomultiplier with a bialkali photocathode that matches the wavelength of the scintillator light. Thin silicone pads were placed between the photocathode and the light guide's ending to avoid any reflections when the light passes through the two different materials. In the end, aluminium flanges were mounted at the end of the light guide to assist the PMT attaching to the detector. The monitors are wrapped with a thin sheet of lead 1.3mm thick and protected from the background ionizing radiation. A picture of the detector installed in the storage ring is shown in Fig. 3.19.

3.3 Acquisition system

The detectors are connected with the Libera BLM data acquisition instrument (Instrumentation Technologies Libera BLM) [104], which uses two hardware interfaces. Four coaxial connectors are used for signal input and four RJ-25 connectors for supplying power and voltage gain control, as shown in Fig. 3.20.



Figure 3.20: Picture of the data acquisition electronics module.

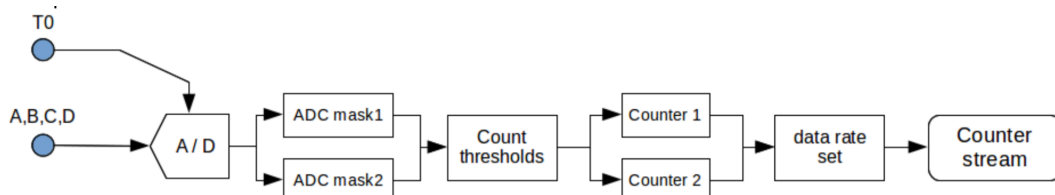


Figure 3.21: Diagram of the counting system.

The instrument is set with an impedance input of $50\ \Omega$ for short individual pulses. The amplitudes are recorded with a 14-bit resolution. The input signals are sampled using an analogue to digital converter (ADC) with a clock rate which is locked to a quarter of the rf frequency, a little below 125 MHz. The reference signal is the revolution clock and is provided through a T_0 connector on the instrument's back panel.

3.3.1 Counting mode

The signal from the beam loss detectors is processed by the data acquisition Libera system using the counting mode. The diagram of the counting system is shown in Fig. 3.21. The ADC converter is locked to a reference clock which is the revolution frequency of the storage ring T_0 . The T_0 revolution clock defines the processing window length (t_0 interval), which is the number of ADC clock cycles between two T_0 events. For the case of DLS, where the revolution frequency T_0 is set to 533 kHz, the processing window length t_0 corresponds to 234 ADC clock cycles samples.

Within the processing window, an ADC mask is used to select only a part of the window. The ADC mask is configured with an offset (starting point of the processing window) and a mask window (length in ADC cycle samples). The offset and window parameters are configured with reference to the T_0 event. It is possible to set two independent ADC masks over the same t_0 interval. Fig. 3.22 demonstrates the ADC mask offset and mask and the two masks that can be set. The lines are spaced at the ADC sampling rate and

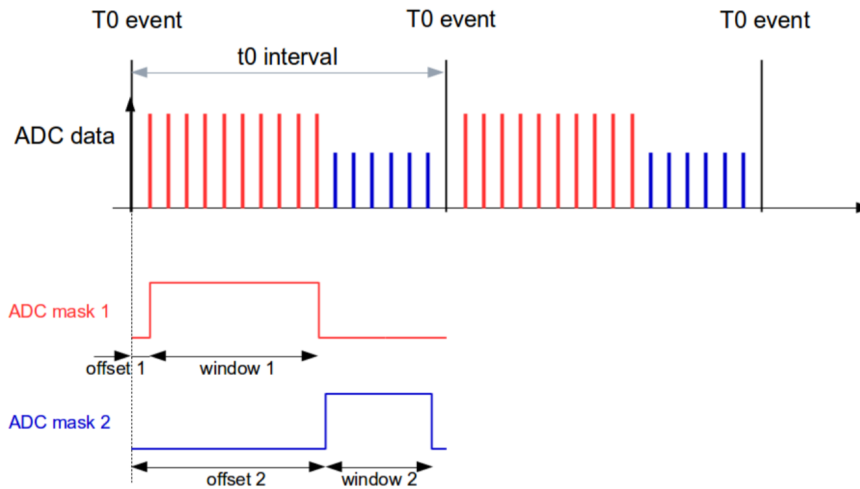


Figure 3.22: The principle of ADC masks.

correspond to the ADC clock samples per revolution.

The ADC data from the two ADC masks are then provided to a stream branch (counter 1 and counter 2), where the counting logic is applied. When an ADC sample drops below a threshold limit that the user sets, this is considered as pulse and the counter increments by one. The ADC sample must rise above the threshold before a pulse can be detected. The threshold counter value is set to 1% of the 14-bit resolution ADC amplitude to avoid false triggers from electronic noise. The counter data rate can be set between 1 and 10 Hz. Then, the sampled counter data are provided to the counter stream.

This system's advantage is that the setting of two independent ADC masks over the same t_0 interval yields two counter values. Thus, the user can analyse losses only on a selected part of the fill pattern in the storage ring. When both masks are configured, losses can be acquired from two parts of the fill pattern, and data can be analysed independently.

3.3.1.1 Pile-Up pulses

In the presence of a pile-up effect in the scintillator detector, some pulses are created during the decaying time of the previous pulse, causing a distortion of the measured pulse. If two pulses are very close in time, the system will record the two pulses as a single event and reduce the counting efficiency. An example is shown in Fig. 3.23. The dark green solid line represents a sequence of ADC samples where three pulses are very close in time. The three pulses are under the red line, which represents the threshold limit for the counting

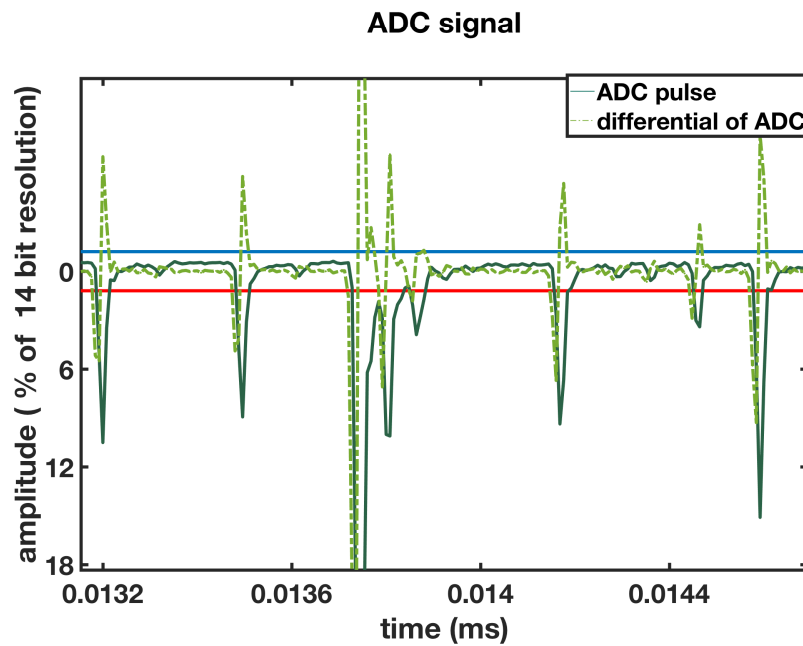


Figure 3.23: The counting of pulses with the two different methods.

algorithm explained earlier. This results in the counting of one pulse instead of three.

For this reason, a new algorithm was introduced to detect and count the pulses based on the difference between the two neighbour samples. The counter will increment when the current sample's amplitude is lower than the previous sample's amplitude or, in other words, when the differential of the two samples amplitude is higher than a threshold set by the user. In Fig. 3.23 the dashed line is the differential of the ADC samples, and the blue line is the new threshold. The improvement due to the differential counting mode is shown for the pile-up event as this algorithm can separate the three events and count three pulses instead of one. This approach has shown better performance in pulse counting than the previous method and has been used for future studies.

3.3.1.2 Coincidence

Losses detected by the counting algorithm can be correlated between the four channels. There are four different coincidence counters for the four channels. A detection window starts after a selected channel (master channel) reports the loss event. If other channels within the detection window report the loss events, a coincidence count for the selected channel will increment by one.

The coincidence counting was suggested for the detection of Touschek particles. In princi-

ple, since the two colliding particles lose and gain an equal amount of momentum, they will hit the inside, and the outside wall of the vacuum chamber [36]. This technique did not work to detect the depolarisation resonance with the detectors of this study due to their location. As they are placed after the collimators, the electromagnetic showers created by each lost particle are overlapping. This does not allow the coincidence counting to detect the shower created by two different particles. The coincidence counting was tested in other locations, where the dispersion is high. However, this did not allow the detection of the depolarisation resonance, as the counting rate was very low, and as Poisson statistics dictates, the noise level high.

3.3.2 Libera software

The core of the instrument is the Xilinx Zynq [105], a dual-core ARM CPU integrated with a Zynq FPGA and several communication controllers on the same chip. The Libera software is based on the design shown in Fig. 3.24. The Linux Kernel Module communicates with a Field-programmable gate array (FPGA). An application daemon runs continuously and handles periodic service requests that the FPGA expects to receive. A Media Control Interface (MCI), which is a high-level Application Programming Interface (API), is used to define interactions between multiple software intermediaries. More specifically, it uses a registry and a signal library underneath for accessing application properties, acquiring signals and changing the application behaviour. On top of MCI, adapters to various control systems, like the EPICS control system, or the command-line tool Libera ireg, are implemented to provide information about the Libera BLM status and configuration. At the same time, enables the change of the configuration parameters and to access the acquired data.

3.4 Excitation

3.4.1 Excitation hardware

The excitation of the beam for the energy measurements is implemented by the Transverse Multi-Bunch Feedback (TMBF) system [106], [107]. The TMBF system is used to control multi-bunch instabilities and to measure the betatron tunes. Because of the bunch by bunch selectable control over feedback filters, gain and excitation, a group of bunches in

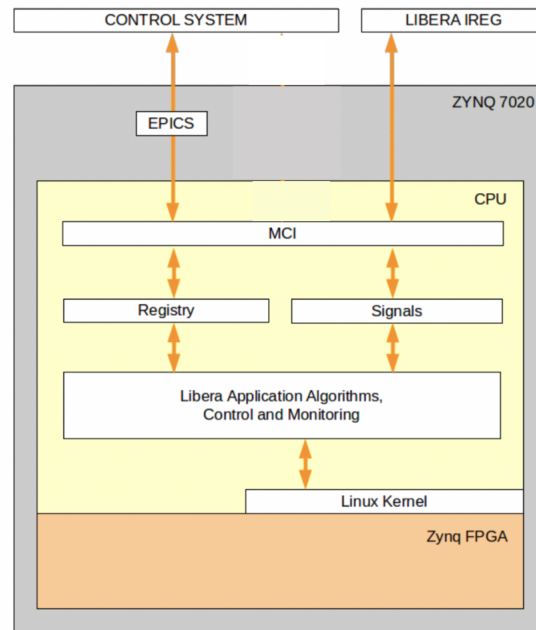


Figure 3.24: Libera software structure (courtesy of Intrumentation Technologies [104]).

the fill pattern can be controlled independently from the bunch train. This characteristic allows experimental studies like continuous measurement of the beta-function, grow-damp measurements in unstable conditions and programmed bunch cleaning. Also, it is essential for the implementation of the energy measurements during user time, where only a selected part of the beam is excited, and the other is unaffected.

For the case of the energy measurements, a numerically controlled oscillator (NCO) integrated into the TMBF system creates a sinusoidal signal at frequencies close to 450 kHz. The signal can be modulated with an internally synchronised rectangular waveform with frequency 533 kHz and duty cycle, which is varied between 40% and 50%. The DAC output is amplified using a 2.8 GHz Differential Amplifier (LMH6554) [108]. Later it is split in two opposite directions by a 180° hybrid coupler (H5675) [109] as shown in Fig. 3.25. The split currents flow through the feedthroughs 1 and 2 in Fig. 3.26 and feed the two parallel to each other 30 cm long kicker striplines, producing horizontal oscillating magnetic fields. The feedthroughs 3 and 4 are connected to resistive loads. The magnetic fields that are generated in the same direction add up and excite the beam. The maximum integrated magnetic field that can be produced is 8 Tm.

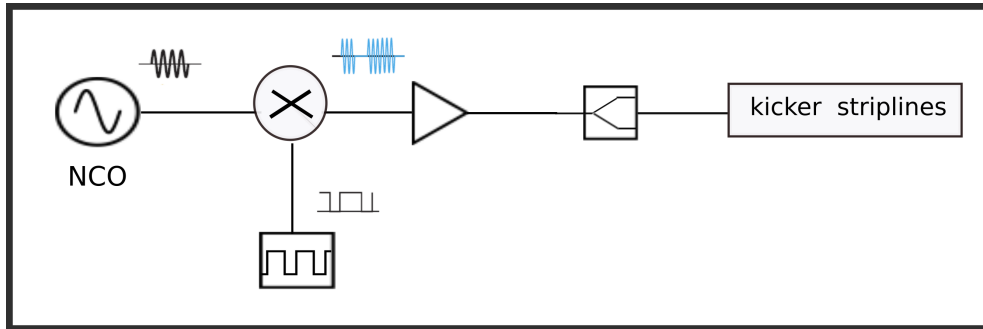


Figure 3.25: Schematic of the generation of the excitation signal by the TMBF system. The symbol \odot represents the signal generator in the NCO. The rectangular waveform used for the modulation is indicated by the symbol \square . The symbol \otimes represents the modulation of the signal. The amplifier is depicted by \triangle . In the end the symbol \square stands for the hybrid coupler.

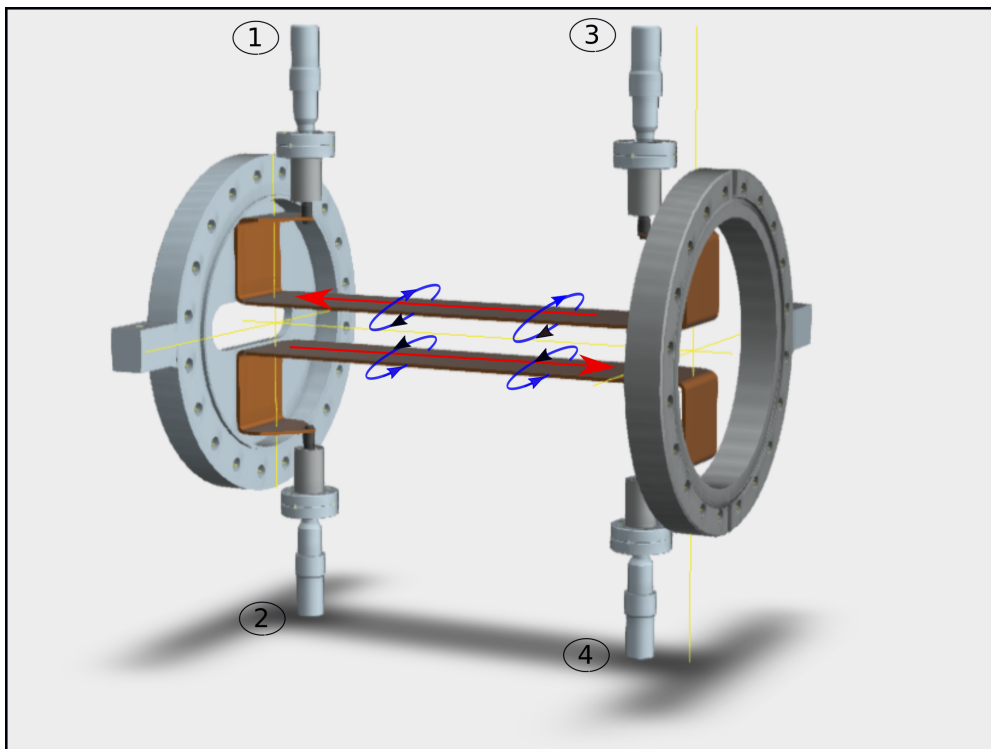


Figure 3.26: 3D design of the striplines used for beam excitation. The current and the magnetic fields generated by the striplines are indicated by the red arrow and the blue loops accordingly.

3.4.2 Excitation principle for energy measurements

The excitation principle for the energy measurements is based on selecting one part of the beam, while the rest is unaffected. Figure Fig. 3.27 describes the implementation of this concept. In the first subplot *a*, the fill pattern of the machine is shown, which consists of 900 occupied and 36 empty buckets. For this case, the first 300 bunches of the fill pattern were selected to be excited. The carrier signal, which is a sinusoidal signal with a frequency in accordance with the spin tune (450 kHz) and is generated by the NCO of the TMBF system, is shown in subplot *c*. The message signal, which is a rectangular signal with a period which equals the revolution time (533 kHz) and is used to modulate the carrier signal, is illustrated in subplot *b*. In the end, the modulated signal in subplot *d* can excite only the selected bunches of the fill pattern, leaving the others unaffected. The part of the excited beam can be set by changing the duty cycle of the rectangular message signal. This feature is essential for implementing the online energy measurements, where the losses from the excited and the non-excited part of the beam are detected by the two ADC masks separately and are used to detect the depolarisation event, excluding the background data from external factors.

3.4.3 Amplifier problem

An amplifier is used to amplify the TMBF system's signal before the stage of feeding the striplines. A typical signal in the time domain is shown in Fig. 3.28a. This modulated signal is a product of a sinusoidal signal with a rectangular wave signal. In Fig. 3.28b, the discrete Fast Fourier Transform (FFT) of the designed modulated signal is shown. If the frequencies of this signal used as inputs in the amplifier are not in the amplifier bandwidth range, a distorted signal is created. The modulated signal harmonics that have frequencies lower than the cutoff frequency of the amplifier are removed. A simulation of the effect of a high pass filter completely suppressing the lowest frequency of the signal ($0.16 f/f_{rev}$) is shown in Fig. 3.28b. The inverse FFT of this signal, when the low-frequency harmonic is suppressed, is shown in Fig. 3.28c. The outcome in the time domain is a problematic signal. The parts of the signal, designed to have zero amplitude, follow a sinusoidal signal with a frequency equal to the one suppressed by the amplifier. Thus, the part of the beam designed to be unaffected is excited with a lower frequency signal. When this frequency matches the mirror frequency of the spin frequency ($1 - 0.84$), like this simulation case,

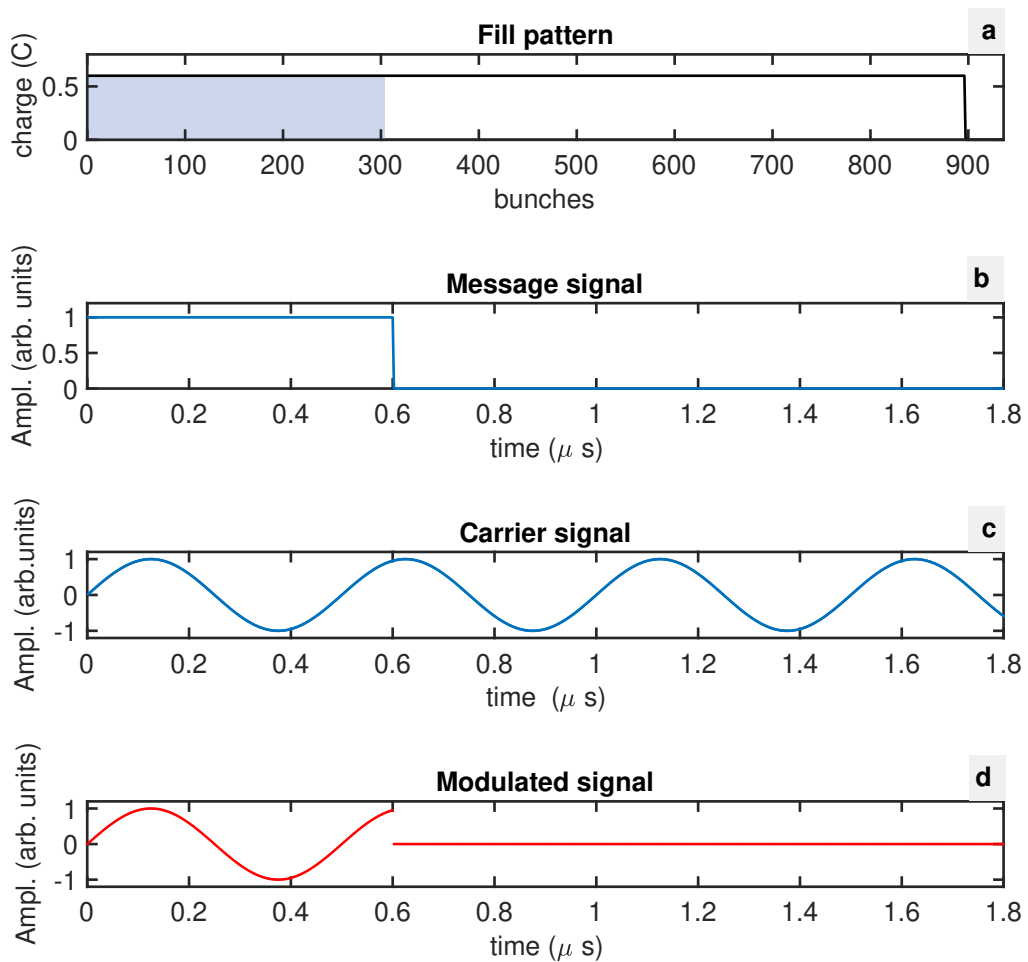


Figure 3.27: The principle of excitation of half part of the beam, while the rest of the bunches are unaffected. Subplot *a* depicts the fill pattern in the storage ring. The first 300 bunches that are excited are coloured gray. Subplot *b* and *c* show the message and the carrier signal respectively. The modulated signal, used for the excitation of the beam is shown in subplot *d*.

the beam can get depolarised.

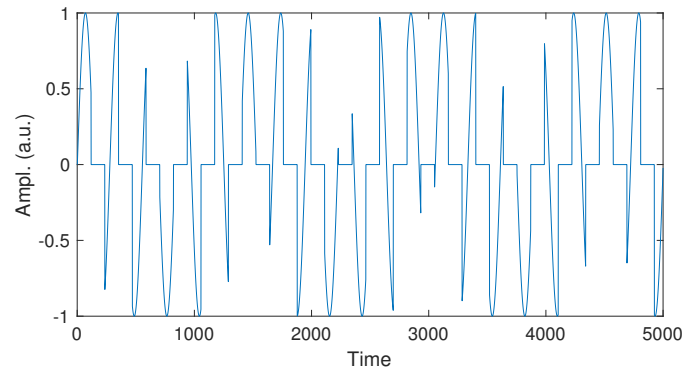
This is a significant problem of the excitation scheme, which cancels the online energy measurements' main idea. Because both parts of the beam are depolarised with unequal strength, the ratio between the count rate of the beam loss monitor masks shows a slight beam loss increase of 0.2% in a depolarisation event. This increase was low and did not match the expected beam loss increase according to the calculations, even if the excitation strength was high. The problem was resolved by exciting the beam with a higher frequency signal. This frequency matches the spin tune which has the same non-integer part but higher integer part. In this way, the higher harmonics frequencies of the modulated signal fit in the amplifier's bandwidth, and the output signal is not distorted.

3.5 Synchronisation

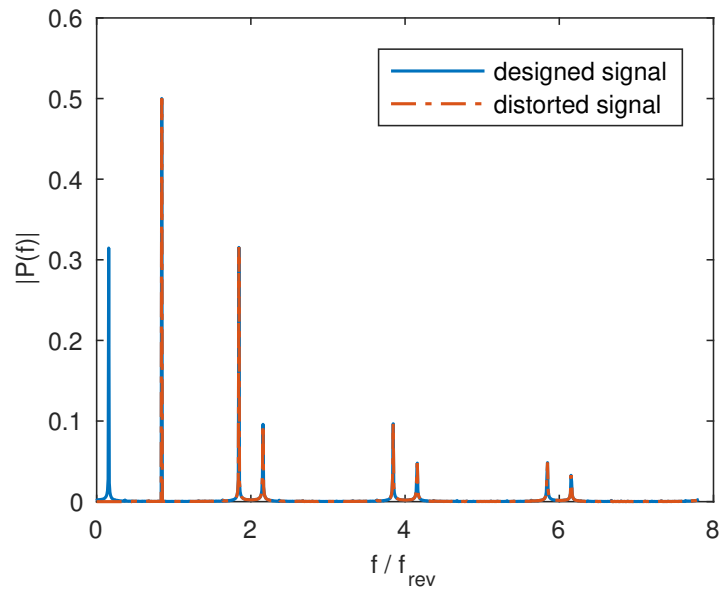
All the components of the accelerator are synchronised by utilising a timing system [110]. For this study, the main components that should be synchronised are the TMBF system which produces the excitation of the selected bunches and the beam loss system, which should detect the losses produced only by the excited bunches. The event clock is derived from the 500 MHz master oscillator and is distributed to the TMBF system, the Low-Level RF system and the event generator, as shown in Fig.3.29. The event generator (EVG) generates the revolution clock and other events and distributes them over fibre optic links to multiple event receivers (EVR). The EVRs decode the revolution clock and distribute it as a TLL signal to the beam loss monitor system.

The TMBF system calculates internally the revolution clock when it receives the event clock. This means that the revolution clock of the TMBF system and the beam loss monitors are generated by different systems and results in two revolution clock signals with the same frequency but with a phase difference.

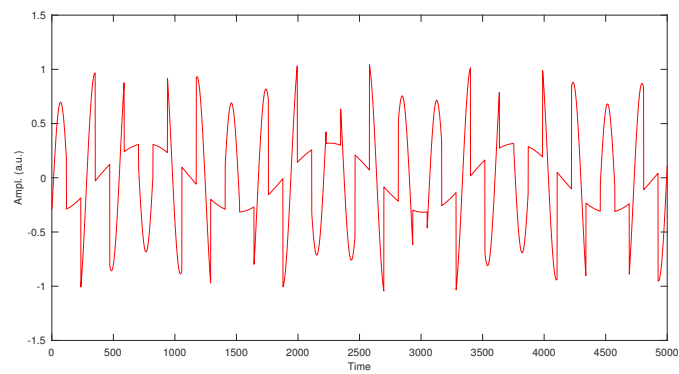
Since the two systems have a phase difference, the ADC cycle sample sequence will be shifted in relation to the bucket sequence. Thus, the number assigned to each bunch will be different in the two different systems. An example is illustrated in Fig. 3.30 where the blue colour shows the part of the fill pattern that consists of 936 buckets (900 are occupied and 36 are empty). The two x-axes in Fig. 3.30 illustrate the number assignment in the ADC cycle samples on the top and the TMBF system on the bottom. The first bunch of



(a) The designed modulated signal.



(b) Single sided discrete Fourier transform of the signal.



(c) Distorted modulated signal.

Figure 3.28: Graphical explanation of the distorted amplifier's output signal due to the bandwidth of the amplifier.

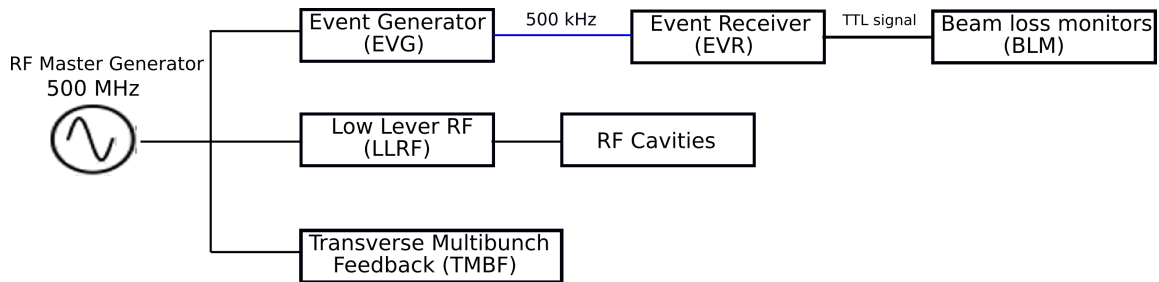


Figure 3.29: The timing system for the synchronisation of TMBF system and the beam loss monitor system. The blue line represents the fiber optic connections.

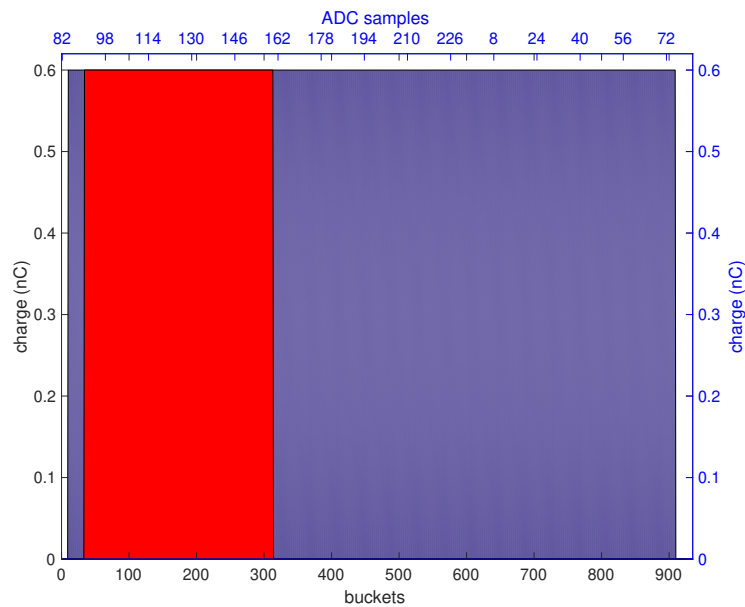


Figure 3.30: The different reference of the bunches in the fill pattern and the beam loss monitor system is shown in the two x -axes. The first bunch in the fill pattern is represented by the 82nd ADC cycle sample in the beam loss monitor system. The total fill pattern in the blue colour consists of 900 bunches. The excited 280 bunches are shown in the red colour.

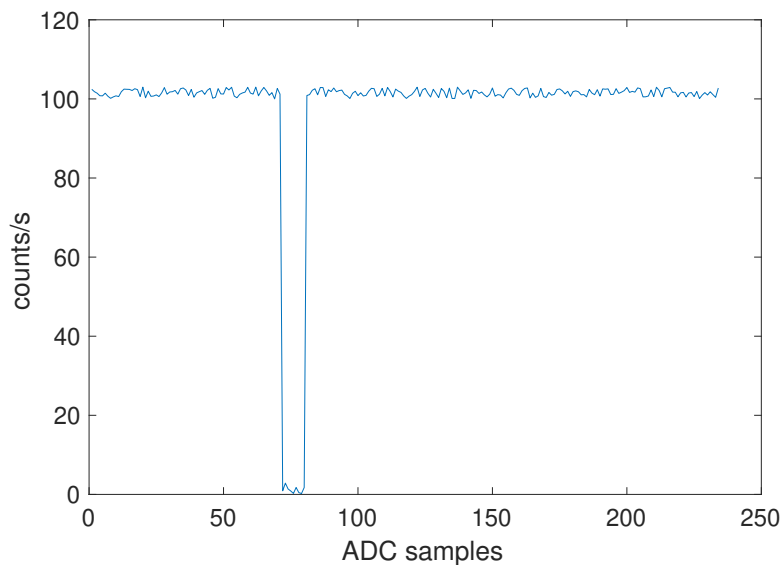


Figure 3.31: Each ADC cycle sample correspond to four buckets in the fill pattern. The beam loss rate for different ADC cycle samples

the fill pattern corresponds to the 9th bucket of the fill pattern, and the losses are detected by the 90th ADC cycle sample in the beam loss monitor acquisition system.

When one part of the beam is set to be excited (in red colour in Fig. 3.30), a technique to align the TMBF system and the beam loss monitors has to be employed. The beam losses detected by an ADC mask follow the same pattern as the fill pattern. When the buckets are filled, the beam loss monitors detect the losses that come from the corresponding bunches. When the buckets are empty, the count rate is zero. Using the feature of changing the length of the ADC mask window and the offset (explained in subsection 3.3.1), the window of one mask of the beam loss system is set to be as short as possible (one ADC cycle sample corresponds to beam losses produced by four buckets) and the offset increments by one. In this way, the beam losses from different parts of the fill pattern are scanned. The acquired data is plotted versus the number of the ADC cycle samples, as shown in Fig. 3.31 and is compared with the fill pattern in Fig. 3.27a. From this comparison, the ADC cycle sample that precedes the gap and corresponds to the first bunch of the fill pattern can be detected and will be the reference to the alignment between the two systems.

3.6 Summary

A detailed study was conducted to find the best material for the detectors of the beam loss monitors. For the detection of Touschek particles, the detectors were installed downstream of the collimators, where there is the highest ratio of physical aperture and dispersion. The radiochromic film measurements demonstrated the area around the beam pipe where the highest fraction of the electromagnetic shower, created by the lost particles, is deposited. Four detectors were installed around the beam pipe and cover this area to maximise the count rate of the beam losses. The main characteristics of the acquisition system for our studies were described. The improvement of the acquisition system led to the optimisation of pulses detection. Additionally, the feature of the ADC masks introduced in the system is important for the working principle of the energy measurements during user time. Lastly, the excitation scheme using the kicker striplines and the amplifier problem with its solution was described, and the synchronisation of all the systems was presented.

Results and discussion

This chapter will discuss the results regarding the beam polarisation that can be achieved in the storage ring of Diamond Light Source. The energy measurements using resonant spin depolarisation accompanied by complementary studies will be demonstrated. The challenges of the continuous energy measurements and our approach to resolving them are presented. In conclusion, the main aim of this study, the continuous energy measurements during user operation mode are shown.

4.1 Beam polarisation

A sufficient level of beam polarisation is essential for the implementation of the resonant spin depolarisation technique. The maximum beam polarisation that can be achieved in an ideal machine without the effect of magnetic field errors is 92 % [43]. However, in the real case scenario, the beam polarisation does not reach this value. For the case of the storage ring of DLS, the maximum level of the beam polarisation was measured.

4.1.1 Beam loss and lifetime data

The beam polarisation that can be achieved in the DLS storage ring was obtained from the data provided by the beam loss monitors and the beam lifetime data that can be derived by fitting the slope on the measurement of beam current taken by a parametric current transformer (DCCT). Fig. 4.1 shows the data from beam loss monitors and DCCT monitors, after the injection of 900 bunches corresponding to 300 mA beam current in the

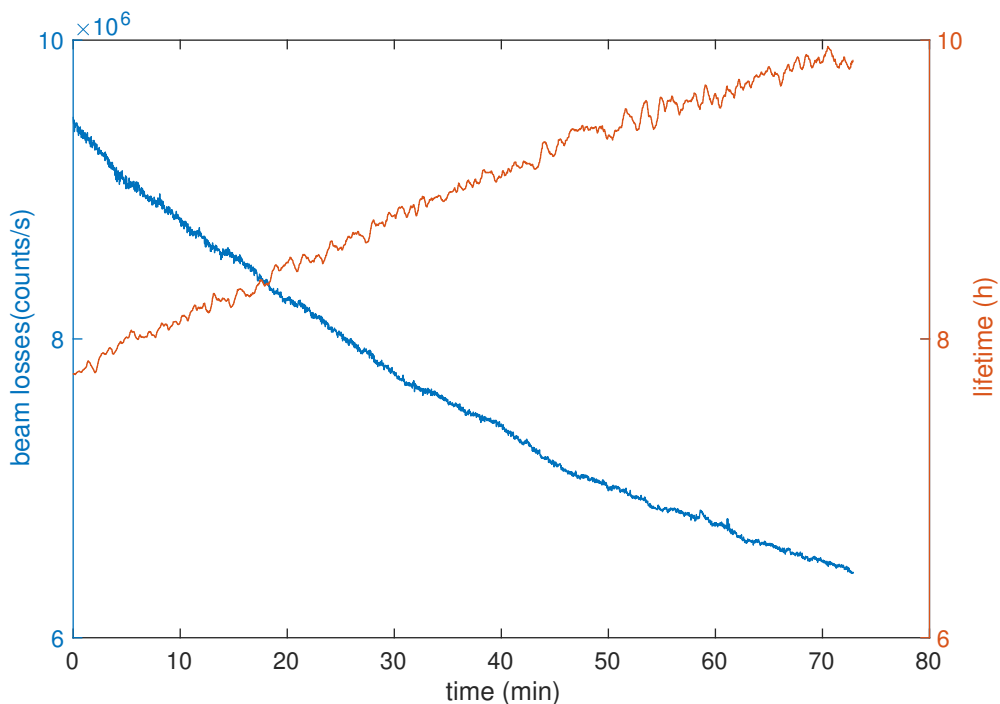


Figure 4.1: The beam losses and the lifetime versus time in minutes during the polarisation process.

storage ring. The beam losses with these settings in the machine are considered to be dominated by Touschek scattering. Data were acquired for 70 mins while the beam was left to decay without any top-up injections, and wigglers were turned off.

Due to the decay of the beam current and the build-up of beam polarisation, the beam losses decrease with time while the lifetime increases. To account for the effect of the beam current decay and show only the effect of the polarisation build-up, the beam loss data and the lifetime are normalised to the beam current according to:

$$\frac{1}{I(t)^2} \frac{dN}{dt} \propto C(\varepsilon) + F(\varepsilon)P(t)^2 \quad \frac{I(t)}{\tau} \propto C(\varepsilon) + F(\varepsilon)P(t)^2 \quad (4.1)$$

These relationships are based on the equation 2.19 where the bunch population for a given time $N(t)$ is replaced by the beam current, assuming that all the bunches of the stored beam have equal current. The functions $F(\varepsilon)$, $C(\varepsilon)$ can be treated for a given measurement as constants [38]. The beam loss data is divided by the square of the beam current data, and the lifetime data is multiplied by the beam current data according to Eq. 4.1. The normalised data is shown in Fig. 4.2. The increase and the decrease of the lifetime and beam losses respectively is equal to 10%. The last ten minutes in both data sets show a

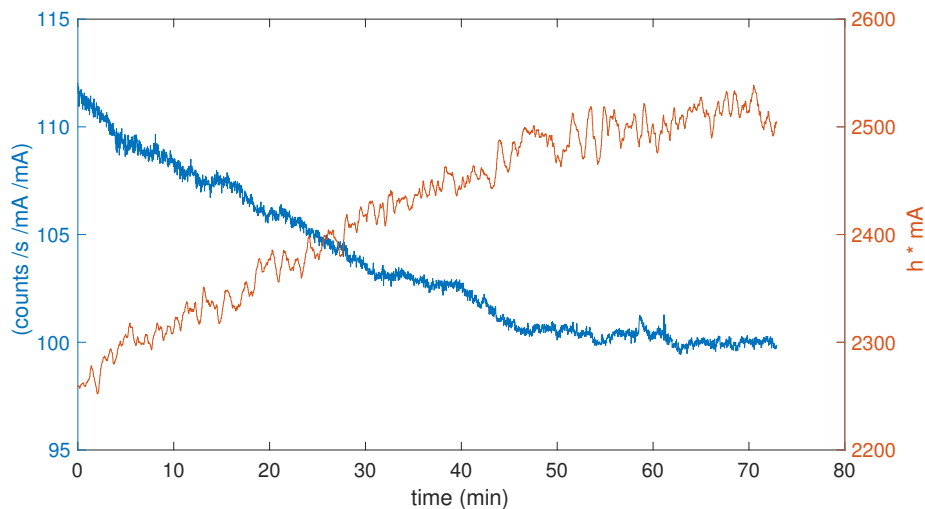


Figure 4.2: The beam losses and the lifetime normalised to the beam current versus time during the polarisation process.

plateau, indicating that the maximum level of polarisation has achieved.

4.1.2 Calculation of the beam polarisation

The relationship between the increase of the lifetime and the polarisation (P) is given by the following equation [15]:

$$\frac{\tau_{(0)}}{\tau_{(s)}} = 1 + \frac{F(\varepsilon)}{C(\varepsilon)} P^2 \quad (4.2)$$

where, $\tau_{(0)}$ corresponds to the initial lifetime after the injection, when the beam polarisation equals to 0, and $\tau_{(s)}$ is the lifetime value at any given time after the injection, when the polarisation starts to build-up.

The variables $F(\varepsilon)$ and $C(\varepsilon)$ can be calculated according to equations 2.21, 2.22. The beta function, the momentum acceptance, the beam energy and the horizontal emittance were used for this calculation. The mean value of the variables $C(\varepsilon)$, $F(\varepsilon)$ are used as constants for the beam polarisation calculations.

The polarisation can be calculated by using the beam lifetime or the beam losses data based on equation 4.2. The polarisation expressed as $P = \sqrt{\left(\frac{\tau_0}{\tau_s} - 1\right) \frac{C(\varepsilon)}{F(\varepsilon)}}$ is plotted versus time in Fig.4.3. The beam lifetime can be derived by fitting a slope to the beam current measurement from the parametric current transformer. Alternatively, a value corresponding to the beam lifetime can be calculated from the measurement of beam losses using Eq. 1.11 with the approximation that the bunch electron population $N(t)$ is

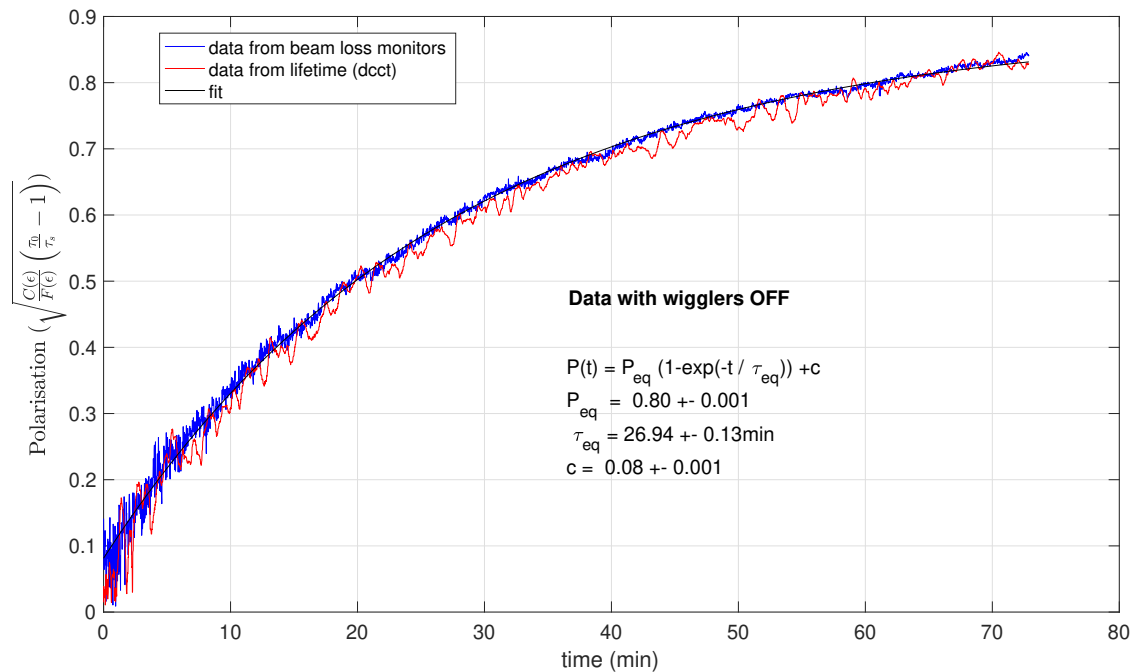


Figure 4.3: Polarisation build-up using beam loss data and lifetime data.

proportional to the beam current $I(t)$.

The amount of polarisation will be a combination of the polarising and depolarising effects and is given by [40] :

$$P(t) = P_{ST} \frac{\tau_d}{\tau_d + \tau_{ST}} \left[1 - \exp \left(-\frac{t}{\tau_{ST}} \left(\frac{\tau_d + \tau_{ST}}{\tau_d} \right) \right) \right] \quad (4.3)$$

where P_{ST} and τ_{ST} are the Sokolov-Ternov values for the equilibrium polarisation level and the time constant, respectively, and τ_d is the depolarisation time constant. Using formula 4.3, we can have an estimation of the polarisation level during the polarisation process.

A fit according to equation 4.3 is applied to calculate the maximum equilibrium polarisation level that can be achieved and the corresponding polarisation time. An offset c is introduced to include the polarisation that had already built-up at the beginning of the data acquisition and should be added in the fitted variable P_{eq} to calculate the total equilibrium polarisation level.

Because of the excellent alignment given by the orbit correction schemes of DLS, the closed orbit distortion are not strong to reduce the equilibrium beam polarisation, allowing the

Insertion Device	Length (m)	Peak Field (T)
Wiggler I15	1.35	3.5
Wiggler I12	1.12	4.2

Table 4.1: Characteristics of the two insertion devices.

beam to acquire a polarisation level of 88%.

4.1.2.1 Effect of wigglers on polarisation

The equilibrium polarisation level P_{ST} is related with the integral of the magnetic fields B along the curvilinear trajectory of the beam s [38], [111], [112]:

$$P_{ST} = \frac{8}{5\sqrt{3}} \frac{\oint B^3 ds}{\oint |B|^3 ds} = \frac{8}{5\sqrt{3}} \frac{\oint \rho^{-3} ds}{\oint |\rho|^{-3} ds} \quad (4.4)$$

where ρ is the bending radius of a homogeneous magnetic field. The contribution of the wiggler insertion devices in the denominator is given by:

$$\oint |\rho|^{-3} ds = \frac{4L_w}{3\pi\rho_w^3} \quad (4.5)$$

where $\rho_w = \frac{B_w}{B\rho}$ is the bending radius in the wiggler and is equal with the ratio of the magnetic field in the wiggler to the magnetic rigidity. L_w is the length of the wiggler unit.

When wiggler insertion devices are introduced, the polarisation level is reduced. At the DLS, there are two electrically powered wiggler insertion devices with the characteristics shown in 4.1. Undulators are not considered in this calculation as their magnetic fields are weak enough to reduce the beam polarisation level.

Using this information, the equation 4.5 for the case of DLS with the two wiggler insertion devices reveals that the maximum polarisation that can be achieved is 63%. This calculation was compared with the experimental data.

Data were taken with the two wigglers turned on and were used to measure the polarisation level. As shown in Fig. 4.4 the polarisation that can be achieved calculated by the experimental data fit is 65%. The experimental data is in good agreement with the theoretical calculation.

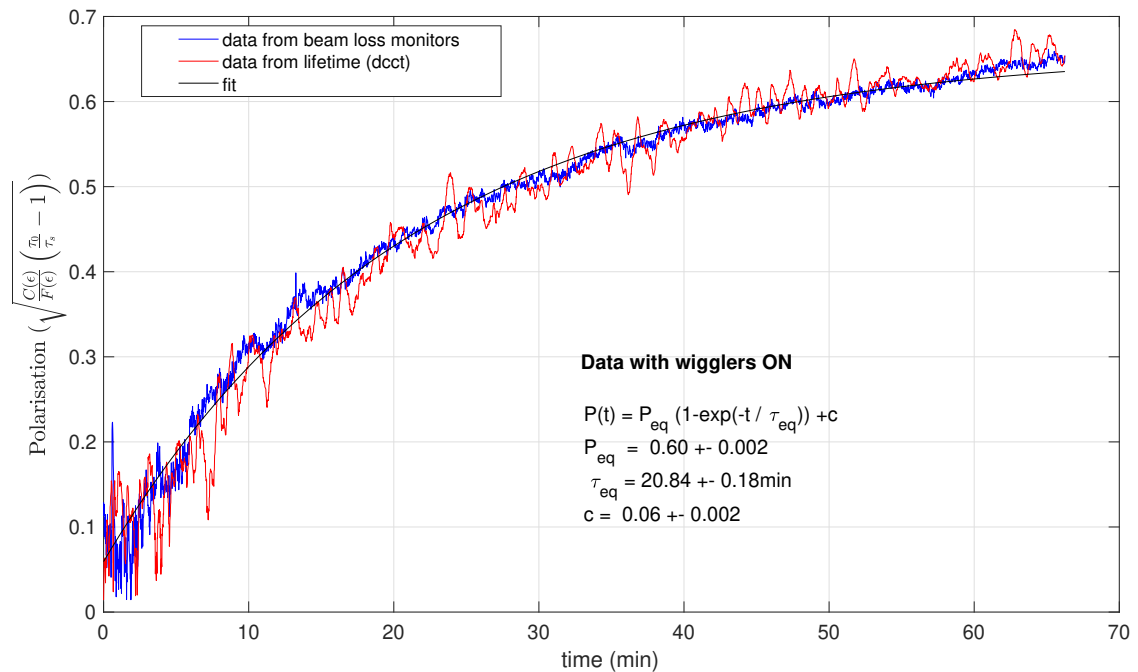


Figure 4.4: Polarisation build-up with wigglers turned on.

4.2 Beam depolarisation measurement

The resonant spin depolarisation of the beam was demonstrated, and different complementary measurements were conducted to understand the results and verify the theoretical approach.

4.2.1 Resonant Spin Depolarisation scan

The basic working principle of the resonant spin depolarisation is: the beam is excited by a horizontal magnetic field produced using a set of vertical stripline kickers. The magnetic field is set to oscillate at a frequency f_{dep} , which matches the fractional part of the spin tune. When the vertical excitation frequency resonates with the spin tune, the spin-vector is tilted away from the vertical axis by a small amount in successive revolutions of the storage ring, gradually reducing the beam polarisation. The particle loss rate increases, when the beam polarisation decreases. This is due to the spin-dependent Touschek scattering cross-section according to Eq. 2.19. An example of a depolarisation scan is shown in Fig. 4.5. The loss rate normalised by the square of the beam current is plotted against the frequency that the beam is excited with. Thus, given the assumption that beam losses

do not originate from other reasons than the beam decay and the beam depolarisation, the increase of the beam losses indicates the spin precession frequency and consequently the beam energy.

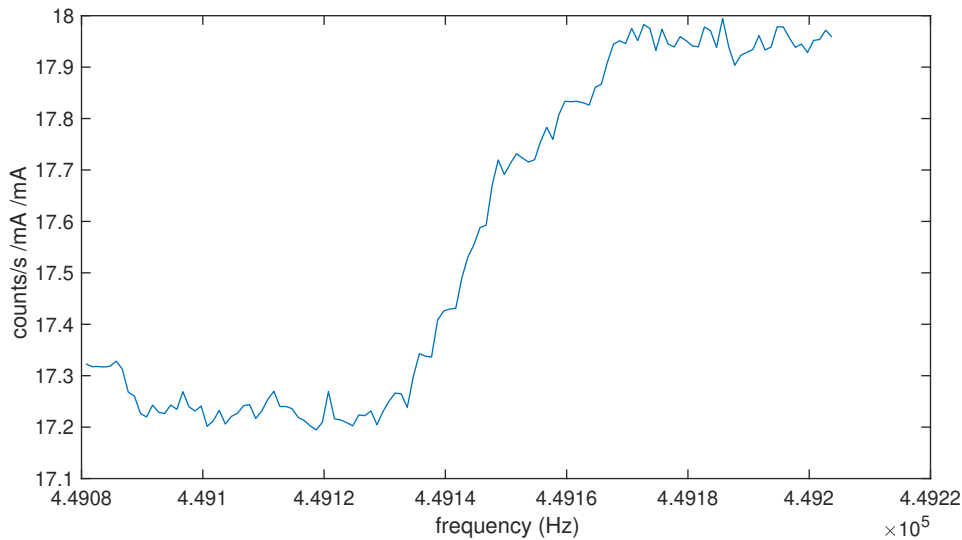


Figure 4.5: Resonant spin depolarisation scan.

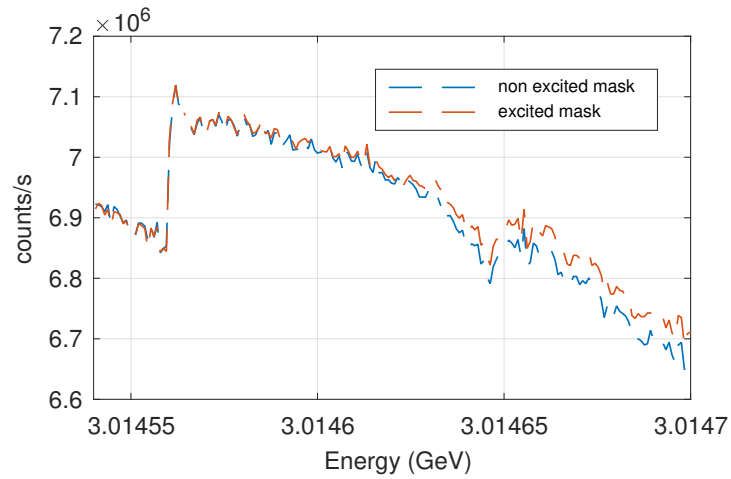
4.2.2 Touschek particle detection in high dispersion areas

According to other studies related to the detection of the Touschek particles, it was suggested that the best location for their detection is a high dispersion section following sections where a high particle density is reached [95], [36], [25]. Following this recommendation, a set of beam loss monitors was placed in a high dispersion position in the accelerator, one outside the ring chamber and another inside. However, because the physical aperture was not as small as the one after the collimators, the loss rate during the depolarisation scans did not indicate depolarisation during most of our attempts. In contrast, the depolarisation event was evident by the loss rate in the location after the collimators.

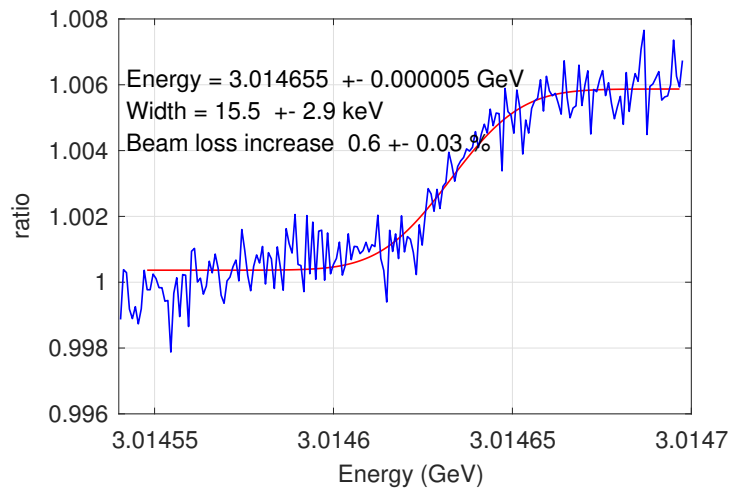
The coincidence counting of the beam losses during depolarisation was studied as well. The coincidence counting was implemented in the acquisition system, and data were recorded from the beam loss monitors in both locations during depolarisation scans. None of the energy measurements scans showed an increase in the detected loss rate due to depolarisation.

4.2.3 New approach of the depolarisation scan

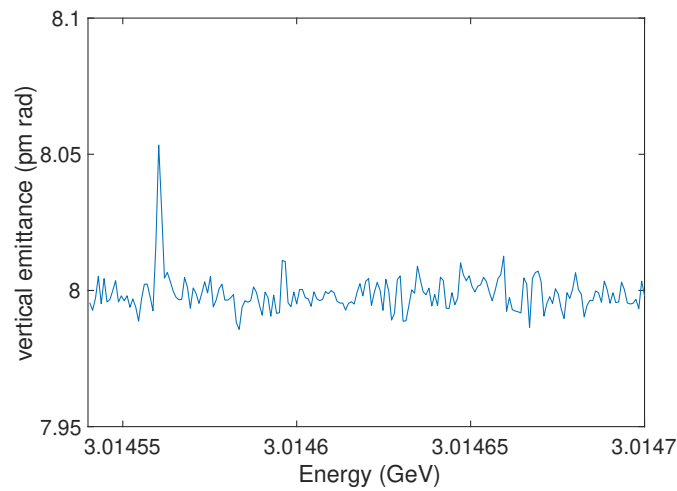
One of the main challenges of the energy measurements is the background beam losses created by causes different from depolarisation during user time. The idea of gating the excitation pattern and the beam loss detection was introduced as described in Section 3.3.1 to overcome this problem. The TMBF system has the capability to select and excite only the bunches that are of interest. The implementation of this capability is described in Section 3.4. The beam loss data acquisition system is equipped with two ADC masks that can monitor only a selected part of the beam. The main principle of the continuous measurements is to excite one part of the beam and count the beam losses using one ADC mask that is time-aligned with the excited part, while the second mask counts the beam losses produced by another, equivalent in charge, part of the beam. The benefit of this technique is that the external factors that will modify the beam losses, like the change of the insertion device gaps, will be recorded by the two masks, but the losses created due to depolarisation will be seen only by one mask. As is shown in Fig. 4.6a, the beam loss data recorded from the excited and non-excited mask during user time show the same trend until the excited mask starts to depolarise and the losses become high. Dividing the counts from the two masks, the initial ratio (before depolarisation) will be equal to one. When depolarisation occurs, this ratio will change, and the frequency of the excitation signal at which the depolarisation occurs will indicate the spin precession frequency. The ratio against the excited frequency, which is translated in energy values, is shown in Fig. 4.6b. Fig. 4.6c shows the vertical emittance data during the energy measurement scan. The data show that the vertical beam size is not disturbed during the beam excitation. The big spike in the start of the scan is due to external factors, the same that produced the high beam losses in the two masks. An error function fit, according to Eq.2.33, is used to determine the energy, the width of the resonance and the beam loss increase with the corresponding uncertainties. The error of each measurement is in the order of keV. The idea of the beam loss rate normalisation using the losses from two bunches circulating in the storage ring [113] was first introduced at the VEPP-4 storage ring facility at Budker Institute Nuclear Physics (Novosibirsk, Russia). However, we established the same idea using all the bunches of the fill pattern independently. Only later, when preparing the publication for the present work [114], we came upon the study of VEPP-4.



(a) The beam loss data recorded from the excited and non-excited mask during user time.



(b) The ratio between the beam losses from the excited and the non-excited mask. The red line corresponds to the error function fit.



(c) The vertical emittance during the beam excitation

Figure 4.6: The ratio of the beam loss data from the two masks show the beam depolarisation. The vertical emittance shows that the vertical beam size does not change during the beam excitation.

4.2.4 Accuracy of the energy measurement

Resonant Spin Depolarisation is a high accuracy energy measurement technique. However, systematic errors set the resolution limit of the method. Some of them are:

- The fundamental limit is set from the measurement of the electron mass [48].
- The revolution frequency and the frequency of the magnet used to excite the beam introduce additional uncertainties.
- The depolarising resonance width, which increases when the beam is excited strongly, with small, long-lasting frequency steps as explained in paragraphs 4.2.6, 4.2.7, limit the accuracy of the measurement. Thus, it should be sufficiently small to reach a good precision in the measurement, while the resonance is strong enough to be observed. The biased energy value can be corrected with an opposite direction frequency scan [115], [116]. Thus, both sides of the resonance can be scanned, and the center of the resonance can be detected from both directions. If there is a discrepancy, a correction can be applied to minimise the energy measurement bias, as explained in paragraph 4.2.5.
- The spin tune spread can be the origin of systematic tune shifts. This effect is expected to be very small.
- In a real storage ring, the optics imperfections that do not allow the beam to reach the maximum theoretical polarisation level, can affect the accuracy of the energy measurement [117], [118]. The radial error fields that the beam experiences mainly at the quadrupoles and sextupoles can cause a perturbation of the spin tune $\delta\nu$, which is added to the nominal spin tune ν_0 . The final spin tune $\nu = \nu_0 + \delta\nu$ is not dependent on the same energy as the nominal spin tune ν_0 , and a bias is introduced in the measurement.

4.2.5 Reverse scan

In this test, the depolarisation scan was repeated backwards. One of the purposes of this scan was to distinguish the depolarisation resonance from a betatron resonance. In the first scan, the beam was excited, with frequencies ranging from a low value to a high value. The same scan, with the reverse sequence of frequencies, was repeated as is shown in Fig. 4.7 in the red line. The results showed that the beam losses increase and are not

restored when the scan is stopped. This scan validated that the crossed resonance is the depolarisation resonance.

The reverse scan approach can be employed to correct the bias introduced in the energy measurement due to the non-zero spin resonance width. The set of the two scans can give information about both sides of the resonance. The peak of the resonance, which correspond to the beam's energy, can be measured by the two scans. If the two values do not agree, the difference between them can be calculated, and the mid-value can give a more accurate energy measurement. The two scans in Fig. 4.7 were fitted to calculate the energy and the width of the resonance. The energy was found to be the same for both of the scans, while the width was 11 keV for the normal scan (in the blue line) and 15 keV for the reverse scan (in the red line). This approach can be considered to be applied to correct the width systematic error when the resonance is strong. When the resonance strength is weak, as in this case, the width systematic error is small.

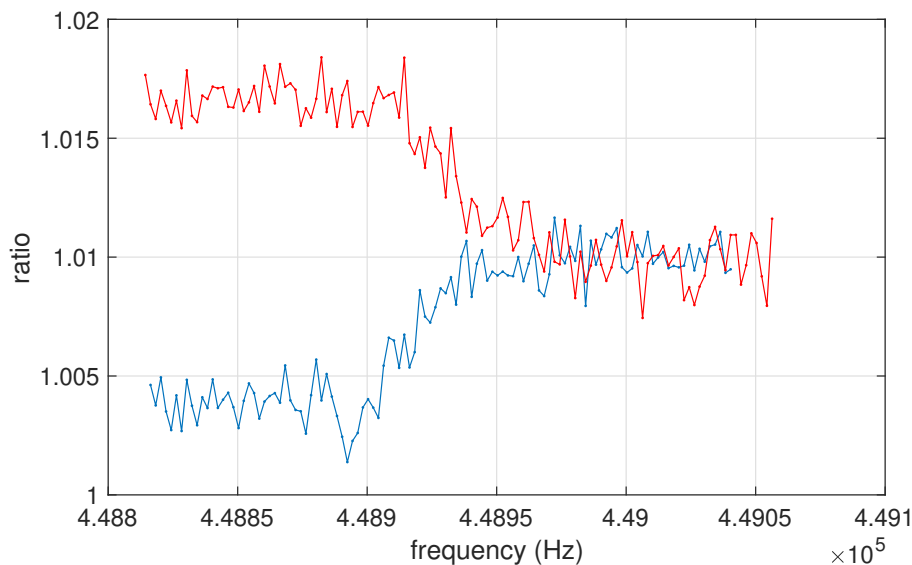


Figure 4.7: The normal scan and the reverse scan are shown in the blue line and red line respectively.

4.2.6 Strength of resonance

Different parameters of the depolarisation scan were studied to understand and improve the depolarisation method. The impact of the magnetic field strength produced by the stripline kickers during the depolarisation scan was investigated. The scan was repeated with two different gains in the amplifier of the striplines. The increase in amplifier's gain

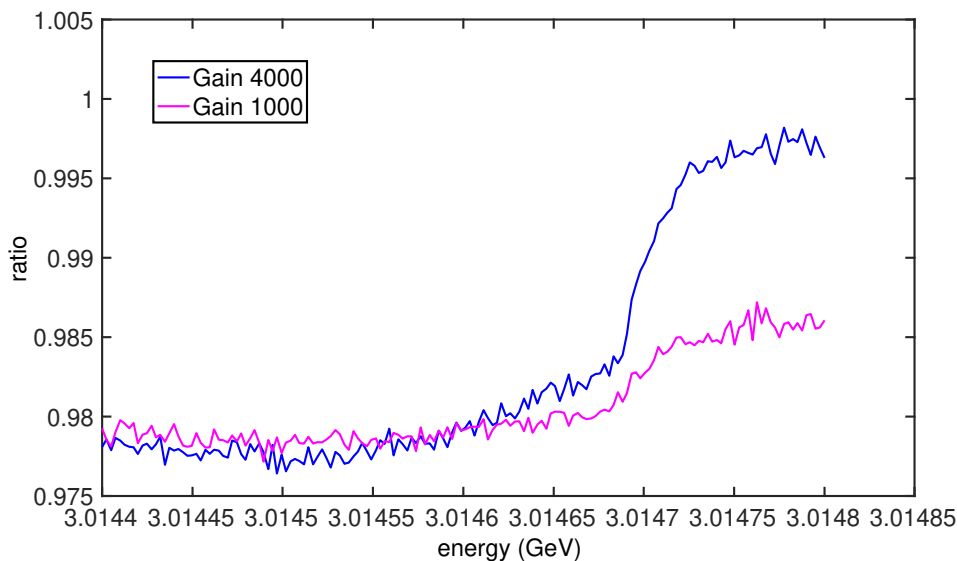


Figure 4.8: Two depolarisation scan with different gain in the amplifier of the striplines.

leads to a higher increase of the beam losses during the depolarisation scan, as is shown in Fig 4.8. The width of the resonance follows the same trend. This was expected according to the simulations using the FESTA code.

4.2.7 Excitation duration of the depolarisation scan

The duration of the excitation in the depolarisation scan was investigated. According to Froissart-Stora, the depolarisation will be stronger for longer excitation. Fig. 4.9 shows different depolarisation scans for different excitation time values. Indeed, stronger depolarisation can be achieved in the expense of long duration scans.

4.2.8 Synchrotron sidebands

The synchrotron oscillations modulate the spin tune resulting in synchrotron sidebands around the main resonance frequency. The frequency distance between the synchrotron sidebands and the main resonance equals the synchrotron frequency. To distinguish the main resonance from its sidebands, the RF voltage changes and consequently, the synchrotron frequency changes as the relationship between these two parameters is dictated by the formula:

$$\omega_s^2 = \frac{2\pi h\alpha}{E_0 T_0^2} \sqrt{(eV)^2 - U_0^2} \quad (4.6)$$

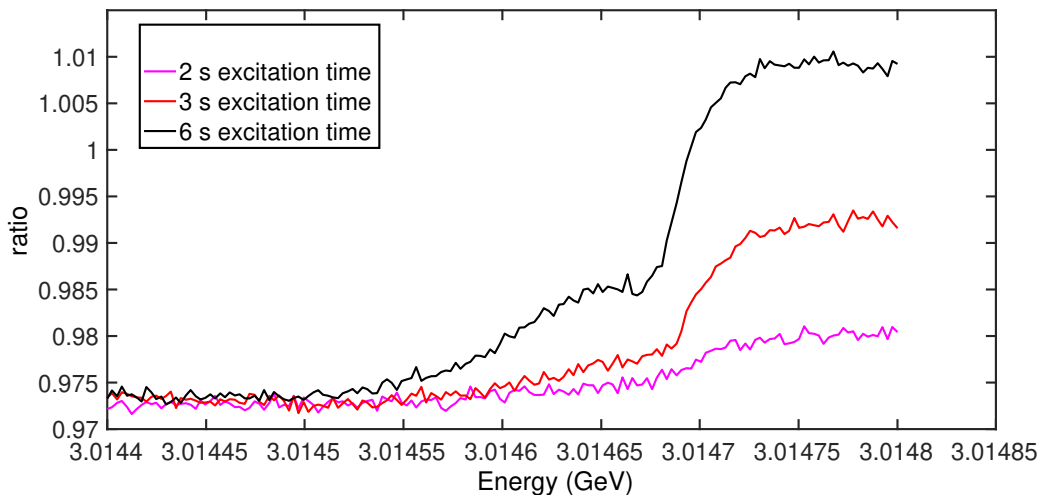


Figure 4.9: Depolarisation scan for different excitation times.

where α is the momentum compaction factor of the ring, h the harmonic number, E_0 the beam energy, T_0 the revolution time, U_0 the energy loss of the electron in one turn and V the RF acceleration voltage. The RF voltage was set to 2.9 MV, 2.5 MV and 2.1 MV and the left synchrotron sideband resonance and the main resonance were excited. As is shown in Fig. 4.10 the left resonance was shifted 180 Hz towards the right in each step, which is the expected shift for 0.4 MV decrease in the RF voltage. This measurement identifies the main resonance, which remains the same for all the scans and the synchrotron sideband, which shifts towards the main resonance when the synchrotron frequency decreases.

The beam loss increase due to depolarisation for the case of 2.9 MV is lower compared to the other two cases. This could be caused by the incomplete equilibrium polarisation, since the measurements with 2.9 MV RF voltage started first. When both parts of the beam get polarised simultaneously, the loss rate ratio between them is one. However, when the unexcited mask is polarised completely, we can see the re-polarisation of the excited mask after the depolarisation event in Fig. 4.10 for the case of 2.1 MV and 2.5 MV RF voltage.

4.2.9 Continuous energy measurements

One of the key aims of this project was to make the energy measurements compatible with the user operation, while the vertical emittance of the beam is small. Studies at BESSY [36] have shown previously that energy measurements were achieved during user operation using a beam with vertical emittance in the range of a few nm-rad. The Diamond Light Source operates with a small vertical emittance in the range of 8 pm-rad and the main

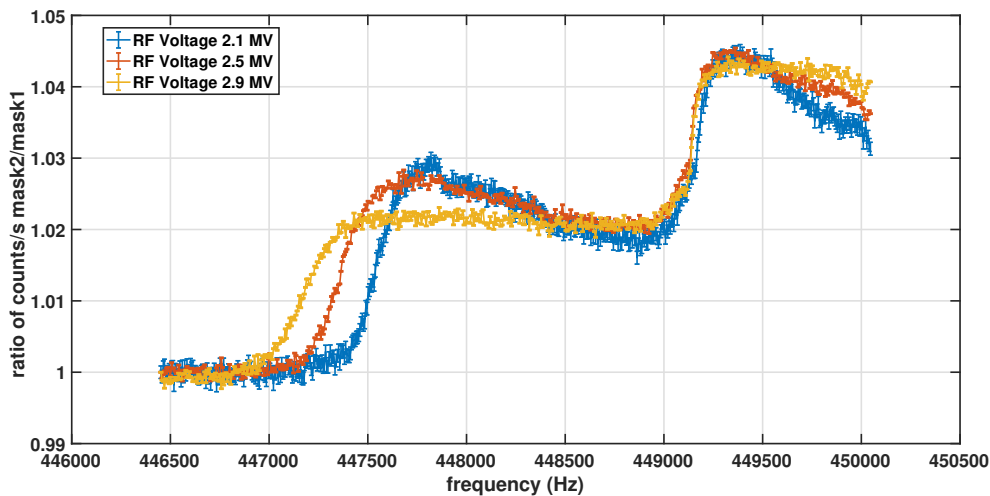


Figure 4.10: Three depolarisation scans to identify the main resonance and the sidebands.

challenge is not to affect this quantity when the beam is excited during the depolarisation scans. During user time, a low current is applied in the striplines, which is enough to depolarise the beam but not affect the beam's quality. Then, the new approach of the depolarisation scan is used. Fig. 4.11 illustrates the continuous energy measurements that took place for three weeks of user operation of DLS. The energy is changing in the range of 10 keV. These results are very important to study the stability of the energy and investigate the sources of the beam energy fluctuations. The beam can be subject to changes in circumference due to temperature change. After a long shutdown or during different seasons, the temperature will change the circumference of the machine and is expected to result in a different beam energy.

The beam energy E in an electron storage ring is related to the integrated dipole field strength $B_n I_n$ by the equation [69]: $E(\text{GeV}) = \frac{0.29979}{2\pi} \sum_n B_n(T) I_n(m)$, where n indicates the n^{th} element. Energy drifts can emanate from factors that change the integrated dipole field strength such as the horizontal COD in the quadrupoles, non-zero average horizontal COD in the correctors, noise in the magnets power supplies [37], [119].

In the end, the impact of the insertion devices in the energy stability could be investigated.

4.2.10 Betatron resonances

The high sensitivity of the beam loss detectors enables them to detect losses created by excited higher order betatron resonances. An increase in the vertical emittance during the

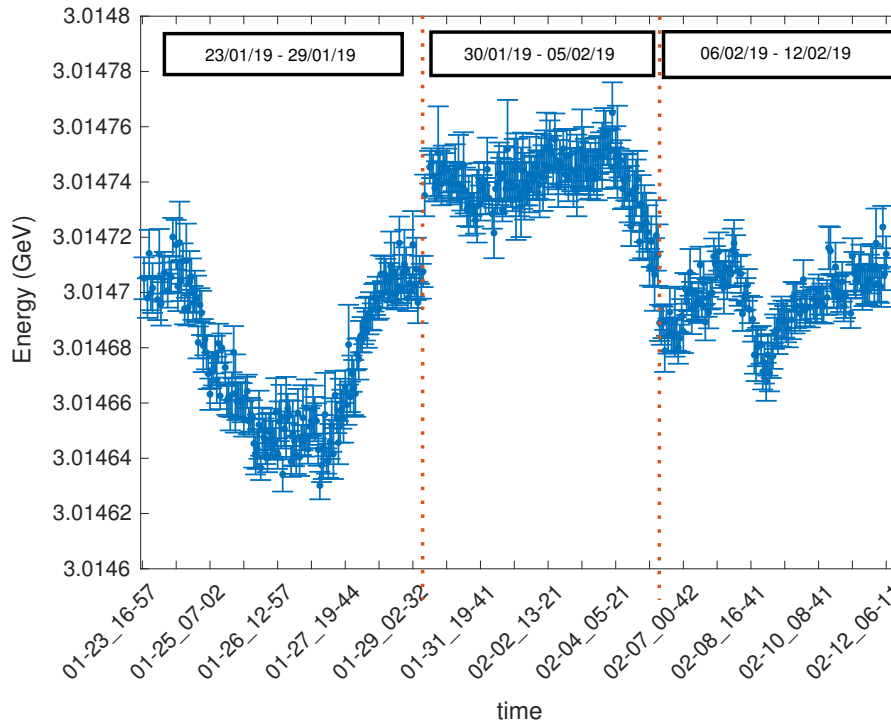
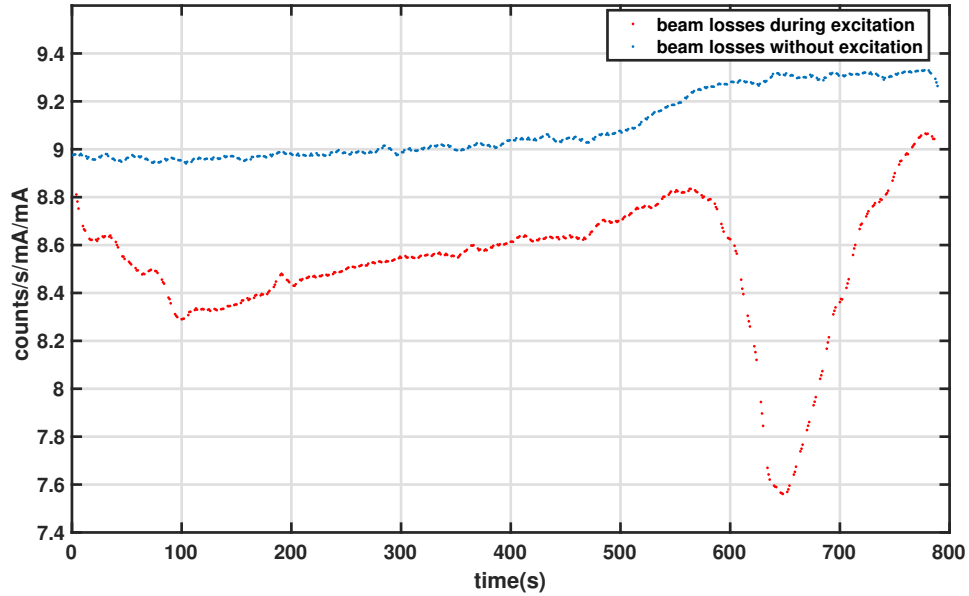


Figure 4.11: Energy measurements every hour for a duration of three weeks of user operation. The energy changes over the time in the order of ten keV.

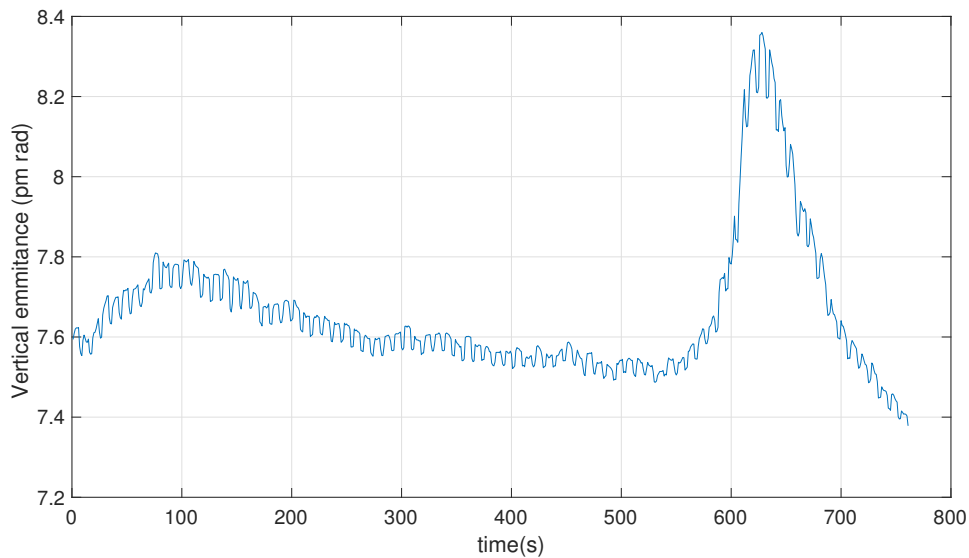
crossing of the betatron resonances is observed, accompanied by decreased beam losses. After the crossing, the above parameters are back to their normal values. These resonances interfere with the beam loss data due to depolarisation resonance and add background noise to the measurement. In Fig. 4.12a the red data represent the losses recorded during the time the beam is excited. The results in Fig. 4.12b show two betatron resonances and an underlying depolarisation resonance. The depolarisation resonance is identified by the increased count rate at the end of the scan and the simultaneous decrease of the vertical beam size. This data is difficult to fit and calculate the energy of the beam. For this purpose, after the excitation of each frequency, the scan is suspended for one second, and the blue data is recorded. Since the beam losses due to betatron resonances fade out in the period of 1 s the blue data show only the losses due to depolarisation that remain. These data, which show clearly the beam depolarisation, can be fitted and provide an energy measurement.

4.2.11 Top-up normalisation

For the online energy measurements, the excitation strength was chosen to be as low as not to disturb the vertical emittance. This implies that for a decent amount of depolarisation,



(a) The red line represents the loss rates during the excitation. The blue line corresponds to the loss rates that happen when the excitation is paused and any betatron resonances have damped out. The data is plotted against time to show the sequence of excitation and non-excitation during the measurement



(b) The vertical emittance data show the decrease of the beam size during the excitation of a betatron resonance. After the crossing of the resonance the beam size is back to its normal value.

Figure 4.12: The betatron resonance excitation shown in beam losses and the vertical beam size.

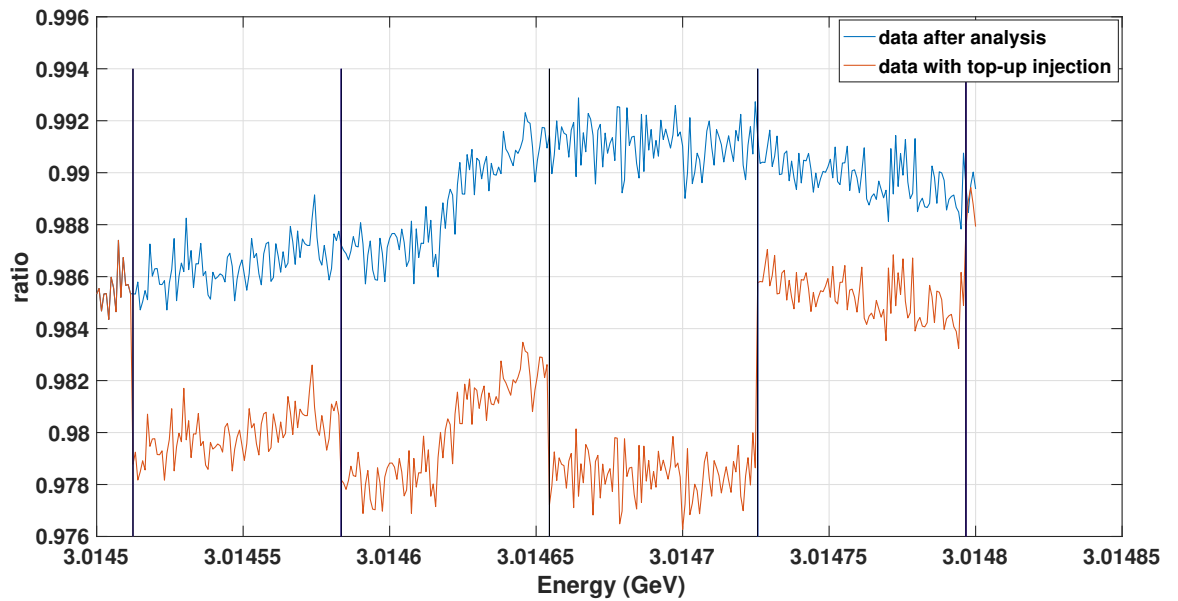


Figure 4.13: The ratio of the beam losses acquired by the two masks in the red line changes after each top-up injection which are illustrated by a vertical black line. The blue data show the data after the analysis for normalising the steps due to the top-up injection.

the beam should be excited for a long time, according to the Froissart-Stora formula. Typically, scans last more than ten minutes, which is the time interval between the top-up events at DLS [120]. The top-up system selectively fills the bunches with the lowest charge and creates inequalities between the losses of the two masks, as the losses depend on the total charge in each mask. For this reason, the ratio between the counts of the two masks is recorded before and after the injection without beam excitation. The difference between the two count rates is calculated and subtracted from the new data set after the injection. The data before and after the analysis are illustrated with the red and the blue line, respectively, in Fig. 4.13. Thus, the depolarisation scans can last for long periods, keeping the ratio of the two masks unrelated to the top-up injections.

4.2.12 Momentum compaction factor

The high accuracy of the resonant spin depolarisation to measure the beam energy was exploited to measure the momentum compaction factor. The momentum compaction factor is defined as the relative change in the electron's path length with respect to a

relative change in the beam energy.

$$\alpha = \frac{\Delta l/l}{\Delta p/p} \quad (4.7)$$

According to the principle of phase stability, the RF frequency defines the reference path length for one revolution of the storage ring.

$$l = \frac{hc}{f_{RF}} \quad (4.8)$$

where h is the harmonic number. As such, a relative change in RF frequency is equal and opposite to the relative change in path length

$$\frac{\Delta l}{l} = -\frac{\Delta f_{RF}}{f_{RF}} \quad (4.9)$$

and the compaction factor can be expressed as [121]:

$$\alpha = -\frac{\Delta f_{RF}/f_{RF}}{\Delta p/p} \quad (4.10)$$

By measuring beam energy as a function of RF frequency, a linear polynomial fit can extract the momentum compaction factor. The beam current was set to 50 mA in order for the optics to be close to the model. The low loss rate due to low beam current was not a problem for detecting the beam depolarisation due to the high sensitivity of the beam loss system. The RF frequency was varied in the range of ± 100 Hz. The results are shown in Fig. 4.14, and the calculated value for the momentum compaction factor is $\alpha = (1.61 \pm 0.03) \times 10^{-4}$. This agrees with the value calculated using the machine model of $\alpha = 1.56 \times 10^{-4}$.

4.3 Summary

The beam polarisation was measured using the lifetime data for two cases, with wiggler insertion devices on and off. According to the experimental studies and the calculations, the two insertion devices decrease the beam polarisation level from 89% to 62%.

The principle of resonant spin depolarisation was described with experimental data. The new approach to depolarise one part of the beam while the other is used to witness beam

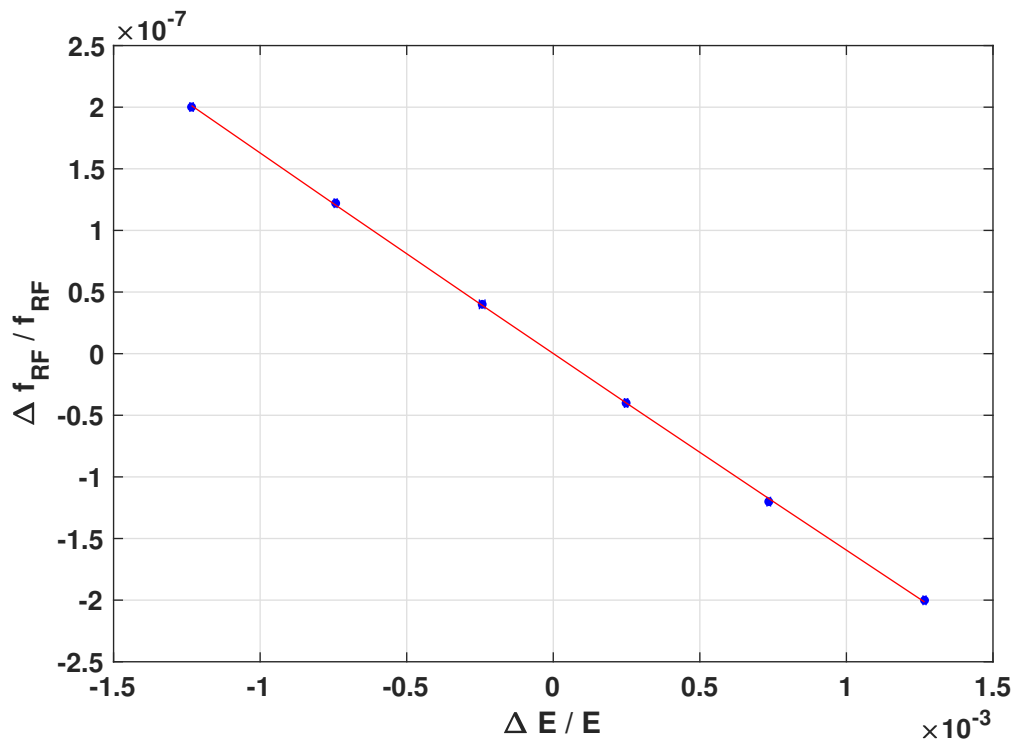


Figure 4.14: The relative change of the energy is plotted versus the relative change of the RF frequency. A linear fit derives the momentum compaction factor.

losses created from different factors was introduced. High precision of $\frac{\Delta E}{E} = 10^{-6}$ was achieved, while the vertical beam size was not affected during user time. Phenomena that limit the accuracy of the resonant spin depolarisation measurements were discussed. A good orbit correction system and high-quality alignment of the magnets is mandatory for a high level build-up polarisation and accurate energy measurements.

The reverse scan and the sidebands study were used to distinguish the main resonance from the synchrotron sidebands or any betatron resonances. The reverse scan was suggested as a good approach to correct the systematic error related to the resonance width when the depolarisation resonance is strong.

The scan with different excitation time and gain in the amplifier of the striplines was repeated. The impact of these parameters on the depolarisation resonance revealed the optimal approach for the excitation method in the measurements. It was suggested that the excitation of the depolarisation resonance should be sufficiently weak to reach a good accuracy in the measurement and strong enough for the resonance to be observed.

The continuous energy measurements for three weeks were presented. The energy varied in the range of 10 keV. The beam stability can be studied using this measurement as a tool

to relate the changes of the energy to changes on other machine's parameters. In the end, due to the high precision of the resonant spin depolarisation technique, the momentum compaction factor was measured successfully.

Conclusions

5.1 Summary of work

The technique of Resonant Spin Depolarisation was studied for the case of Diamond electron storage ring. The method was successfully conducted and the energy was measured with high precision.

The energy measurement was difficult to be conducted prior to the present work. The RSD method requires a polarised beam which means a long period was needed for this measurement. The approach to measuring the energy during user time had been challenging as the beam could not be excited strongly, to avoid disturbing its small vertical emittance. A weak excitation, however, would not reveal the depolarisation resonance in the beam loss monitors that were used for this measurement.

One part of this study was focused on the polarisation level that can be achieved in the storage ring of DLS. The polarisation level was calculated theoretically using the SLIM code. The most important finding using the results from the SLIM calculation revealed that a high level of polarisation cannot be achieved when the sum of the betatron and the spin tune is equal with an integer. Thus, the betatron tunes should be chosen carefully in order to allow the beam to polarise and later conduct the energy measurement with RSD. The polarisation level was calculated experimentally for the circumstances of the wigglers being turned on and off. It was found that wigglers reduce the polarisation level but the level of the polarisation is enough in order to conduct a depolarisation measurement.

This project aimed to improve the detectors employed for this method as well as to develop

a technique that will allow the measurement to be conducted during user time to overcome the existent challenges.

It was shown that the high count rate of the beam loss monitors was paramount for the success of this measurement. According to Poisson statistics which the counting method follows, the error of a measurement decreases with the number of the counts. The detectors were designed and positioned to capture the largest part of the beam losses. The sensitivity of the scintillator which was used as the detector in the beam loss monitors allowed the system to maximise the pulses created by the losses. The algorithm that was used for the pulse counting was improved and the system of the beam loss monitors could give a high accuracy in the measurements and reveal small changes in the created beam losses that could not be detected before.

Changes in the beam loss rate were detected with the new system even with weak excitation of the depolarisation resonance. This made the measurement compatible with user operation as the vertical emittance is not disturbed. Thus, there is no need for dedicated time to allow the beam to polarise and the measurements can be conducted continuously in the storage ring providing a reading of the energy in a frequency that has not been implemented before in DLS. However, the challenge that was met due to high sensitivity was the detection of background data.

Background data was generated either by losses due to external factors, like the changing of the gap in the insertion devices or by the excitation of higher-order betatron resonances during the scans of the energy measurement. Two different strategies were used to overcome these problems.

The losses due to external factors were anticipated by the gating of the excitation and the detection scheme. One part of the beam is excited and the beam losses from this part were normalised with the beam losses from another non-excited part of the beam with equal charge. In this way, the ratio of the beam losses of the two parts of the beam shows only the effect of the excitation.

The beam losses due to the excitation of the betatron resonances were separated by the beam losses due to depolarisation. This was accomplished by collecting data after the excitation of each frequency and not in parallel with the excitation. This allows the beam to recover from the excitation of the betatron resonance. The data of the beam losses will witness the depolarisation when it happens without including the background data.

When the depolarisation resonance is not detected due to the weak excitation, the excitation time and the frequency step of the scan were increased. This approach follows the Froissart-Stora equation for the depolarisation process and results in long-lasting energy measurements scans. FESTA simulations were used for understanding the depolarisation resonance process since the Froissart-Stora equation describes only the relationship between the polarisation level after and before the excitation. The expected shape of the depolarisation resonance was simulated successfully from FESTA and the results guided the later experiments. However, there was not an agreement between the depolarisation level and the width of the resonance between the simulation and the experiment.

After anticipating all these challenges, the energy measurements were successfully conducted during user time. An energy measurement reading is given every hour and the beam energy stability can be studied. The online measurements were demonstrated for a period of three weeks in this thesis.

5.2 Future Work

This work has been successful and the energy measurement technique of RSD is working in the storage ring of DLS. However, there is some further work that could be conducted as complementary to this study.

Regarding the detectors, the location of the beam loss monitors to detect Touschek particles could be studied further. Finding locations along the ring where the detected beam losses come only from Touschek scattering would be of interest. This count rate could be compared with the count rate of this study where the detectors were placed after the collimators and beam losses were created from other causes as well. Coincidence counting could be explored as well, since the algorithm is already implemented in the acquisition software.

The energy measurements that are collected every hour can be used for further studies. Any changes in the energy, could be correlated with other changes of beam or machine parameters. The stability in the long term could be explored as well.

One more useful addition to this work could be the implementation of a software that can run the energy measurements script in parallel with all the other measurements and diagnostics, without the need of a user to start and stop the scan.

List of Abbreviations

RF Radio Frequency

PMT Photomultiplier Tube

SLIM Solution by Linear Matrices

FESTA Fast Electron Spin Tracking based on Accelerator Toolbox

RSD Resonant Spin Depolarisation

DLS Diamond Light Source

ADC Analog-to-Digital Converter

GUI Graphical User Interface

FPGA Field Programmable Gate Arrays

LINAC Linear Accelerator

COD Closed Orbit Distortion

XOP X-ray Optics

DCCT DC Current Transformer

TMBF Transverse Multibunch Feedback

DAC Digital-to-Analog Converter

NCO Numerical Control Oscillator

EVG Event Generator

EVR Event Receiver

TTL Transistor-transistor logic

Bibliography

- [1] V. Kain, Beam Dynamics and Beam Losses - Circular Machines (arXiv:1608.02449) (2016) pp. 18, contribution to the 2014 Joint International Accelerator School: Beam Loss and Accelerator Protection, Newport Beach, CA, USA , 5-14 Nov 2014. doi:10.5170/CERN-2016-002.21.
- [2] A. Wolski, Beam Dynamics in High Energy Particle Accelerators, Imperial College Press, London, 2014. doi:10.1142/p899.
- [3] A. Wolski, Linear Dynamics : Review of Hamiltonian Mechanics, URL: <https://www.cockcroft.ac.uk/wp-content/uploads/2014/12/wolski-1.pdf> (November 2012).
- [4] A. Wolski, Linear Dynamics : The Accelerator Hamiltonian in a straight coordinate system, URL: <http://pcwww.liv.ac.uk/~awolski/Teaching/Cockcroft/LinearDynamics/LinearDynamics-Lecture2.pdf> (November 2012).
- [5] Barletta,Spentzouris,Harms, Fundamentals of accelerator physics and technology with simulations and measurements lab, URL: <https://uspas.fnal.gov/materials/12MSU/emitlect.pdf> (June 2012).
- [6] R. D. Ruth, Single-particle dynamics in circular accelerators, AIP Conf. Proc. 153 (1987) pp. 150–235. doi:10.1063/1.36365.
- [7] W. T. Weng, S. R. Mane, Fundamentals of particle beam dynamics and phase space, AIP Conf. Proc. 249 (1992) pp. 3–45. doi:10.2172/5149692.

-
- [8] M. Martini, An introduction to transverse beam dynamics in accelerators, Tech. Rep. CERN-PS-96-011-PA, CERN, Geneva (March 1996).
URL <http://cds.cern.ch/record/311384>
- [9] A. Wolski, Low-emittance storage rings, in: CERN Accelerator School: Advanced Accelerator Physics Course, 2014, pp. 245–294. doi:10.5170/CERN-2014-009.245.
- [10] M. Minty, F. Zimmermann, Measurement and control of charged particle beams, Particle acceleration and detection, Springer, Berlin, 2003. doi:10.1007/978-3-662-08581-3.
- [11] H. Wiedemann, Particle accelerator physics I: Basic principles and linear beam dynamics, Springer, Berlin, Germany, 1999. doi:10.1007/978-3-662-03827-7.
- [12] E. J. N. Wilson, An introduction to particle accelerators, Oxford Univ. Press, Oxford, 2001. doi:10.1093/acprof:oso/9780198508298.001.0001.
URL <http://cds.cern.ch/record/513326>
- [13] S. Khan, Collective Phenomena in Synchrotron Radiation Sources: Prediction, Diagnostics, Countermeasures, Springer, Berlin, Heidelberg, 2006. doi:10.1007/978-3-540-34313-4.
- [14] H. Wiedemann, Storage Ring Design as a Synchrotron Light Source, Springer Berlin Heidelberg, Berlin, Heidelberg, 2003, pp. 125–136. doi:10.1007/978-3-662-05312-6_8.
- [15] T. Lee, J. Choi, H. Kang, Simple determination of Touschek and beam-gas scattering lifetimes from a measured beam lifetime, Nuclear Instruments and Methods in Physics Research A 554 (2005) 85–91. doi:10.1016/j.nima.2005.08.049.
- [16] X. Huang, J. Corbett, /SLAC, Measurement of beam lifetime and applications for spear3, Nuclear Instruments and Methods in Physics Research A 629 (1). doi:10.1016/j.nima.2010.10.147.
URL <https://www.osti.gov/biblio/1010948>
- [17] P. Kumar, G. Singh, A. D. Ghodke, P. Singh, Dependence of loss rate of electrons due to elastic gas scattering on the shape of the vacuum chamber in an electron storage ringarXiv:1409.3060.

-
- [18] C. Sun, J. Zhang, J. Li, W. Z. Wu, S. F. Mikhailov, V. G. Popov, H. L. Xu, A. W. Chao, Y. K. Wu, Polarization measurement of stored electron beam using Touschek lifetime, *Nuclear Instruments and Methods in Physics Research A* 614 (2010) 339–344. doi:10.1016/j.nima.2010.01.034.
- [19] E. Jaeschke, S. Khan, J. R. Schneider, J. B. Hastings (Eds.), *Synchrotron Light Sources and Free-Electron Lasers*, Springer, 2015. doi:10.1007/978-3-319-04507-8.
- [20] Lightsources.org official page, [<https://lightsources.org>].
- [21] Diamond machine description (official page), [<https://www.diamond.ac.uk/Science/Machine/Components>].
- [22] R. Bartolini, C. Abraham, M. Apollonio, B. et. al, Double-double bend achromat cell upgrade at the diamond light source: From design to commissioning, *Phys. Rev. Accel. Beams* 21 (2018) 050701. doi:10.1103/PhysRevAccelBeams.21.050701.
- [23] CLRC. Diamond Synchrotron Light Source: Report of The Design Specification. Technical report, 2002.
- [24] Epics and open-source, [<https://www.aps.anl.gov/epics>].
- [25] A.-S. Muller, Measurements of beam energy, CERN Accelerator School: Beam Diagnostics, France, May (2009) pp. 427doi:10.5170/CERN-2009-005.
- [26] S. Kurokawa, S. Lee, E. Perevedentsev, S. Turner (Eds.), Beam measurement. Proceedings, Joint US-CERN-Japan-Russia School on Particle Accelerators, Montreux and Geneva, Switzerland, May 11-20, 1998, World Scientific, 1999. doi:10.1142/4107.
- [27] J. Safranek, Experimental determination of storage ring optics using orbit response measurements, *Nuclear Instruments and Methods in Physics Research A* 388 (1997) 27–36. doi:10.1016/S0168-9002(97)00309-4.
- [28] R. Assmann, et al., Calibration of centre-of-mass energies at LEP 2 for a precise measurement of the W boson mass, *Eur. Phys. J. C* 39 (2005) 253–292. arXiv:hep-ex/0410026, doi:10.1140/epjc/s2004-02108-8.
- [29] R. Klein, R. Thornagel, G. Brandt, G. Ulm, P. Kuske, R. Gorgen, Measurement of the BESSY II electron beam energy by Compton-backscattering of

- laser photons, *Nuclear Instruments and Methods in Physics Research A* 486 (2002) 545–551. doi:10.1016/S0168-9002(01)02162-3.
- [30] E. Tegeler, G. Ulm, Determination of the beam energy of an electron storage ring by using calibrated energy dispersive Si(Li)-detectors, *Nuclear Instruments and Methods in Physics Research A* 266 (1-3) (1988) 185–190. doi:10.1016/0168-9002(88)90380-4.
- [31] E. Tarazona, P. Elleaume, Measurement of the absolute energy and energy spread of the esrf electron beam using undulator radiation, *Review of Scientific Instruments* 67 (9) (1996) 3368–3368. doi:10.1063/1.1147371.
URL <https://doi.org/10.1063/1.1147371>
- [32] K.-J. Kim, An Interference Wiggler for Precise Diagnostics of Electron Beam Energy, *Conf. Proc. C* 870316 (1987) pp. 562.
- [33] Suwada, Tsuyoshi, Precise beam energy monitor using synchrotron radiation interferometry, in: *SLAC-AP-120*, 1999.
- [34] C. Steier, J. M. Byrd, P. Kuske, Energy Calibration of the Electron Beam of the ALS using Resonant Depolarization, in: *Proceedings of 7th European Particle Accelerator Conference (EPAC 2000)*, Vienna, Austria, 2000, pp. 1566–1568.
- [35] L. Arnaudon, L. Knudsen, J. P. Koutchouk, R. Olsen, M. Placidi, R. Schmidt, M. Crozon, A. Blondel, R. Assmann, B. Dehning, Measurement of LEP beam energy by resonant spin depolarization, *Phys. Lett. B* 284 (1992) 431–439. doi:10.1016/0370-2693(92)90457-F.
- [36] P. Kuske, in: *European Workshop on Beam Diagnostics and Instrumentation for Particle Accelerators, (DIPAC 2001)*, DIPAC, Grenoble, France, 2001.
- [37] J. Zhang, L. Cassinari, M. Labat, A. Nadji, L. S. Nadolski, D. Pedeau, Precise beam energy measurement using resonant spin depolarization in the SOLEIL storage ring, *Nuclear Instruments and Methods in Physics Research A* 697 (2013) 1–6. doi:10.1016/j.nima.2012.09.003.
- [38] K. P. Wootton, M. J. Boland, W. J. Corbett, X. Huang, L. et. al, Storage ring lattice calibration using resonant spin depolarization, *Physical Review Special Topics - Accelerators and Beams* 16 (7) (2013) pp. 1–13. doi:10.1103/PhysRevSTAB.16.074001.

-
- [39] V. Blinov, V. Ivakin, V. Kaminskiy, V. Kudryavtsev, S. Nikitin, I. Nikolaev, L. Shekhtman, Beam Energy Measurement by Resonant Depolarization Method at VEPP-4M, in: CERN-BINP Workshop for Young Scientists in e^+e^- Colliders: CERN, Geneva, Switzerland, August 22–25, 2016, 2017, pp. 109–118. doi:10.23727/CERN-Proceedings-2017-001.109.
- [40] D. Barber, et al., The HERA polarimeter and the first observation of electron spin polarization at HERA, Nuclear Instruments and Methods in Physics Research A 329 (1993) 79–111. doi:10.1016/0168-9002(93)90924-7.
- [41] S. Belomesthnykh, A. Bondar, M. Yegorychev, V. Zhilitch, G. Korniyukhin, S. Nikitin, E. Saldin, A. Skrinsky, G. Tumaikin, An observation of the spin dependence of synchrotron radiation intensity, Nuclear Instruments and Methods in Physics Research Section A 227 (1) (1984) 173–181. doi:https://doi.org/10.1016/0168-9002(84)90119-0.
- [42] I. Martin, M. Apollonio, R. Fielder, G. Rehm, R. Bartolini, Energy measurements with resonant spin depolarisation at diamond, in: Proceedings of 2nd International Conference, (IPAC 2011), San Sebastian, Spain, 2011, pp. 1404–1406.
- [43] J. D. Jackson, Reviews of Modern Physics 48 (3) (1976) pp. 417–433. doi:10.1103/RevModPhys.48.417.
- [44] A. Sokolov, I. Ternov, On The Spin And Polarization Effects In The Theory Of Synchrotron Radiation, in: 4th International Conference on High-Energy Accelerators, 1963, pp. 1271–1275.
- [45] D. P. Barber, G. Ripken, Radiative polarization, computer algorithms and spin matching in electron storage ringsarXiv:physics/9907034.
- [46] A. W. Chao, Polarization of a stored electron beam, AIP Conf. Proc. 87 (1982) pp. 395–449. doi:10.1063/1.33619.
- [47] S. Lee, Spin dynamics and snakes in synchrotrons, World Scientific, 1997.
- [48] L. Arnaudon, et al., Accurate determination of the LEP beam energy by resonant depolarization, Z. Phys. C 66 (1995) 45–62. doi:10.1007/BF01496579.
- [49] D. Barber, G. Ripken, Radiative polarization, computer algorithms and spin matching in electron storage ringsarXiv:physics/9907034.

-
- [50] J.-Q. Lan, H.-L. Xu, Numerical simulation study on spin resonant depolarization due to spin—orbit coupling, *Chinese Physics B* 21 (8). doi:10.1088/1674-1056/21/8/084501.
- [51] R. Neumann, R. Rossmanith, A fast depolarizer for large electron positron storage rings, *Nuclear Instruments and Methods in Physics Research* 204 (1982) pp. 29–36. doi:10.1016/0167-5087(82)90073-4.
- [52] S. Mane, Synchrotron sideband spin resonances in high-energy electron storage rings, *Nuclear Instruments and Methods in Physics Research A* 292 (1990) 52–74. doi:10.1016/0168-9002(90)91734-S.
- [53] S. Mane, Polarization of electron beams in high energy storage rings Part II. Series expansion with tune modulation, *Nuclear Instruments and Methods in Physics Research A* 321 (1-2) (1992) 42–47. doi:10.1016/0168-9002(92)90375-E.
- [54] C. Biscari, J. Buon, B. W. Montague, Depolarizing Effects of Quantum Fluctuations and the Action of Nonlinear Wigglers on Equilibrium Polarization Level, *Nuovo Cim. B* 81 (1984) 128–142. doi:10.1007/BF02721605.
- [55] K. Yokoya, Effects of radiative diffusion on the spin flip in electron storage rings, *Part. Accel.* 14 (1983) pp.39.
- [56] S. Mane, Synchrotron oscillation effects for spin resonances driven by a localized oscillating rf magnetic field, *Nuclear Instruments and Methods in Physics Research A* 726 (2013) pp. 104–112. doi:10.1016/j.nima.2013.05.176.
- [57] N. Carmignani, F. Ewald, L. Farvacque, B. Nash, P. Raimondi, Modeling and Measurements of Spin Depolarization, 6th International Particle Accelerator Conference, JACoW, Geneva, Switzerland, 2015, pp. 109–112. doi:https://doi.org/10.18429/JACoW-IPAC2015-MOPWA013.
- [58] S. R. Mane, Method for calculating strong synchrotron tune modulation of depolarizing resonances in storage rings, in: *Conference Record of the 1991 IEEE Particle Accelerator Conference, 1991*, pp. 1690–1691 vol.3. doi:10.1109/PAC.1991.164746.
- [59] G. Z. M. Berglund, Spin-Orbit Maps and Electron Spin Dynamics for the Luminosity Upgrade Project at HERA, Ph.D. thesis, Royal Inst. Tech., Stockholm (2001). doi:10.3204/DESY-THESIS-2001-044.

-
- [60] B. W. Montague, Polarized Beams in High-energy e^+e^- Storage Rings, Phys. Rept. 113 (1984) 1–96. doi:10.1016/0370-1573(84)90031-0.
- [61] Y. Derbenev, A. Kondratenko, A. Skrinsky, Radiative Polarization at Ultrahigh-Energies, Part. Accel. 9 (1979) 247–266.
- [62] S. R. Mane, Polarization at tlep/fcc-ee: ideas and estimates (2014). arXiv:1406.0561.
- [63] J. Buon, Depolarization Enhancement due to Energy Spread, Tech. Rep. DESY-HERA-83-14 (1983).
URL <https://bib-pubdb1.desy.de/record/222555>
- [64] L. Arnaudon, et al., Accurate determination of the LEP beam energy by resonant depolarization, Z. Phys. C 66 (1995) 45–62. doi:10.1007/BF01496579.
- [65] M. A. Leonova, Achieving High Spin-Flip Efficiency with an RF Magnet and Discovery of Spin-Resonance Strength Formulae Problem, Ph.D. thesis, Michigan U. (2008).
- [66] C. Bernardini, G. F. Corazza, G. Di Giugno, G. Ghigo, R. Querzoli, J. Haissinski, P. Marin, B. Touschek, Lifetime and beam size in a storage ring, Phys. Rev. Lett. 10 (1963) 407–409. doi:10.1103/PhysRevLett.10.407.
- [67] Wolfram mathematica., [<https://www.wolfram.com/mathematica/>].
- [68] A. Chao, Evaluation of Beam Distribution Parameters in an Electron Storage Ring, J. Appl. Phys. 50 (1979) 595. doi:10.1063/1.326070.
- [69] A. W. Chao, M. Tigner, Handbook of Accelerator Physics and Engineering, WORLD SCIENTIFIC, 1999. arXiv:<https://www.worldscientific.com/doi/pdf/10.1142/3818>, doi:10.1142/3818.
URL <https://www.worldscientific.com/doi/abs/10.1142/3818>
- [70] Y. Z. Sarah Cousineau, Jeff Holmes, Transverse beam optics, part i (January 2011).
- [71] R. Talman, Representation of thick quadrupoles by thin lenses, Tech. Rep. SSC-N-33, Lawrence Berkeley Nat. Lab., Berkeley, CA (1985).
URL <http://cds.cern.ch/record/533900>
- [72] H. Burkhardt, R. De Maria, M. Giovannozzi, T. Risselada, Improved Teapot Method and Tracking with Thick Quadrupoles for the LHC and its Up-

- grade (CERN-ACC-2013-0059) (2013) 3 p.
URL <https://cds.cern.ch/record/1572997>
- [73] K. L. Brown, A first- and second-order matrix theory for the design of beam transport systems and charged particle spectrometers, SLAC, Stanford, CA, 1972.
URL <https://cds.cern.ch/record/283218>
- [74] J. Kolski, D. Barlow, Ray Tracing through the Edge Focusing of Rectangular Benders and an Improved Model for the Los Alamos Proton Storage Ring.
URL <http://www.osti.gov/bridge/servlets/purl/1011078-qyGTk1/>
- [75] L. Schachinger, R. Talman, Teapot: A Thin Element Accelerator Program for Optics and Tracking, Part. Accel. 22 (1987) 35.
- [76] MAD - Methodical Accelerator Design, <http://mad.web.cern.ch>.
- [77] Elegant, https://ops.aps.anl.gov/manuals/elegant_latest/elegant.html.
- [78] N. Carmignani, F. Ewald, L. Farvacque, B. Nash, P. Raimondi, Modeling and Measurements of Spin Depolarization, in: 6th International Particle Accelerator Conference, 2015, p. MOPWA013. doi:10.18429/JACoW-IPAC2015-MOPWA013.
- [79] N. Carmignani, Touschek Lifetime Studies and Optimization of the European Synchrotron Radiation Facility, Ph.D. thesis, Pisa U. (2014). doi:10.1007/978-3-319-25798-3.
- [80] P. Kuske, T. Mayer, Set up for beam energy measurements at BESSY II, Conf. Proc. C 960610 (1996) 1570–1572.
- [81] S. Y. Lee, Spin resonance strength of a localized rf magnetic field, Phys. Rev. ST Accel. Beams 9 (2006) 074001. doi:10.1103/PhysRevSTAB.9.074001.
URL <https://link.aps.org/doi/10.1103/PhysRevSTAB.9.074001>
- [82] Y. M. Shatunov, S. R. Mane, Calculations of spin response functions in rings with Siberian Snakes and spin rotators, Physical Review Accelerators and Beams 12 (2) (2009) 024001. doi:10.1103/PhysRevSTAB.12.024001.
- [83] V. I. Ptitsyn, Y. M. Shatunov, S. R. Mane, Spin response formalism in circular accelerators, Nuclear Instruments and Methods in Physics Research A 608 (2) (2009) 225–233. doi:10.1016/j.nima.2009.06.066.

-
- [84] A. Kondratenko, M. Kondratenko, Y. Filatov, Calculation of spin resonance strength at COSY accelerator, *Pisma Fiz. Elem. Chast. Atom. Yadra* 2008 (6) (2008) 902–918. doi:10.1134/S1547477108060083.
- [85] M. Brugger, H. Burkhardt, B. Goddard, *Interactions of Beams With Surroundings*, 2013. doi:10.1007/978-3-642-23053-0_5.
- [86] R. Wigmans, *Calorimetry in High Energy Physics*, NATO Sci. Ser. B 275 (1991) 325–379. doi:10.1007/978-1-4684-6006-3_6.
- [87] Saint-gobain, product comparisons, inorganic and organic scintillators structural differences, [<https://www.crystals.saint-gobain.com/>].
- [88] P. Lecoq, *Scintillation Detectors for Charged Particles and Photons*, Springer, Cham, 2020, pp. 45–89. doi:10.1007/978-3-030-35318-6_3.
- [89] The spectrum of riemannium physmatics in a nutshell, [<https://thespectrumofriemannium.wordpress.com/tag/cherenkov-radiation/>].
- [90] C. Grupen, *Physics of particle detection*, AIP Conf. Proc. 536 (1) (2000) 3–34. arXiv:physics/9906063, doi:10.1063/1.1361756.
- [91] G. F. Knoll, *Radiation Detection and Measurement*, 3rd ed., 3rd Edition, John Wiley and Sons, New York, 2000.
- [92] SENSE, Photomultiplier Tubes, <https://www.sense-pro.org/111-sensors/pmt>.
- [93] Photomultiplier tubes, basics and applications, [https://www.hamamatsu.com/resources/pdf/etd/PMT_handbook_v3aE.pdf].
- [94] Photonis, photomultiplier tube basics, [https://psec.uchicago.edu/library/photomultipliers/Photonis_PMT_basics.pdf].
- [95] K. Wittenburg, *Beam Loss Monitors*, in: CAS - CERN Accelerator School: Beam Instrumentation, 2020. arXiv:2005.06522.
- [96] Gafchromic RTQA2 Film, <http://www.gafchromic.com>.
- [97] N. Hubert, N. Béchu, P. Brunelle, L. Cassinari, C. Herbeaux, S. Hustache, J. F. Lamarre, P. Lebasque, F. Marteau, A. Nadji, L. S. Nadolski, *Radiation damages and characterization in the soleil storage ring, IBIC 2013: Proceedings of the 2nd International Beam Instrumentation Conference (2013)* 644–647.
- [98] Eljen technology., [<http://www.eljentechnology.com>].

-
- [99] ET enterprises, <http://et-enterprises.com/>.
- [100] Photon Counting SNR Simulator, https://hub.hamamatsu.com/us/en/interactive_tools/photon-counting-snr-simulator/index.html.
- [101] S. L. Hulbert, J. M. Weber, Flux and brightness calculations for various synchrotron radiation sources, Nuclear Instruments and Methods in Physics Research Section A: Accelerators, Spectrometers, Detectors and Associated Equipment 319 (1) (1992) 25–31. doi:[https://doi.org/10.1016/0168-9002\(92\)90526-A](https://doi.org/10.1016/0168-9002(92)90526-A).
- [102] (X-ray Oriented Programs), <http://www.esrf.eu/Instrumentation/software/data-analysis/xop2.4>.
- [103] Autodesk AutoCAD, <http://web.autocad.com/>.
- [104] Instrumentation Technologies, Beam Loss Monitor readout electronics, [<http://www.i-tech.si>].
- [105] <https://www.xilinx.com>.
- [106] M. Abbott, G. Rehm, I. Uzun, Architecture of Transverse Multi-Bunch Feedback Processor at Diamond, in: 15th International Conference on Accelerator and Large Experimental Physics Control Systems, 2015, p. MOPGF097. doi:10.18429/JACoW-ICALEPCS2015-MOPGF097.
- [107] M. Abbott, G. Rehm, I. Uzun, A New Transverse and Longitudinal Bunch by Bunch Feedback Processor, in: 16th International Conference on Accelerator and Large Experimental Physics Control Systems, 2018, p. THPHA115. doi:10.18429/JACoW-ICALEPCS2017-THPHA115.
- [108] Texas Instruments, <https://www.ti.com>.
- [109] Werlatone, <https://www.werlatone.com>.
- [110] Review of the diamond light source timing system, RuPAC 2010 Contributions to the Proceedings - 22nd Russian Particle Accelerator Conference (2010) 144–146.
- [111] J. Buon, J.-P. Koutchouk, Polarization of electron and proton beams (CERN-SL-94-80-AP) (1994) pp. 56. doi:10.5170/CERN-1995-006.879.
URL <https://cds.cern.ch/record/269521>

-
- [112] A. Blondel, J. M. Jowett, Dedicated wigglers for polarization, Tech. Rep. CERN-LEP-Note-606. LEP-Note-606, CERN, Geneva (1988).
URL <https://cds.cern.ch/record/442913>
- [113] V. Blinov, V. Kiselev, S. Nikitin, I. Nikolaev, V. Smaluk, Measurement of the Energy Dependence of Touschek Electron Counting Rate, Conf. Proc. C 110328 (2011) 426–428.
- [114] N. Vitoratou, P. Karataev, G. Rehm, Continuous energy measurement of the electron beam in the storage ring of diamond light source with resonant spin depolarization, Phys. Rev. Accel. Beams 22 (2019) 122801. doi:10.1103/PhysRevAccelBeams.22.122801.
- [115] V. M. Aulchenko, et al., New precision measurement of the J / ψ and ψ -prime meson masses, Phys. Lett. B 573 (2003) 63–79. doi:10.1016/j.physletb.2003.08.028.
- [116] Nuclear Instruments and Methods in Physics Research Section A: Accelerators, Spectrometers, Detectors and Associated Equipment 494 (1) (2002) 68–74. doi:[https://doi.org/10.1016/S0168-9002\(02\)01447-X](https://doi.org/10.1016/S0168-9002(02)01447-X).
- [117] R. Assmann, J. P. Koutchouk, Spin tune shifts due to optics imperfections.
- [118] A. V. Bogomyagkov, S. A. Nikitin, A. G. Shamov, Influence of the vertical closed orbit distortions on accuracy of the energy calibration done by resonant depolarization technique [arXiv:1801.01227](https://arxiv.org/abs/1801.01227).
- [119] A. V. Bogomyagkov, S. E. Karnaev, V. A. Kiselev, B. V. Levichev, E. B. Levichev, A. I. Naumenkov, S. A. Nikitin, I. B. Nikolaev, I. Y. Protopopov, D. N. Shatilov, E. A. Simonov, G. M. Tumaikin, Study of the Energy Stability in the VEPP-4M Storage Ring.
URL <https://cds.cern.ch/record/583365>
- [120] C. Christou, V. C. Kempson, Operation of the diamond light source injector, in: Proceedings of 2007 IEEE Particle Accelerator Conference (PAC 2007), 2007.
- [121] A. Ben Kalefa, I. Birkel, E. Huttel, A. S. Muller, M. Pont, F. Perez, Momentum Compaction Factor and Nonlinear Dispersion at the ANKA Storage Ring, in: Proceedings of 9th European Particle Accelerator Conference (EPAC 2004), Lucerne, Switzerland, 2004, pp. pp. 2005–2007.